

Single-Photon Avalanche Diode Image Sensors for Harsh Radiation Environments

Présentée le 17 avril 2024

Faculté des sciences et techniques de l'ingénieur
Laboratoire d'architecture quantique
Programme doctoral en microsystemes et microélectronique

pour l'obtention du grade de Docteur ès Sciences

par

Ming-Lo WU

Acceptée sur proposition du jury

Prof. C. Moser, président du jury
Prof. E. Charbon, directeur de thèse
Prof. L. Ratti, rapporteur
Prof. S. Charlebois, rapporteur
Dr J.-M. Sallese, rapporteur

Stay humble.
Stay hungry.

To my parents...

Acknowledgements

This thesis would not have been possible without the assistance of many people. During my studies, I experienced one of the best research environments I have ever been in. The working atmosphere at AQUALab is highly collaborative, and when we encounter problems, we can always rely on the group's support. First and foremost, I would like to express my gratitude to my supervisor, Professor Edoardo Charbon, for his guidance throughout my studies. Whenever a research idea emerged, we could consistently count on his support, whether in terms of resources or ideas. Thanks to him, we also had valuable opportunities to participate in conferences and workshops, collaborating with other research groups.

I want to convey my appreciation to the entire AQUALab team, especially those who provided invaluable assistance during my time in the lab. A special thanks goes to Kazuhiro Morimoto and Francesco Gramuglia for their chip design, which formed the foundation of my work. The projects wouldn't have been possible without your innovative design, reminding me of Isaac Newton's quote, 'If I have seen further, it is by standing on the shoulders of Giants'. I also want to extend my thanks to Emanuele Ripiccini and Jad Benserhir, who worked tirelessly alongside me for weeks in the challenging radiation test facilities. Additionally, I'd like to express my appreciation to my office mates, Ekin Kizilkan and Utku Karaca, who not only provided valuable support throughout my studies but also contributed to a very enjoyable working environment.

As a student with a background in device physics during my bachelor's and master's studies, I've always been curious about the final stage of the semiconductor industry chain, which involves electronics design. This curiosity drove me to join this lab, where I aim to expand my knowledge of electronics. Starting a completely new discipline in the doctoral program is undoubtedly challenging, and I've had to rely on the support of many individuals to comprehend this new subject. First and foremost, I would like to express my gratitude to Paul Mos, who provided thorough guidance in firmware design. I would also like to express my appreciation to Augusto Carimatto, Baris Can Efe, Kerim Yildirim, and Pouyan Keshavarzian. They not only provided valuable expertise in hardware, software, and circuit designs but also shared wonderful moments outside of office hours. Furthermore, I am thankful to Claudio Bruschini, Ivan Michel Antolovic, Andrei Ardelean, Yang Lin, and David Rodriguez Martinez for their stimulating discussions, which have resulted in diverse perspectives and breakthroughs in

various projects.

I would like to acknowledge some former and new members of the lab, with whom I may not have had extensive working relationships, but with whom I shared enjoyable moments. This includes Andrea Ruffino, Andrada Muntean, Preethi Padmanabhan, Tommaso Milanese, Vladimir Pesic, Yasemin Uzun, and Bedirhan Ilik, whose advice helped me steer my studies in a positive direction. I also want to express my gratitude to Brigitte Khan and Begonia Tora for their administrative support, which greatly facilitated my smooth transition into a new academic environment in a foreign nation.

I have had the opportunity to collaborate with several researchers outside of the lab, and I would like to express my gratitude to my coauthors, especially Vytautas Zickus from Prof. Daniele Faccio's group. Additionally, I want to thank Lorenzo Paolozzi for his valuable support at the CERN beamline.

I wholeheartedly dedicate this work to my parents, who always support and give me great advice throughout my academic journey. I am deeply grateful for their role in helping me reach the place I am today.

Neuchâtel, 2023

M.-L. Wu

Abstract

The space industry has experienced substantial growth in recent years, leading to rapid advancements in space exploration and space-based technologies. Consequently, the study of electronics and sensor performance in extreme environments has become crucial. Light sensors play a pivotal role among the detectors utilized in space-based missions. Nonetheless, the space environment poses several challenges for these systems. Among the emerging photodetectors, the single-photon avalanche diode (SPAD) has showcased exceptional timing performance, sensitivity to low light, and scalability due to its increasing compatibility with complementary metal–oxide–semiconductor technology. To investigate the feasibility of implementing SPADs in harsh environments and improving current systems, we first focused on studying the radiation hardness of SPADs. We subjected various SPAD systems to testing using protons and neutrons, which are sources of both ionizing and non-ionizing damage. The impact of radiation on all the figures of merit of SPADs under various operating conditions involving temperature and bias was characterized. Notably, the SPADs were exposed to the highest displacement damage dose (> 1 PeV/g) ever delivered. Furthermore, we explored methods to mitigate damage post-radiation exposure by incorporating annealing steps.

Multiple applications using the developed megapixel SPAD camera and individual SPAD pixels were successfully demonstrated. The findings illustrate that a well-engineered SPAD camera is capable of high dynamic range 2D imaging, making it well-suited for space-based imaging scenarios with varying light contrast scenes. Our investigation also encompassed an exploration of how the design of SPAD-based systems and potential radiation-induced damage can influence imaging performance. We presented 3D multi-object ranging utilizing the SPAD camera. Furthermore, the camera resolution facilitated the reconstruction of 4D light-in-flight imaging by harnessing the concept of apparent superluminal motion. Additionally, the thesis explores wide-field fluorescence lifetime imaging microscopy (FLIM) and spectral FLIM systems. These systems are integrated with machine learning algorithms for data processing, resulting in a significant reduction in processing time by over four orders of magnitude compared to conventional methods. Furthermore, we found that the sensitivity of SPADs to ionizing radiation and high avalanche gain makes them suitable for particle or radiation detection. A particle coincidence timing precision down to 15.3 ps was achieved, which is the best recorded to date. These applications possess potential for planetary exploration, astronomy, and material studies.

Acknowledgements

Key words: dynamic range, fluorescence lifetime imaging microscopy (FLIM), harsh environment, imaging, light-in-flight, object ranging, minimum ionizing particle (MIP), particle detection, radiation, single-photon avalanche diode (SPAD), space application, time gating

Résumé

L'industrie spatiale a connu une croissance substantielle ces dernières années, conduisant à des avancées rapides dans l'exploration spatiale et les technologies spatiales. En conséquence, l'étude de l'électronique et des performances des capteurs dans des environnements extrêmes est devenue cruciale. Les capteurs de lumière jouent un rôle essentiel parmi les détecteurs utilisés dans les missions spatiales. Néanmoins, l'environnement spatial pose plusieurs défis pour ces systèmes. Parmi les photodétecteurs émergents, la diode à avalanche monophotonique (SPAD) a montré des performances de synchronisation exceptionnelles, une sensibilité à la faible lumière et une extensibilité grâce à sa compatibilité croissante avec la technologie à base de métal-oxyde-semiconducteur complémentaire. Pour étudier la faisabilité de la mise en œuvre des SPAD dans des environnements hostiles et améliorer les systèmes actuels, nous nous sommes d'abord concentrés sur l'étude de la résistance aux radiations des SPAD. Nous avons soumis différents systèmes SPAD à des essais avec des protons et des neutrons, qui sont des sources de dommages ionisants et non ionisants. L'impact des radiations sur toutes les caractéristiques des SPAD dans diverses conditions de fonctionnement impliquant la température et la polarisation a été caractérisé. À noter, les SPAD ont été exposés à la plus haute dose de dommages par déplacement ($> 1 \text{ PeV/g}$) jamais enregistrée. De plus, nous avons exploré des méthodes pour atténuer les dommages après l'exposition aux radiations en incorporant des étapes d'recuit.

Plusieurs applications utilisant l'appareil photo SPAD mégapixels développé et les pixels SPAD individuels ont été démontrées avec succès. Les résultats montrent qu'un appareil photo SPAD bien conçu est capable de réaliser des images 2D avec une grande plage dynamique, ce qui le rend adapté aux scénarios d'imagerie spatiale présentant des contrastes lumineux variables. Notre étude a également exploré comment la conception de systèmes basés sur les SPAD et les dommages potentiels dus aux radiations peuvent influencer les performances en imagerie. Nous avons présenté une technique de détection 3D d'objets multiples utilisant l'appareil photo SPAD. De plus, la résolution de l'appareil photo a permis la reconstruction d'images 4D de la lumière en vol en exploitant le concept de mouvement superluminal apparent. De plus, la thèse explore des systèmes de microscopie à durée de vie de fluorescence en champ large (FLIM) et de FLIM spectral. Ces systèmes sont intégrés avec des algorithmes d'apprentissage automatique pour le traitement des données, ce qui entraîne une réduction significative du temps de traitement de plus de quatre ordres de grandeur par rapport aux méthodes

conventionnelles. De plus, nous avons constaté que la sensibilité des SPAD aux radiations ionisantes et leur gain d'avalanche élevé les rendent adaptés à la détection de particules ou de radiations. Une précision de synchronisation de particules de coïncidence jusqu'à 15,3 ps a été obtenue, ce qui constitue le meilleur enregistrement à ce jour. Ces applications présentent un potentiel pour l'exploration planétaire, l'astronomie et les études sur les matériaux.

Mots clefs : plage dynamique, microscopie à fluorescence à durée de vie (FLIM), environnement hostile, imagerie, lumière en vol, estimation d'objet, particule d'ionisation minimale (MIP), détection de particules, radiation, diode avalanche à photon unique (SPAD), application spatiale, déclenchement temporel.

Contents

Acknowledgements	i
Abstract	iii
List of figures	ix
List of tables	xiii
List of acronyms	xv
1 Introduction	1
1.1 SPAD operating principles	2
1.2 Overview of SPADs	6
1.2.1 Dark count	6
1.2.2 Photon detection probability	6
1.2.3 Timing jitter	7
1.2.4 SPAD-based systems	7
1.3 Harsh environments and effects	9
1.3.1 Radiation environment and sources	10
1.3.2 Effects of radiation on electronic devices	10
1.3.3 Mitigation techniques for radiation effects	13
1.4 Applications of SPAD-based systems for harsh environments	14
1.5 Objectives of the thesis	16
1.6 Thesis structure	16
2 Methods and tools	17
2.1 Sensor architecture	17
2.1.1 Intensity mode readout	18
2.1.2 Gating mode readout	19
2.2 Sensor characterization	22
2.2.1 Noise performance	22
2.2.2 Gate profile	24

3 Radiation hardness study of SPADs	29
3.1 Proton radiation	29
3.1.1 Materials and methods	29
3.1.2 Results	31
3.2 Neutron radiation	46
3.2.1 Materials and methods	46
3.2.2 Results	47
3.3 Discussions	48
3.4 Conclusion	54
4 Results of SPAD-based applications	57
4.1 2D high dynamic range imaging	57
4.2 3D imaging	65
4.2.1 Object ranging	65
4.2.2 Fluorescence lifetime imaging	66
4.3 4D imaging	73
4.3.1 Hyperspectral fluorescence lifetime imaging	73
4.3.2 Light-in-flight imaging	77
4.4 Particle/radiation detection	83
4.5 Conclusion	90
5 Conclusion	93
5.1 Summary	93
5.2 Scientific contribution	94
5.3 Technology comparison	95
5.4 Future perspective	98
A SPAD characterization methods	99
A.1 Dark count	99
A.2 Afterpulsing	101
A.3 Photon detection probability	102
A.4 Timing jitter	103
B Gallery	105
Bibliography	122
List of Publications	123
Curriculum Vitae	125

List of Figures

1.1	p-n junction	2
1.2	SPAD structure and its electric field profile	3
1.3	Impact ionization	4
1.4	SPAD operation and circuit configuration	5
1.5	Photon absorption in indirect and direct bandgap material	5
1.6	SPAD-based systems	8
1.7	SPAD pixel circuits	8
1.8	Extreme lighting condition in space applications	9
1.9	Ionizing interactions by electrons and photons	11
1.10	Single-event effect and displacement damage	12
1.11	Proton NIEL in silicon	13
2.1	The megapixel SPAD camera and its pixel schematic	18
2.2	Timing diagram of intensity mode operation	18
2.3	FPGA design for streaming binary images	19
2.4	1-bit, 2-bit, and 3-bit images	20
2.5	Multi-bit images	21
2.6	Timing diagram of gating mode	22
2.7	DCR characterization of the megapixel SPAD array	23
2.8	Cumulative probability of DCR	24
2.9	Example of a gating mode application	25
2.10	Gate profile of the megapixel SPAD camera	26
2.11	Deconvolution of measured photon profile	27
3.1	Proton beamline and DUTs	31
3.2	Breakdown voltage before and after irradiation	32
3.3	SPAD's DCR behaviors under irradiation	34
3.4	Cumulative DCR distribution of the 180 nm megapixel SPAD camera irradiated with 100 MeV and 10 MeV protons	35
3.5	TRIM simulations for 100 MeV and 10 MeV protons entering silicon	36
3.6	Mean and median DCR evolution of the 180 nm megapixel SPAD camera irradiated with 100 MeV and 10 MeV protons	36

3.7	Mean DCR of the 180 nm megapixel SPAD camera at different temperatures before and after irradiation	37
3.8	Distribution of activation energy in the megapixel SPAD camera before and after proton irradiation	38
3.9	Afterpulsing of 55 nm SPAD before and after irradiation	39
3.10	Afterpulsing probability of irradiated SPADs and its temperature dependency	40
3.11	DCR prediction model	42
3.12	DCR random telegraph signal	42
3.13	PDP of the megapixel camera before and after irradiation	43
3.14	Jitter performance before and after irradiation	44
3.15	Room-temperature annealing of the 180 nm megapixel SPAD camera	45
3.16	High-temperature annealing of the 180 nm megapixel SPAD camera	46
3.17	Activation energy distribution of the megapixel SPAD camera after irradiation and after high-temperature annealing	46
3.18	SPAD DCR levels after irradiated with neutron	48
3.19	Afterpulsing measurement of a 25 μm SPAD irradiated with neutron	49
3.20	Temperature-dependent DCR of the sample irradiated with $10^{11} \text{ n}_{eq}/\text{cm}^2$	50
3.21	Working principle of deep level transient spectroscopy	51
3.22	Normalized DCR of different SPADs irradiated with protons	55
4.1	Measured photon count and SNR of a 12-bit image	59
4.2	Noise of a 12-bit image	60
4.3	Influence of DCR and frame rate on the SNR	61
4.4	Influence of DCR and frame rate on the dynamic range	61
4.5	Exposure timing of mono- and dual-exposure mode	62
4.6	Measured count and SNR of mono- and dual-exposure mode	63
4.7	High dynamic range image of real-life scene	64
4.8	Multi-object ranging setup	65
4.9	Principle of time-gated acquisition of FLIM	67
4.10	Artificial neural network for lifetime retrieval	69
4.11	0.5 megapixel wide-field FLIM	70
4.12	3.64 megapixel wide-field FLIM	72
4.13	Hyperspectral fluorescence lifetime imaging setup	73
4.14	Spectral resolution calibration	74
4.15	Principle of hyperspectral fluorescence lifetime imaging	75
4.16	Hyperspectral fluorescence lifetime imaging results	77
4.17	Light-in-flight experimental setup	78
4.18	The principle of observing light-in-flight in the Minkowski spacetime	79
4.19	Light-in-flight experimental result	80
4.20	Light-in-flight model	81
4.21	Dataset of the light-in-flight measurement	82
4.22	Reconstruction result of light-in-flight with 4D information	82

LIST OF FIGURES

4.23 Particle detection experimental setup	84
4.24 Schematic of the particle detection setup	85
4.25 Timing response of SPAD	85
4.26 MIP and photon timing resolution at different voltages	86
4.27 DCR before and after MIP detection	87
4.28 Simulation result of coincidence DCR	88
4.29 DCR of different size SPADs at different temperature	89
A.1 SPAD's equivalent circuit and output	100
A.2 Temperature dependence of the breakdown voltage	101
A.3 Relationship between apparent afterpulsing probability and illumination	102
A.4 PDP measurement setup	103
A.5 Timing jitter measurement setup	104
B.1 Megapixel SPAD array	105
B.2 High timing precision SPAD pixel	106
B.3 High timing precision SPAD pixel	106

List of Tables

3.1	Irradiation dose steps with target DDD and corresponding TID for 100 MeV and 10 MeV protons	30
3.2	Final DCR and APP of SPADs irradiated with different neutron doses	49
4.1	Comparison of LSQ and ANN results for different datasets	71
4.2	Comparison of the MIP detection performance with state-of-the-art systems	89
5.1	Comparison of single photodetectors	95
5.2	Comparison of photodetector arrays/image sensors	97

List of acronyms

ANN	artificial neural network
APD	avalanche photodiode
APP	afterpulsing probability
BCD	bipolar-CMOS-DMOS
CCD	charge-coupled device
CMOS	complementary metal-oxide-semiconductor
cps	counts per second
DCR	dark count rate
DDD	displacement damage dose
DMOS	double diffusion metal oxide semiconductor
DUT	device under test
FLIM	fluorescence lifetime imaging microscopy
FOV	field of view
FPGA	field-programmable gate array
FWHM	full-width-at-half-maximum
FWTM	full-width-at-tenth-maximum
IRF	instrument response function
LET	linear energy transfer
LHCb	Large Hadron Collider beauty
LiDAR	light detection and ranging
MIP	minimum ionizing particle
NIEL	non-ionizing energy loss
PDP / PDE	photo detection probability / photo detection efficiency
QIS	quanta image sensor
QKD	quantum key distribution
RICH	ring-imaging Cherenkov
RTS	random telegraph signal
SEE	single-event effect
SNR	signal-to-noise ratio
SPAD	single-photon avalanche diode
TCSPC	time-correlated single-photon counting
TID	total ionizing dose

1 Introduction

The field of space-based technologies and high-energy physics has experienced remarkable growth in recent years. As we continue to push the boundaries of such applications, studying the performance of electronics and sensors in extreme environments becomes crucial. The harsh conditions of space, characterized by high radiation levels, extreme temperature spans, and other challenges, require technologies capable of operating effectively in such inhospitable conditions.

Optical sensors play an important role in space-based missions, offering significant benefits in imaging, ranging systems, and communication systems that require precise timing. Photon-counting photodetectors are particularly valuable for a wide range of applications, including material analysis, biological studies, and quantum communication. These detectors encompass photomultiplier tubes, superconducting nanowire detectors, and photodiodes, with photodiodes being the most commonly used due to their simplicity and scalability. However, their performance in low-light conditions, which are prevalent in many fields of interest, is often hindered by a critical signal-to-noise ratio mainly attributed to readout electronics noise.

In recent years, single-photon avalanche diodes (SPADs) have emerged as promising alternatives with excellent timing performance, sensitivity to low light, and scalability, thanks to their compatibility with complementary metal–oxide–semiconductor (CMOS) technology. The development of large-scale SPAD arrays with resolutions exceeding megapixels has opened up new possibilities for SPADs in various applications. Researching the performance and viability of SPAD-based systems in these applications will contribute to the development of robust and reliable SPAD-based technologies for space exploration and high-energy physics studies.

This chapter provides the fundamental operating principle of SPADs, an overview of SPAD-based systems, and the key figures of merit used to evaluate the performance of SPADs. Moreover, we will examine various applications in harsh environments and discuss the impact of radiation. We will outline the aim and objectives of this work and provide an overview of the structure and organization of the thesis.

1.1 SPAD operating principles

The basic structure of SPADs consists of a p-n junction, shown in Fig.1.1. When p-type and n-type material touch, the electrons from the n-type region and the holes from the p-type region diffuse towards the other side and recombine with the local majority carriers. This leads to the formation of a depletion region near the p-n interface. Specifically, the n-side near the interface becomes positively charged due to the presence of fixed positive ions, while the p-side near the interface becomes negatively charged due to the presence of fixed negative ions. This charge separation creates an electric field across the depletion region. This electric field formed in the depletion region acts as a potential barrier for carriers, preventing further diffusion to the other side.

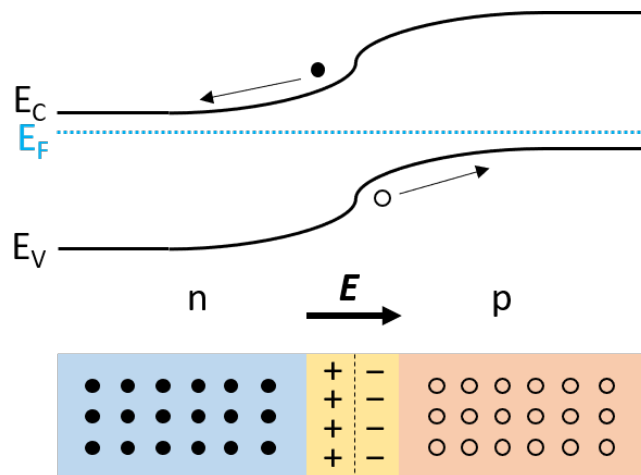
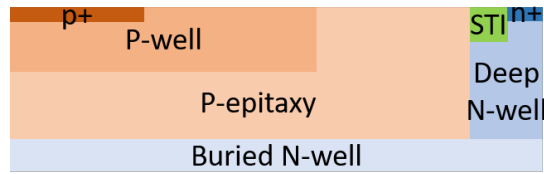


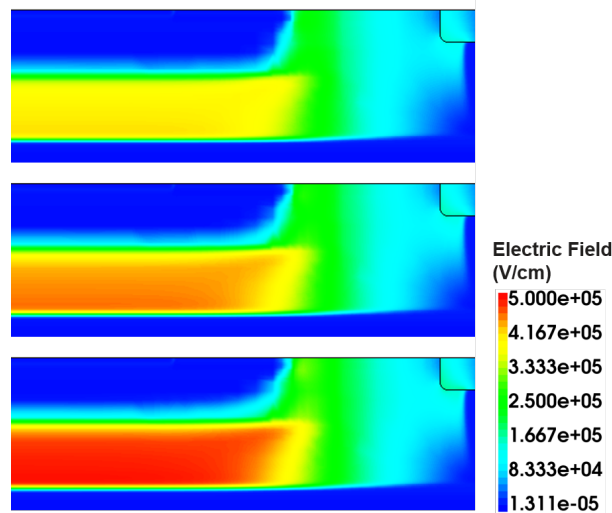
Figure 1.1: A p-n junction and its band diagram. The free electrons are represented by solid balls. The holes are represented by hollow balls. The electric field, E , is formed in the depletion region. E_C , E_V , and E_F represent the energy levels of the conduction band, valence band, and Fermi level, respectively.

We can see an example of a SPAD cross section in Fig.1.2a. In this structure, the junction is formed between the lightly doped p-epitaxy layer and the buried n-well [1]. The P-well and highly doped p+ forms the anode contact and the deep n-well/n+ forms the cathode contact. By applying a higher reverse bias, we can create a larger depletion region and a stronger electric field. The electric field profile within this structure can be visualized in Fig.1.2b, with the help of Technology Computer-Aided (TCAD) Design simulation.

As we increase the reverse bias voltage, we will eventually reach a critical point called the breakdown voltage (V_B), at which the diode breaks down and conducts current in the reverse bias direction. This breakdown process can begin when a single electron is present in the conduction band within the depletion region. The process is illustrated in Fig.1.3. Due to the high electric field, the electron is accelerated in the depletion region. The resulting high-energy electron can collide in the semiconductor lattice and transfer enough energy to ionize the



(a) Cross section of a SPAD



(b) Top to bottom shows the electric field profile of the illustrated SPAD with increasing reverse biased voltages.

Figure 1.2: Example of a SPAD structure and its electric field profile at different voltages.

atom; this process is known as impact ionization. It frees one bound electron from the valence band to the conduction band, resulting in an electron-hole pair. The newly free electron can also be accelerated in the electric field and create more electron-hole pairs, which leads to a chain reaction.

SPAD operates above breakdown voltage, at V_{op} , in a metastable state. This can be visualized as the dot in Fig.1.4a. That is, the diode normally **does not** conduct current until a carrier triggers the avalanche breakdown.

Once the avalanche is triggered, a self-sustaining current will flow through the diode. To prevent damage to the SPAD, a quenching resistance is used to limit the current flow during the avalanche process. This can be seen in Fig.1.4b. Once current flows through the resistance, the voltage at the anode of the SPAD increases and results in the voltage across the diode dropping to V_B , which quenches the avalanche process. The SPAD is then recharged back to V_{op} for the next event. The profile of the resulting electrical signal seen by the output in Fig.1.4b is due to the capacitance and resistance of the junction and the quenching resistance, which will be discussed in more detail in Appendix A. The output voltage has a maximum height of $V_B - V_{op}$, which is usually known as the excess bias voltage, V_{ex} . In order to determine

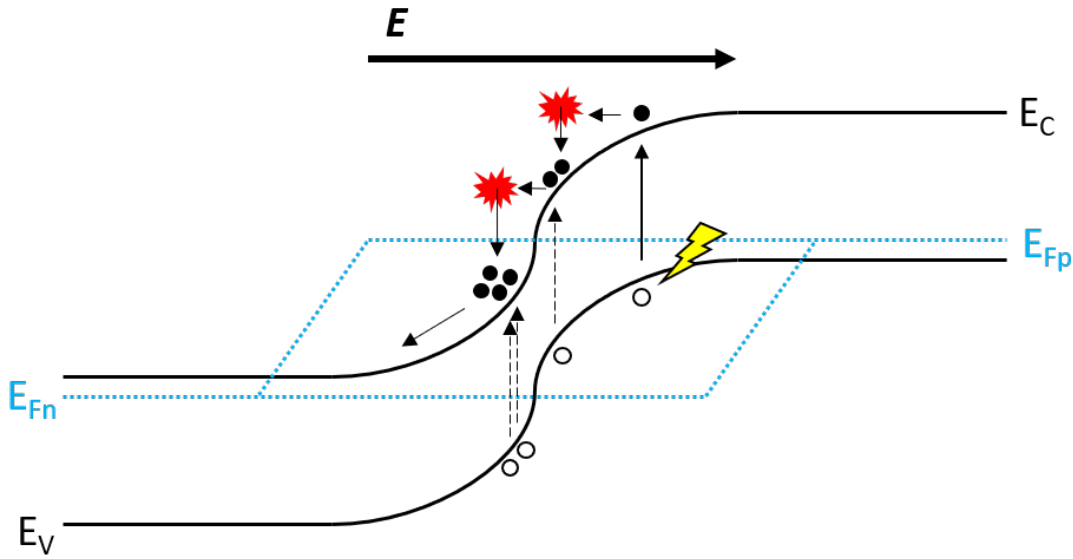


Figure 1.3: An electron is first excited from the valence band to the conduction band. Due to the high electric field, the electron is accelerated in the depletion region. The accelerated electron impacts the lattice and frees more electrons from the valence band, creating a self-sustaining avalanche process. E_{Fn} and E_{Fp} represent the quasi-Fermi levels.

whether the SPAD has fired, this voltage signal is generally sent to an inverter or a comparator, which outputs a digital pulse. This digital output can then be processed to perform more complex tasks such as timing measurements or counting.

As mentioned previously, an avalanche breakdown can be initiated when a primary carrier, such as an electron, is present in the conduction band. One way to generate such a carrier is through photoexcitation. When a photon with sufficient energy strikes a bound electron in the valence band, the electron can be excited to the conduction band. With this process, SPADs achieve single-photon sensitivity.

The energy of the photon must be greater than the bandgap energy, E_g , to create photoexcitation. We can calculate the minimum photon energy required using the Planck relation $E = h\nu$, where h is the Planck constant ($4.1 \times 10^{-15} \text{ eV}\cdot\text{Hz}^{-1}$) and ν is the photon frequency. Silicon, for instance, is an indirect bandgap material, i.e. the minimum in the conduction band is not located at the same momentum in the k -space as the maximum in the valence band. Therefore, the probability of electron excitation is low unless an additional phonon is present to conserve momentum, as illustrated in Fig.1.5. It is also the reason why silicon SPADs typically have good photon response only within the visible photon range. For applications that require SPADs to detect lower energy photons in the infrared region, one will need smaller bandgap materials such as germanium or InGaAs. Conversely, the maximum photon energy that a SPAD can detect, it depends on the absorption coefficient of the material. Higher energy photons have a higher absorption coefficient and therefore are mostly absorbed at the surface

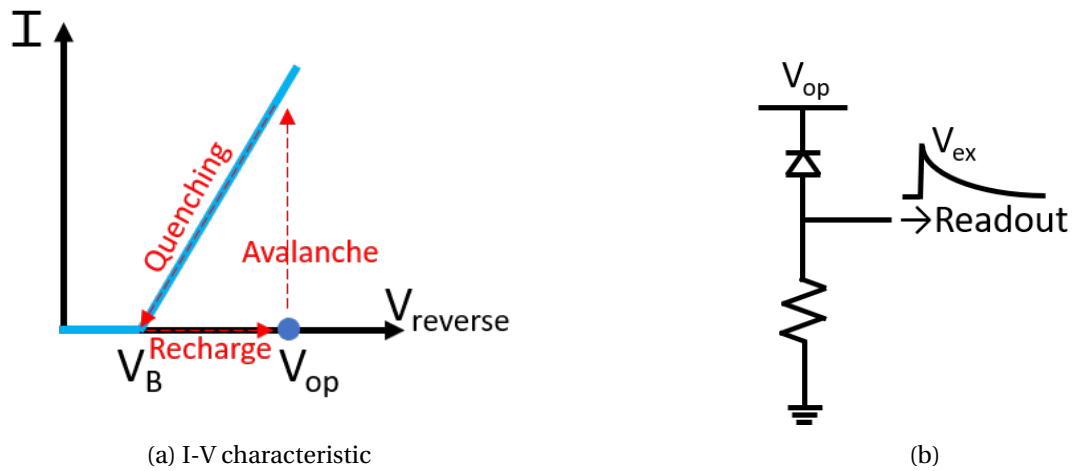


Figure 1.4: SPAD operation and I-V characteristic and basic circuit configuration. The dot at V_{op} represents the metastable operating point.

of the semiconductor, while lower energy photons can penetrate deeper. This is why the depth of the depletion region plays an important role in the detection efficiency of photons at different wavelengths. Typically, one will prefer a shallower depletion region to detect higher energy photons.

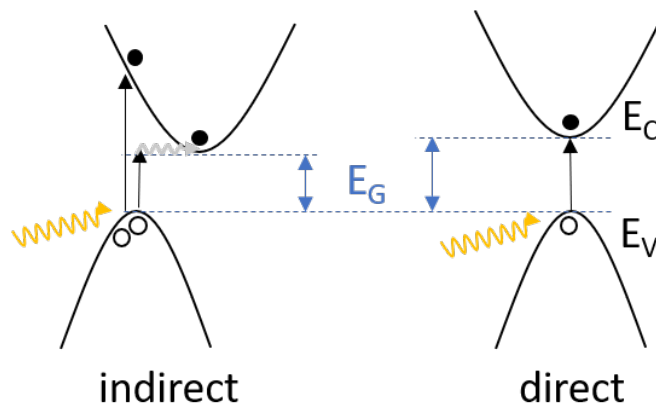


Figure 1.5: Direct bandgap materials can absorb photon energy equivalent to the bandgap directly. In the case of indirect bandgap materials, they require the assistance of additional phonons to absorb photons with energy equivalent to the bandgap.

As any carriers present in the depletion region can trigger an avalanche, carriers not generated by photons can also result in signals. For example, an electron can be thermally generated from the valence band to the conduction band, or it can undergo tunneling, either band-to-band or with the help of a trap within the bandgap. The resulting signals that are not caused by a photon are considered noise, which is quantified as the dark count rate (DCR). The DCR is an important performance metric for SPADs, as it affects the device's ability to detect weak

signals in the presence of noise, thereby impacting the signal-to-noise ratio (SNR). The carriers can also be generated by ionizing radiation, which will be explored later in this thesis.

1.2 Overview of SPADs

This section provides key figures of merit to evaluate the performance of SPADs. It also discusses the commonly seen architecture of SPAD-based systems. The characterization method of these figures of merit is presented in Appendix A.

1.2.1 Dark count

DCR is measured in counts per second, [cps]; it can also be normalized, measured in cps per unit area [cps/ μm^2]. Dark counts arise primarily from thermal effects, making the operating temperature of a SPAD critical to determine DCR. The generation rate of dark counts increases with temperature and reduces with cryogenic temperatures up until about 77K, after which it may increase again. Therefore, adjusting the operating temperature offers a means to mitigate this noise. The generation process of dark counts can occur with or without trap assistance, following the principles of the Shockley-Read-Hall theory. The presence of traps, which act as generation-recombination centers, directly affects the generation rate and, consequently, DCR. Therefore, controlling the concentration of undesired traps becomes a significant factor in ensuring a clean fabrication process.

Operating under high reverse bias, SPADs experience changes in the energy barrier for carrier transport in silicon due to the presence of a high electric field. This creates the potential for tunneling and the Poole-Frenkel effect, which refers to trap-assisted electron transport occurring under high electric fields. While these processes are less sensitive to the operating temperature, they are highly influenced by the SPAD's operating voltage.

During the avalanching process, existing traps can capture charges due to the generation of a large current in the depletion region. These trapped charges can be subsequently released after the SPAD is recharged [2], leading to a phenomenon known as **afterpulsing**. Afterpulsing introduces additional noise into the system, originating from either a photon or another noise event. Consequently, it creates unwanted correlations in counts.

1.2.2 Photon detection probability

The photon detection probability (PDP) refers to the ratio between the number of detected photons and the total number of photons impinging on the active area of the SPAD. It is important to note that not all photons are detected, as the probability of being absorbed within the active region is less than 100%. This is why having a wider active region is desirable, as it improves the detection efficiency. Additionally, the wavelength of the photons also plays a role, as the absorption coefficient is wavelength-dependent.

Once a photon is absorbed in the active region, the excited carriers have a probability of triggering an avalanche. The product of these two probabilities gives us the PDP. It is worth mentioning that the PDP exclusively considers the active area. However, when implementing SPADs in larger systems, the readout electronics occupy space and thus reduce the effective active area. This results in a limited active area ratio within a single pixel of the SPAD, known as the fill factor. If photons are absorbed outside the active area, they will never be registered. Therefore, it is possible to quantify the photon detection efficiency (PDE) as $\text{PDP} \times \text{fill factor}$.

1.2.3 Timing jitter

Upon impinging the detector, the registration of a photon by the timing electronics involves a certain time delay. This delay is influenced by two possible scenarios: when the photon is absorbed in the high field region, leading to an avalanche with a specific build-up time, or when it is absorbed in a low field region, necessitating the drifting and diffusion of the generated electron-hole pair to the high field region for avalanche triggering. The distinct time requirements of these processes result in timing uncertainty, commonly referred to as timing jitter.

The timing jitter in a SPAD comprises two components: a Gaussian statistics arising from the avalanche build-up time and an exponential timing uncertainty caused by carrier diffusion, as modeled in [3]. To quantify timing jitter, the full-width-at-half-maximum (FWHM) of the overall instrument response function is commonly used. As drift is influenced by the electric field, maximizing the electric field is desirable to expedite carrier drift, thereby improving timing uncertainty.

1.2.4 SPAD-based systems

SPADs can be implemented as single-pixel detectors, shown in Fig.1.6a, offering advantages such as a larger detection area and the ability to incorporate more complex readout and feedback electronics. This design approach enables the development of systems with high detection efficiency. Additionally, the incorporation of more complex electronics allows for improved timing performance and faster reset, making them suitable for high count rate applications. The circuit shown in Figure 1.7a represents an example of a SPAD pixel circuit featuring an active recharge implementation. The active recharge loop provides a way to adjust reset time and pulse width. Additionally, thick-oxide transistors and a cascode architecture are employed in this circuit to allow higher operating voltage, as the transistors share the excess voltage above breakdown, thereby preventing damage [4].

SPAD arrays offer increased flexibility and additional degrees of freedom for various applications. These arrays can be designed in different formats, including 1D linear arrays, 2D planar arrays, and 3D stacking configurations. A simplified circuit architecture suitable for large-format arrays is depicted in Figure 1.7b. In this configuration, passive quenching and

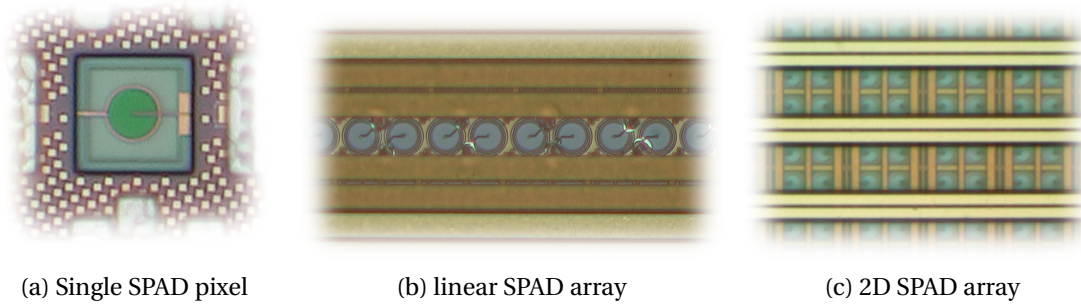


Figure 1.6: SPAD-based systems

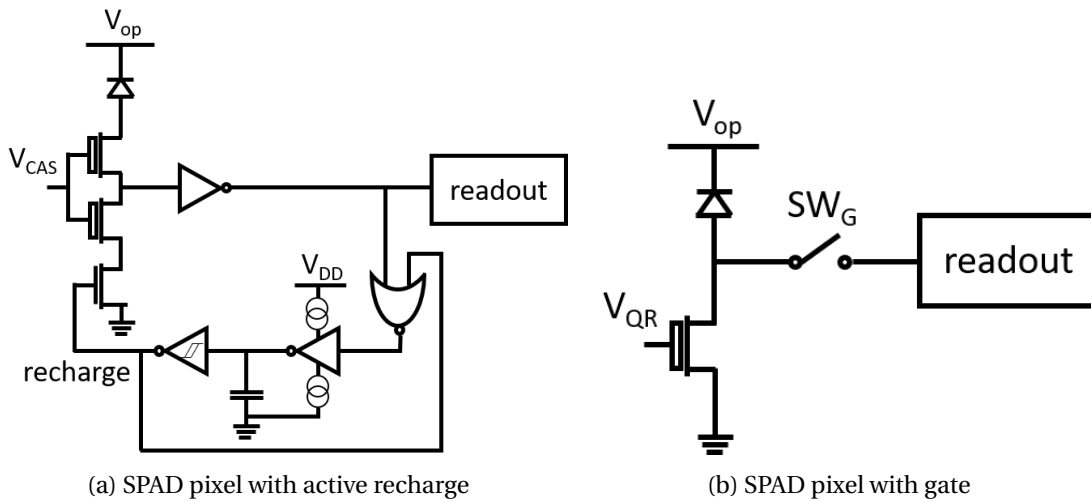


Figure 1.7: SPAD pixel circuits

recharge are controlled by voltage V_{QR} . The gate switch SW_G enables the SPAD's anode to be registered by the readout.

A 1D linear array of SPADs, shown in example Fig.1.6b, enables single-shot measurements and is particularly suitable for applications that require 1D information, such as spectroscopy applications. The spectral dimension can be projected onto the 1D SPAD array, allowing for efficient data acquisition. Additionally, the linear array can replace single-SPAD pixels when scanning is required.

A planar array of SPADs, shown in example Fig.1.6c, provides an extra spatial dimension, making it valuable for imaging purposes. The additional dimension enhances the capability to capture detailed spatial information and can also be utilized for other types of data, such as optical spectrum analysis, which will be demonstrated later in this thesis.

In 3D-stacking architectures one separates SPADs from readout electronics using two tiers; it provides additional space to improve the fill factor. Moreover, the arrangement of positioning two SPADs on top of each other has been demonstrated to be highly valuable for coincidence

measurements in high-energy particle detection. This configuration facilitates the detection and analysis of simultaneous events, thereby expanding the range of applications in particle physics research.

As the dimension of the SPAD array increases, there is a trade-off with the available area for the readout electronics. In a 1D array, the readout electronics can be positioned outside of the array area, providing the linear SPAD array with more flexibility in terms of data processing. While a 1D array allows for more flexibility in data processing, a 2D array offers additional dimensions of information. However, in a 2D array, each pixel has limited space for readout electronics, and the 3D stacking solution may introduce additional design complexities. Therefore, the choice of architecture should align with the desired trade-offs and the specific needs of the applications at hand. This work will explore and investigate the mentioned architectures.

1.3 Harsh environments and effects

A harsh environment for electronic devices refers to operating conditions that pose significant challenges and risks to functionality. These conditions can include an extreme temperature span, exposure to radiation, vibration, and shock, high electromagnetic interference, and other challenging factors such as extreme light contrast for image sensors. Harsh environments can be encountered in various industries and applications, including aerospace, defense, automotive, space exploration, and high-energy physics beamlines. Electronic devices designed to withstand harsh environments must be engineered and tested to ensure their reliability, durability, and performance under such demanding conditions.

The emergence of fields like quantum computing has created a demand for devices capable of operating in extreme temperature environments. This requirement has driven the development of cryogenic CMOS circuits and systems. Additionally, optical sensors, such as those used for optical readout of qubit states in trapped ion quantum computing [5], have sparked research into understanding device behavior at cryogenic temperatures [6].



Figure 1.8: In space, visual environments include complex lighting situations involving phenomena like sun glare, specular reflections, and high contrast that requires a broad dynamic range. These conditions often lead to images being either overexposed or underexposed upon capture. (Image sources: NASA/SpaceX/CLEP/CNSA)

Extreme lighting conditions encountered in astrophotography pose significant challenges for astrophysics studies and astronomy observations, as well as vision systems for space

applications. Examples of these conditions can be seen in Fig.1.8. Furthermore, space and planetary exploration often necessitate imaging in low-light regions that are shadowed or located on the backside of the light source. An example of this is the observation of lunar permanently shadowed regions, which are believed to contain substantial amounts of water ice. The utilization of deep learning techniques has been proposed to interpret images captured under conditions of low resolution and signal strength [7]. In such scenarios, the dynamic range of image sensors can limit overall performance, affecting the ability to capture detailed information. The performance of SPAD-based cameras under extreme lighting conditions will be further elaborated upon in this study. Additionally, space poses a significant risk of radiation damage to image sensors and peripheral electronics. In this section, we will provide an introduction to the radiation environments and discuss its effects on electronic components.

1.3.1 Radiation environment and sources

On Earth, the impact of radiation is minimal due to the protective effects of the planet's magnetic field. Most of the charged particles from space are deflected or trapped by the Earth's magnetic field, forming the Van Allen radiation belts. These belts are regions of charged particles that are guided and accelerated along the magnetic field lines, resulting in a spectrum of particles with varying energies. When we deploy devices in space, they become more susceptible to the influx of high-energy particles depending on their operating position. These particles, including protons, electrons, and heavy ions, originate from the Sun and other celestial bodies beyond our solar system [8].

In high-energy particle studies, detectors and peripheral electronics are often positioned in close proximity or directly under the particle beamline. As a result, these devices are exposed to radiation from the primary beam. Furthermore, secondary radiation particles, generated by the interaction of high-energy particles with surrounding materials, can also cause radiation damage. These secondary particles encompass a range of charged particles as well as uncharged particles such as neutrons.

In the following sections, we will examine the potential effects of radiation on electronic devices and discuss common strategies for mitigating radiation damage.

1.3.2 Effects of radiation on electronic devices

Radiation damage can be categorized in two groups: ionizing radiation and non-ionizing radiation.

Ionizing radiation can result in two types of effects: single-event effects (SEEs) and total ionizing dose (TID) effects. Total ionizing dose (TID) effects refer to the accumulated damage caused by ionizing radiation over an extended period. Continuous exposure to ionizing radiation leads to gradual degradation in device performance, which can manifest itself as a

drift in characteristics or even complete failure.

The effects of ionizing radiation can be observed and visualized in Figure 1.9. When a charged particle, such as an electron, interacts with the material, it can undergo various transformations. These include elastic electron-electron scattering, which involves interactions with other electrons in the material. Additionally, the generation of secondary radiation may emerge through processes like Bremsstrahlung or braking radiation. Inelastic scattering can also occur, resulting in the emission of recoil electrons and characteristic X-ray photons when electrons transition from higher energy shells to lower energy shells. Photons can also cause ionizing damage through the photoelectric effect, where an incident photon is absorbed by an atom, leading to the emission of secondary X-ray photons. Additionally, pair production can occur, where a high-energy photon interacts with the nucleus and generates an electron-positron pair. Compton scattering is another process in which a photon interacts with an electron, resulting in the scattering of the photon at a lower energy and the ejection of a recoil electron. These processes demonstrate how charged particles and photons can induce ionizing damage and produce secondary particles or photons in the material.

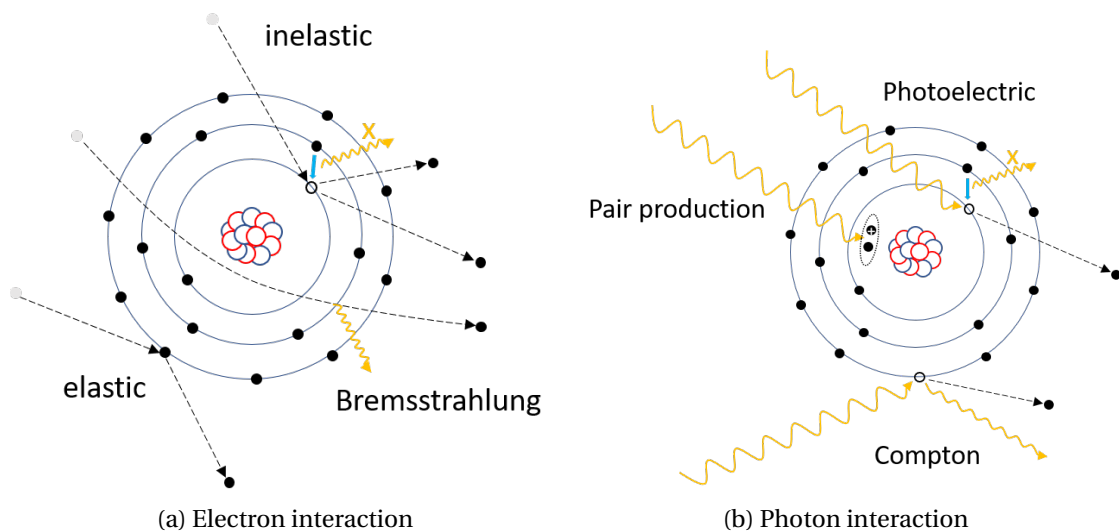


Figure 1.9: Electrons can undergo elastic scattering, inelastic scattering, and Bremsstrahlung. Photons can interact with bound electrons through the photoelectric effect, Compton scattering, and pair production.

On the other hand, single-event effects (SEEs), illustrated in Fig.1.10a, occur when a single ionizing particle interacts with electronic components, causing malfunctions or changes in their states. These effects are immediate and can result in temporary or permanent alterations in device behavior.

Non-ionizing radiation, also known as displacement damage, occurs when energetic particles displace atoms in the material, thus resulting in lattice disruption. This displacement creates vacancies and atom interstitials, as shown in Fig.1.10b, causing a disturbance in the periodic lattice structure. Consequently, energy states form within the bandgap of the material. As

previously mentioned, these energy states play a role in carrier generation and recombination processes.

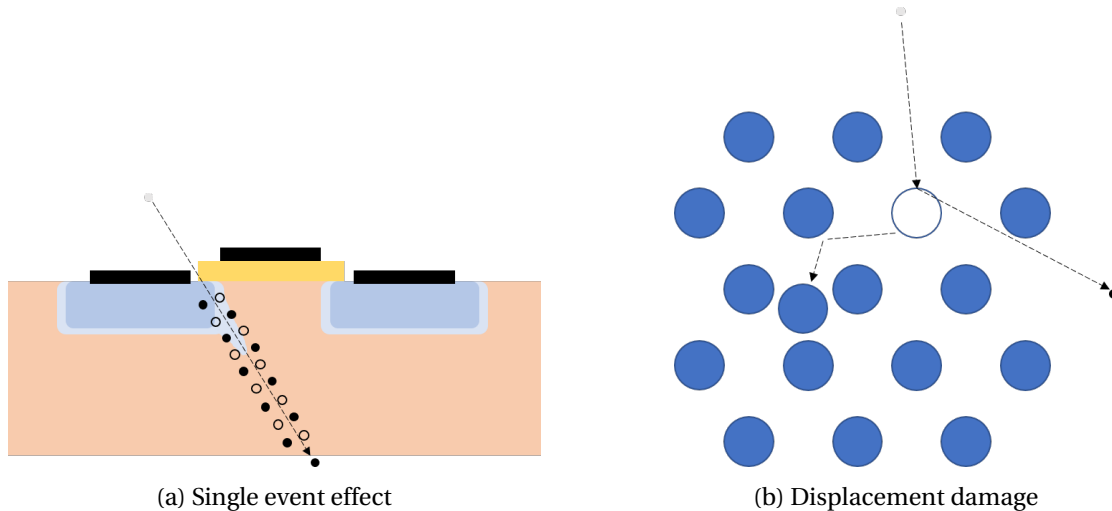


Figure 1.10: Single-event effects can create a track of electron-hole pairs within the device. Displacement damage results in the creation of vacancies and interstitials.

To quantify the ionizing and non-ionizing damage, two important metrics are commonly used: linear energy transfer (LET) and non-ionizing energy loss (NIEL).

LET [MeV/cm] is a measure of the amount of energy deposited by ionizing radiation per unit length as it traverses through a material. It provides information about the average energy deposited in the material by the ionizing particles. NIEL [MeV-cm²/g] quantifies the energy transferred to a material by non-ionizing radiation. Fig.1.11 illustrates the NIEL profile for silicon as a function of proton energy. With the fluence of the particle, we can obtain TID [rad = J/kg] and displacement damage dose (DDD) [MeV/g]. The units mentioned within the brackets are commonly used to distinguish between the dose caused by ionizing radiation and non-ionizing radiation.

In space, protons and electrons generate most of the TID radiation. Testing the radiation hardness of electronic components is crucial for assessing the risks associated with their use in radiative environments. The tests involve exposing the target samples to various types of radiation from a known radiation source, depending on the potential applications. These tests are particularly significant for electronics intended for radiation-hard applications.

The common technology used for SPADs has been evaluated in several technology nodes below 350 nm, and it has been observed that transistors can withstand TID of up to a few hundred Mrad with minimal degradation in their operational performance [9]–[12]. The assessment is not limited to individual transistors; rather, it also includes more complex components such as memories and field-programmable gate arrays (FPGAs) [13]. Furthermore, the effects of radiation have been studied extensively on various silicon-based sensors, includ-

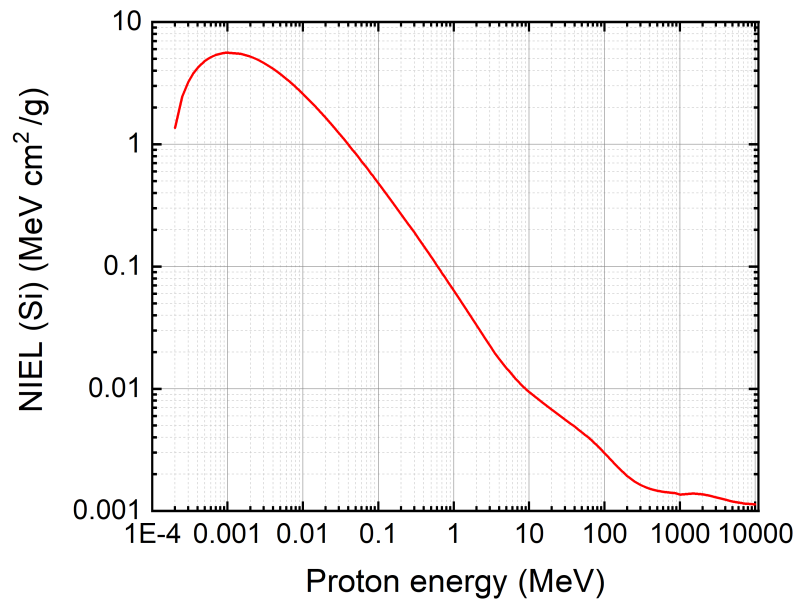


Figure 1.11: The NIEL profile for silicon as a function of proton energy.

ing photodiodes, Silicon photomultipliers, and charge-coupled devices (CCDs). Additionally, investigations have been conducted on III-V material-based photonic devices, such as ring resonators and lasers, to understand their response to radiation [14]–[20].

Studies have shown that the DCR of SPADs increases due to displacement damage caused by protons, as well as ionizing damage from X-rays, alpha particles, heavy ions, and neutrons [9], [21]–[26].

1.3.3 Mitigation techniques for radiation effects

Reducing the impact of radiation on electronic devices can be accomplished through various means, including the use of radiation-hard packaging and shielding. Shielding is a common approach employed in high radiation environments to protect both humans and electronics, such as in high-energy beamlines. However, when it comes to optical sensors, a significant challenge arises due to the lack of optically transparent shielding materials capable of effectively blocking radiation without interfering with the optical signal. Consequently, in the absence of suitable shielding options, it becomes necessary to explore alternative mitigation strategies to address the potential damage caused by radiation.

In high radiation environments, such as the radiation belt, the effects of TID on electronic devices are amplified by the electric field they experience. To minimize the risk of damage, certain electronics are powered down when subjected to these conditions, as the presence

of an electric field can exacerbate the damage. Additionally, the layout of transistors can be optimized to withstand higher TID levels. Enclosed layout transistors, specifically designed for this purpose, have been developed to enhance radiation tolerance [27]. This layout configuration provides better isolation and shielding for the transistor's active region. These measures ensure the reliability and functionality of electronic systems in challenging radiation environments.

Displacement damage leads to the formation of defects within the lattice structure of devices, which are relatively less influenced by the existing electric field. To address these defects, an effective approach is through annealing. Annealing involves providing additional energy to the lattice, facilitating the diffusion of atoms and the rearrangement of bonds, thereby mitigating the impact of displacement damage. In the case of SPADs, thermal annealing has been demonstrated to reduce DCR following exposure to radiation damage [9], [28], [29]. However, implementing thermal annealing for space applications is challenging as it requires a thermal module, which consumes significant power.

Alternatively, an innovative method involves laser annealing to locally target the active region of the SPAD. Laser annealing has been shown to effectively reduce noise in SPADs after radiation damage, offering faster recovery and greater energy efficiency [30], [31]. By focusing a high-energy laser beam onto the specific area requiring annealing, defects can be effectively mitigated without the need for a thermal module or excessive energy consumption.

In addition to annealing, another method to reduce DCR in SPAD-based systems is by lowering the operating temperature. Dark counts primarily arise from thermal generation processes, and by cooling the system, the rate of thermal generation decreases. It is important to note that in this mitigation method, the damage from radiation remains.

1.4 Applications of SPAD-based systems for harsh environments

In this section, we explore a range of applications for SPADs, with a particular focus on their use in harsh environments.

With our focus on SPADs operating in high-radiation environments, the field of space exploration emerges as a rapidly expanding area of interest. In space, radiation doses are significantly higher compared to those on Earth. Additionally, imaging in space poses a challenge due to extreme lighting contrasts. The presence of areas ranging from fully shadowed to brightly lit creates difficulties for various applications, including rover detectors. Rovers rely heavily on multiple cameras for tasks such as 2D imaging, 3D ranging, navigation, and landing. These applications specifically demand exceptional timing performance and a high dynamic range from the detectors to ensure accurate and reliable operation.

In addition, these detectors play critical roles in space missions, specifically in hazard detection, radiation detection, and material analysis. Prominent examples include instruments

1.4 Applications of SPAD-based systems for harsh environments

like ChemCam [32] on the Mars Curiosity Rover, which utilize the Laser-induced Breakdown Spectroscopy technique [33]. The instrument heavily relies on robust imaging systems capable of capturing spectral information. The ability to obtain precise and high-quality images in such challenging environments is essential for the success of these scientific investigations. Furthermore, there have been efforts to downscale advanced microscopy setups for space-based research [34]. These setups are of great significance in conducting biological studies under microgravity conditions. While CCDs and photodiodes have traditionally been the common choice for sensors in these systems, the increasing compatibility of SPADs with CMOS technology holds the potential to revolutionize the field.

SPADs, integrated with high-speed electronics, have already found wide applications in photon counting and imaging with single-photon resolution. Their unique capability for photon counting makes them suitable for various applications where conventional photodiodes and CCDs fall short. Several studies have demonstrated the impressive performance of SPAD-based imaging systems, achieving high dynamic range (>120 dB) intensity imaging [35]–[40]. Additionally, their exceptional timing performance in the range of tens of picoseconds makes them well-suited for 3D imaging, ranging, and LiDAR applications [41]–[44]. In the field of material characterization, SPADs have shown promising results in Raman spectroscopy [45]–[47] and fluorescence lifetime imaging microscopy (FLIM) [48]–[50].

In the field of quantum cryptography, particularly in satellite or space-based implementations, SPAD-based systems have proven beneficial for quantum key distribution [51]–[54] and quantum random number generation [55], [56]. By leveraging the single-photon sensitivity and precise timing capabilities of SPADs, these applications have seen significant advancements.

In terrestrial applications, where optical detectors are required to withstand harsh environments, high-energy physics studies play a significant role. The radiation levels experienced by these detectors can be several orders of magnitude higher than those encountered in space-based systems. A notable example is that of light sensors in ring-imaging Cherenkov (RICH) detectors for experiments such as LHCb [57], Belle II, and ALICE 3 [58]. These detectors are positioned in close proximity to high-energy beamlines and are designed to identify charged particles.

The design of a large-area SPAD with a $500\ \mu\text{m}$ diameter was specifically intended for radiation detection using scintillating fibers [59]. Furthermore, recent research has showcased the promise of employing 3D-stacked SPADs for direct particle detection, leveraging the ionizing radiation generated by high-energy particles [60]–[62].

All the aforementioned applications heavily rely on operating the detector system with limited resources, whether it be in terms of power or the available incoming signal. Currently, rovers, such as the NASA VIPER moon rover, require an additional light source to explore lunar permanently shadowed regions, where the lack of sufficient light poses significant challenges. In the case of rovers with a constrained power supply, obtaining solar power from these shadowed regions is extremely difficult. Therefore, the ability to perform object detection

and ranging in low-light conditions without the need for a light source would be highly advantageous. These requirements highlight the suitability of SPADs as sensors for space exploration and high-energy physics studies.

1.5 Objectives of the thesis

This thesis focuses on investigating SPADs under a range of harsh operating conditions, including radiation environments, extreme temperatures, and challenging light conditions. This research aims to provide valuable insights into the feasibility and advantages of SPADs as valid alternatives to conventional CCD and CMOS sensors in these environments.

The primary objective of this research is to assess the radiation tolerance of SPADs. Understanding how SPADs perform under various types of radiation is crucial to evaluate their reliability and suitability for space-based and high-energy physics applications. We analyze the effects of radiation on key performance indicators such as DCR, PDP, timing resolution, and overall imaging quality. Additionally, we study the mechanisms behind these radiation effects and we explore techniques to mitigate the impact of these effects on SPAD performance.

Rapid advancements in SPAD-based systems motivate this research to showcase diverse applications in the aforementioned areas. By highlighting the advantages of SPADs over other optical systems, the research aims to elevate the state-of-the-art performance and effectively tackle the challenges posed by harsh operating conditions. As a result, we aim to promote the adoption of SPAD technology in space exploration and high-energy physics applications, thereby contributing to advancements in scientific research and exploration.

1.6 Thesis structure

The thesis is organized into four chapters. Chapter 2 discusses SPAD-based systems, highlighting how these systems can be implemented as powerful tools for time-resolved applications. Chapter 3 focuses on radiation with a study conducted on SPADs and SPAD arrays investigating the impact of proton and neutron radiation. In Chapter 4, various applications of SPAD-based systems are explored, discussing insights gained from the radiation study. Finally, Chapter 5 concludes the thesis. Appendix A provides an explanation of the metrology employed to characterize SPADs in the study. Appendix B presents the gallery of devices used in this work.

2 Methods and tools

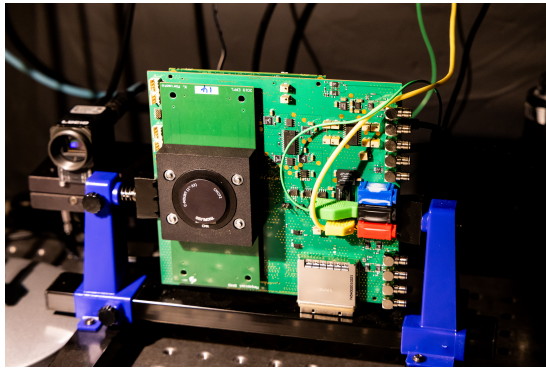
In this chapter, we focus on explaining and developing the tools used in this study. We place particular emphasis on the megapixel SPAD camera called MegaX, extensively discussed and demonstrated in [35]. This section aims to provide a brief introduction and summary of the design of the SPAD array and the development of higher-level design, highlighting its relevance to the thesis.

2.1 Sensor architecture

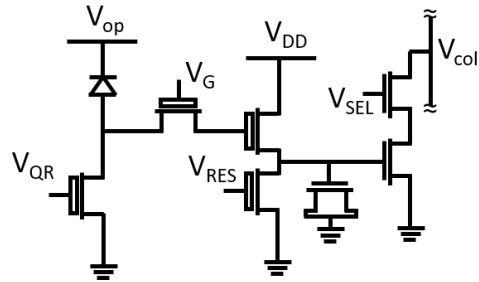
The 180 nm megapixel SPAD camera consists of two sensor architectures, each forming a 500×1024 array. One half of the sensor has a SPAD active area radius of $1.4 \mu\text{m}$, while the other half has $1.94 \mu\text{m}$. The larger SPAD is achieved with a shared readout circuit architecture. The measured peak PDP for the two halves of the camera, at a wavelength of 520 nm and with a bias voltage of 3.3 V, were found to be 10.5% and 26.7%, respectively. The measurement method used to obtain these values is explained in detail in Appendix A. These results indicate that, despite the PDP being normalized to the active area, the larger SPAD exhibits a higher detection efficiency due to having less dead area [63].

The SPAD sensor is wire-bonded to a breakout board, which is then connected to a motherboard. The motherboard supplies the power to the sensor through the use of low-dropout regulators or DC-DC converters. Additionally, it establishes the connection with FPGAs, which provide control signals. Depending on the specific application, different camera lenses can be installed using the lens mount. The camera is shown in Fig.2.1a.

To illustrate the readout process of the SPAD, we present the schematic of one of the pixels in Fig.2.1b. The pixel consists of a passive quenching active recharge transistor controlled by V_{QR} and a gate controlled by V_G . This configuration allows the voltage at the anode of the SPAD to pull up the 1-bit memory, which is implemented using a source-drain shorted transistor functioning as a capacitor. To read out the 1-bit memory, V_{SEL} is applied, causing V_{col} to be pulled low if the memory is charged. After the readout, the memory is reset by applying V_{RES} .



(a) Megapixel SPAD camera



(b) Pixel schematic

Figure 2.1: The megapixel SPAD camera and its pixel schematic

2.1.1 Intensity mode readout

The gate allows the camera to operate in two modes. The first mode is known as intensity mode, where the gate remains on throughout the exposure time window. The timing diagram for the intensity mode is presented in Fig.2.2. During the exposure, in a constant light environment, photons arrive at a rate determined by the light intensity. We define the photons that arrive within the exposure gate and trigger an avalanche as **impinging** photons. It is important to note that any signal containing more than one impinging photon will be registered as a "1" in the 1-bit memory, representing one **measured** photon. Consequently, pile-up may occur under high illumination conditions, which will be discussed in detail in Chapter 4.

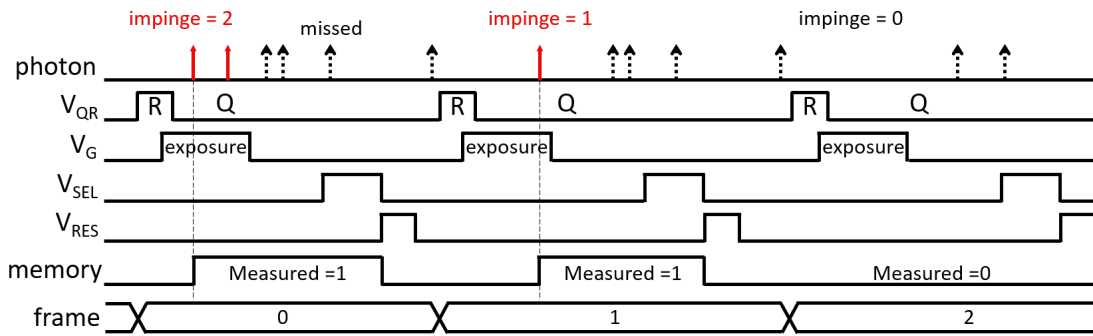


Figure 2.2: Timing diagram of intensity mode operation. The recharge (R) and quenching (Q) processes are controlled by V_{QR} , while the exposure gate window is defined by V_G . V_{SEL} and V_{RES} are applied to read out the selected pixel and reset the memory, respectively. The 1-bit memory registers one measured photon when the count of impinging photons is equal to or greater than one.

We developed two types of readout using the XEM7360 FPGA, each designed for different applications. The FPGA was interfaced with a Python-based graphical user interface. One of the readout methods involved utilizing the DDR3 SDRAM to stream out binary frames. The architecture for this readout method is depicted in Fig.2.3.

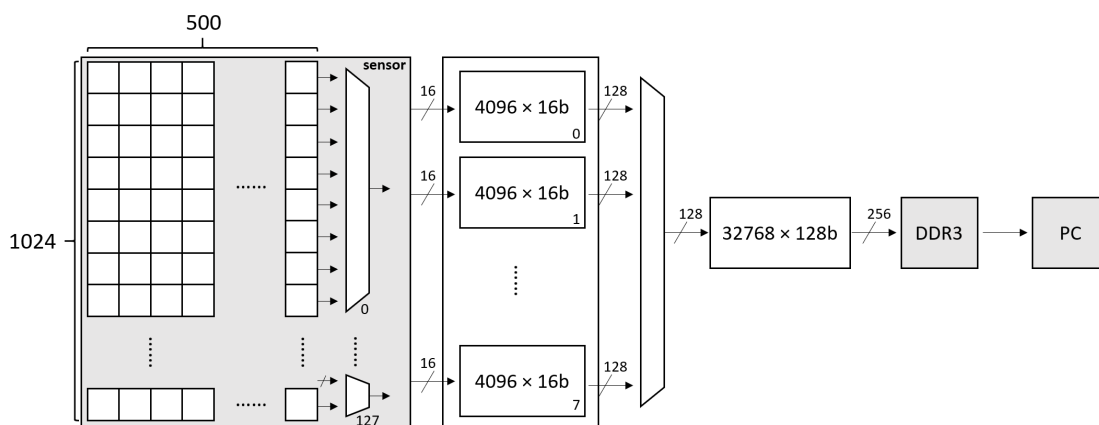


Figure 2.3: FPGA design for streaming binary images involves using FIFOs to interface the sensor chip, DDR3 SDRAM, and the PC.

The rows and columns of the SPAD array are selected by the control signals, which control the on-chip shift registers and multiplexers. The value of each memory element is then captured by the FPGA using first-in, first-out (FIFO) memories, which interface with the RAM. An example of a 1-bit image of the ISO 12233 test chart obtained from the 1-bit memory is depicted at the top of Fig.2.4. Depending on the application, the output binary images can be aggregated into multi-bit images either on the PC or on the FPGA using the available Block Random Access Memory (BRAM). Fig.2.4 and Fig.2.5 illustrate the process of combining multiple 1-bit images to form multi-bit images.

This approach, which increases the bit depth of the image, enhances the image quality by improving the SNR. It is evident that as the bit depth increases, the visibility of finer lines improves. Moreover, areas with consistent color and lighting display a greater uniformity in brightness, indicating a higher SNR where shot noise dominates the noise characteristics. The quantitative evaluation of SNR and dynamic range will be elaborated upon in Chapter 4.

Nonetheless, the achievable bit depth is constrained by the available memory resources. Moreover, increasing the bit depth entails a trade-off in the form of an extended total exposure time, assuming the same exposure time for each binary frame. This extension may be limited by specific application requirements. Therefore, when considering each application, careful consideration must be given to the system-level architecture in terms of resources, the available time for exposure for time domain oversampling [64], and the desired outcome, such as feature detection.

2.1.2 Gating mode readout

In the gating mode, the gate opens for a few nanoseconds following the delivery of a reference signal, typically generated by a pulsed light source such as a laser. The timing diagram for the gating mode is depicted in Fig.2.6. In this mode, the gate, or the exposure window, is initially

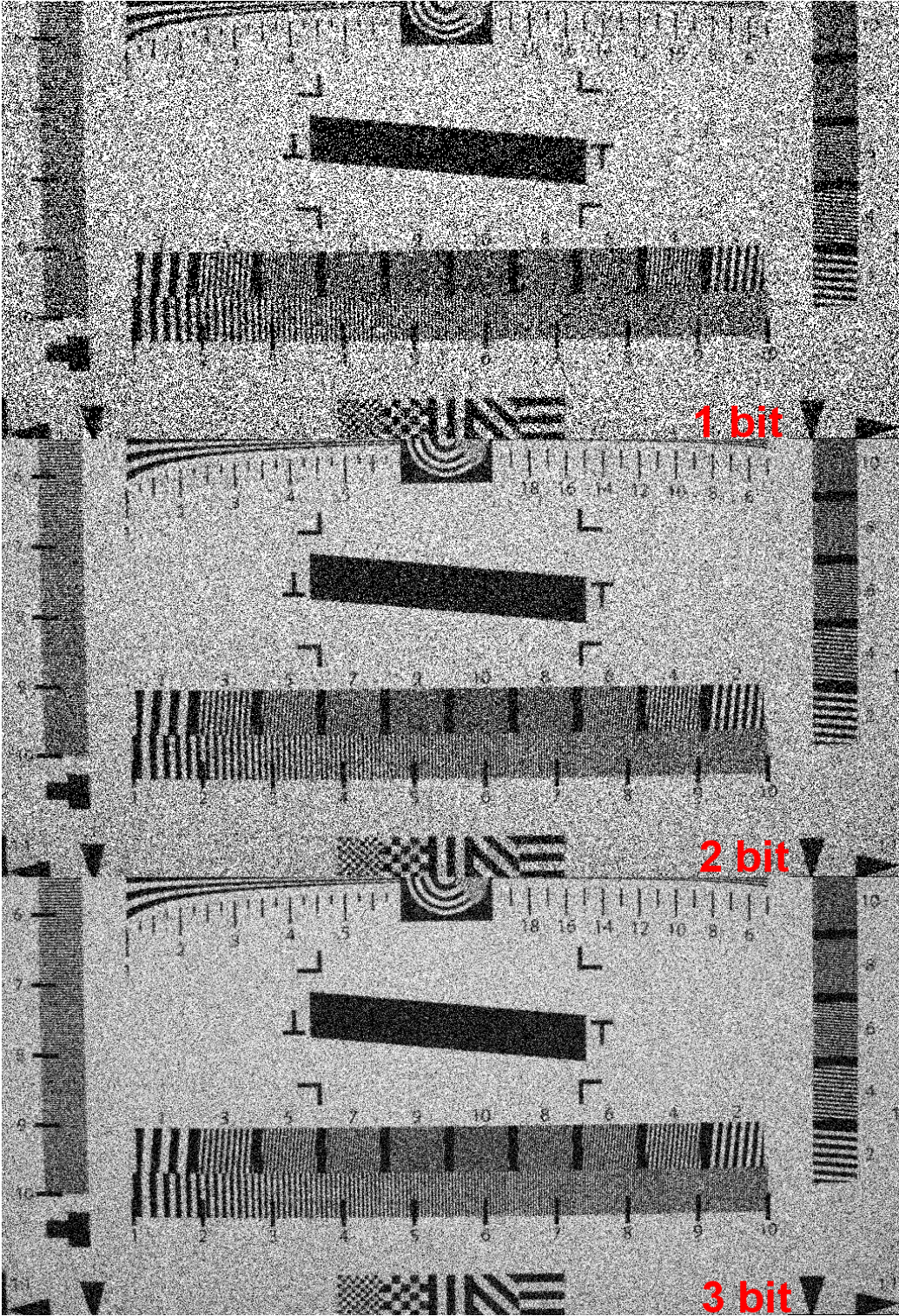


Figure 2.4: Multiple 1-bit images of the ISO 12233 test chart captured by the SPAD camera can be combined to form multi-bit images.

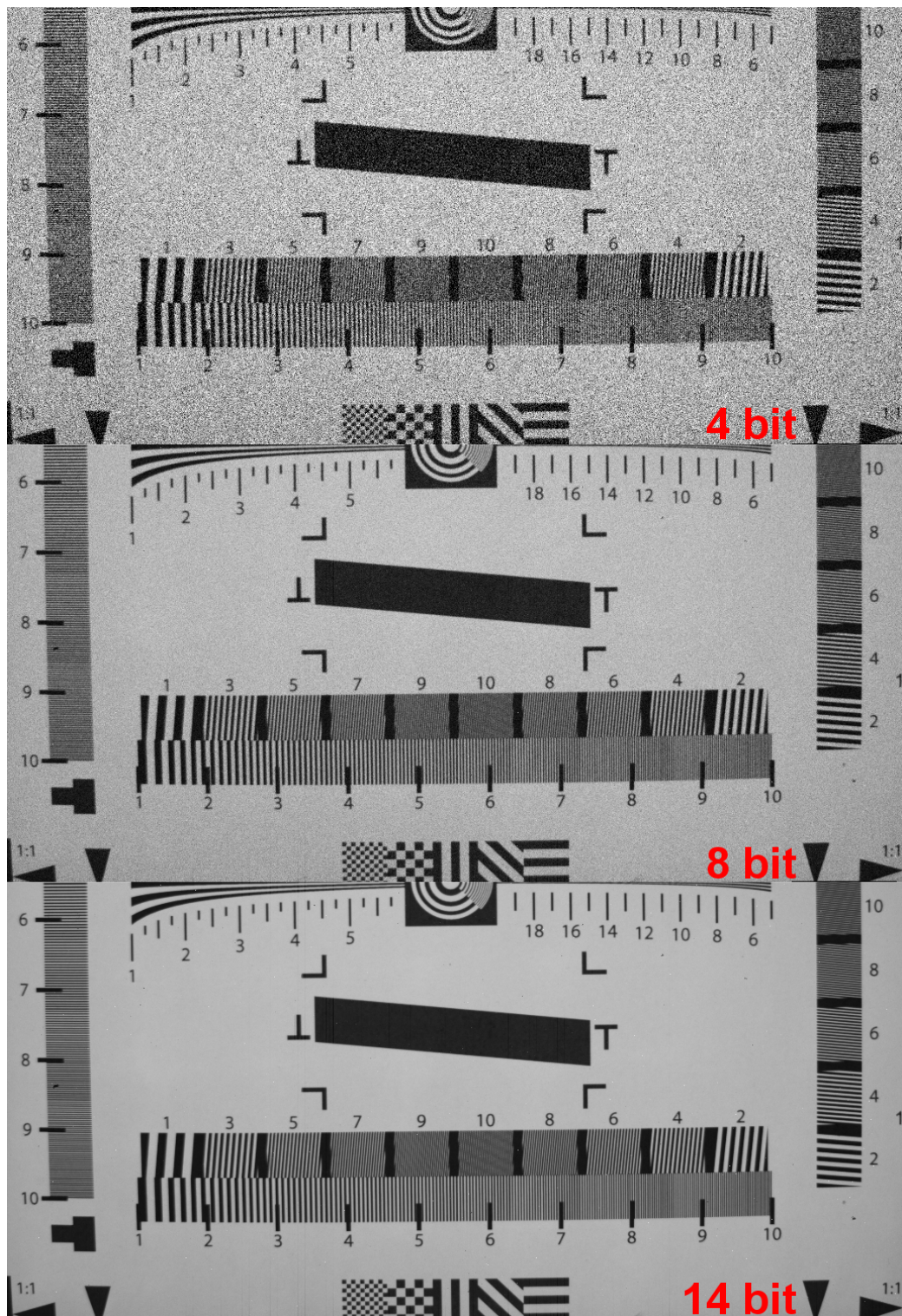


Figure 2.5: Images with higher bit depth have better image quality at the cost of memory resources and total exposure time.

aligned with the reference signal in frame 0. The gate opens multiple times within one binary frame at the same gate position. This process is then repeated to reach $2^{BD} - 1$ of frames, where BD represents the bit depth of the resulting image, forming a BD -bit image. At frame number 2^{BD} , the gate position is shifted. The resulting data is a stack of BD -bit images, with each image having a gate position that is continuously shifted.

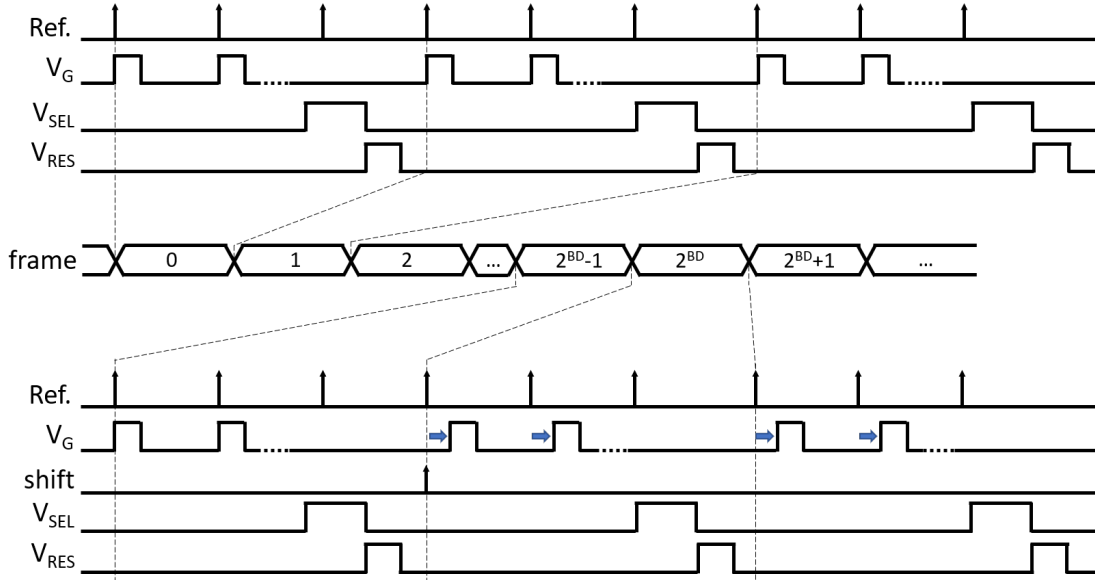


Figure 2.6: The timing diagram of gating mode operation. After capturing a BD -bit image, the gate position is shifted.

This operational mode allows the camera to exclusively register the photons that reach the SPADs within the gate window. It provides valuable timing information regarding the correlation between the pulses of the light source and the arrival time of the photons. Depending on the target applications, the gate can be finely shifted at the cost of requiring more total images to capture the entire signal profile over time.

2.2 Sensor characterization

2.2.1 Noise performance

To utilize this sensor effectively in diverse applications, it is crucial to characterize its noise performance, as it directly affects the signal-to-noise ratio. The DCR of the SPAD camera is measured by capturing multiple 8-bit intensity images in a dark environment. The firmware of the camera enables us to adjust the exposure time, which is set to an appropriate value. This ensures that the majority of the pixels experience dark counts, while only a small number of pixels become saturated due to excessive noise. Figure 2.7a displays a portion of a 15-bit image (with a maximum count value of 32640) captured by the SPAD array with an active area radius of $1.4 \mu\text{m}$. In Fig.2.7b, the same image is presented with adjusted contrast to a maximum

count of 510. By tuning the contrast, the SPAD pixels with lower DCR become visible. The resulting mean DCR of this particular SPAD array is measured to be 2.1 cps, while the median DCR is 0.4 cps.

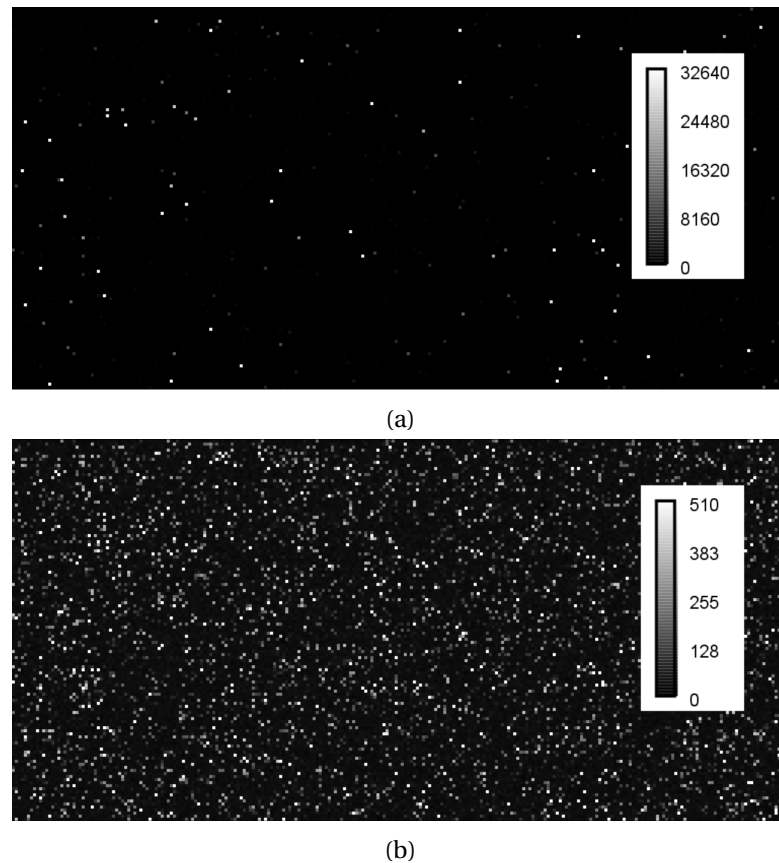


Figure 2.7: The DCR characterization of the megapixel SPAD array. In this example, the characterization is performed by exposing it to a dark environment for a duration of 64 seconds. The dark counts are typically invisible unless the contrast is tuned, except for the hot pixels.

In this case, the median DCR of the full array is considered a more reliable indicator of noise characteristics, as it is less affected by outliers such as hot pixels. Hot pixels refer to SPADs with a DCR significantly higher than the rest of the population, by more than one order of magnitude.

The distribution of DCR within the array can be visualized in terms of cumulative population or cumulative probability, as shown in Fig.2.8. The plot illustrates that 87% of the pixels exhibit a DCR lower than 1 cps. On the other hand, less than 1% of the pixels, which correspond to the hot pixels, display a DCR higher than 10 cps.

This visualization provides a clear understanding of the DCR distribution across the array and highlights the prevalence of low DCR values in the majority of pixels, while also identifying the

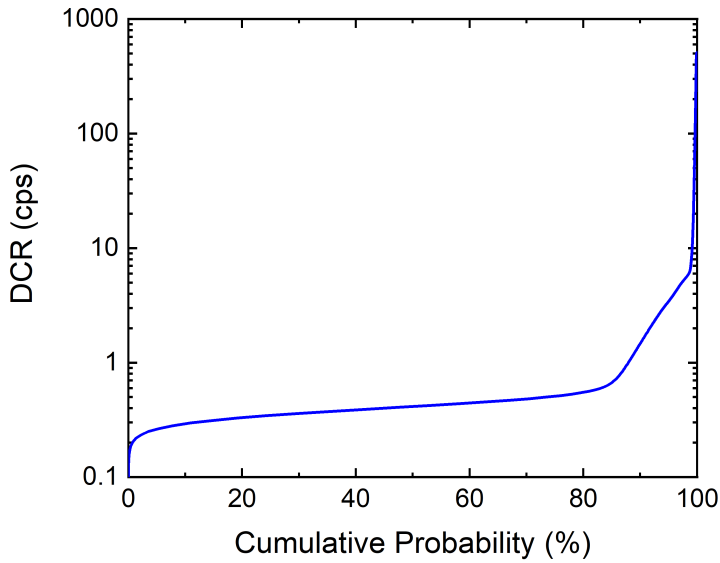


Figure 2.8: The cumulative probability plot of DCR reveals that the majority of pixels have a DCR lower than 1 cps. A small portion of hot pixels is visible on the right side of the graph.

small subset of hot pixels with significantly higher DCR. This technique will be utilized later in the thesis as a noise performance metric to investigate the impact of radiation damage on SPADs.

We conducted tests on the other half of the chip, which has a larger SPAD active area, using the same method. The measured mean and median DCR for this portion of the chip were found to be 15.7 cps and 3.0 cps, respectively.

2.2.2 Gate profile

The gating mode is a technique used to provide temporal information for time-resolved applications, as illustrated in Fig.2.9a. In this setup, a pulsed laser emits short bursts of light at regular intervals, with each burst having a specific period (T). The light from the laser is directed toward a target object, and the time it takes for the reflected photons to reach the SPAD camera needs to be precisely measured. The SPAD must be synchronized with the laser period, which determines when the gate should be open. This gate-opening window is denoted as 'g' in the figure. During this gate-opening window, the camera will register a "1" if one or more photons impinge upon the camera. To create a high-bit depth image, the camera is exposed to the reflected photon multiple times at a fixed gate position. The gate opening position is then shifted in time to capture the photons reflected with a different time of flight (TOF). Through multiple gate position shifts, we acquire an image stack, with each image representing the photon intensity at different reflecting durations.

Each image within the image stack not only contains spatial information but, more importantly, it provides valuable timing information. By focusing on a single pixel and tracking its intensity changes over time, we can construct a histogram that effectively represents the variation in reflected light intensity over time. This profile is the result of convolving the instrument response function (IRF) of the laser with the gate profile, as depicted in Fig.2.9b. Typically, the IRF of the laser is significantly shorter, below tens of picoseconds, compared to the gate window which spans nanoseconds. This difference allows us to approximate the laser IRF as a Dirac delta function. Consequently, the resulting measured profile is similar to the gate profile given by the FPGA, with the maximum photon count matching the maximum measured photon count in each frame.

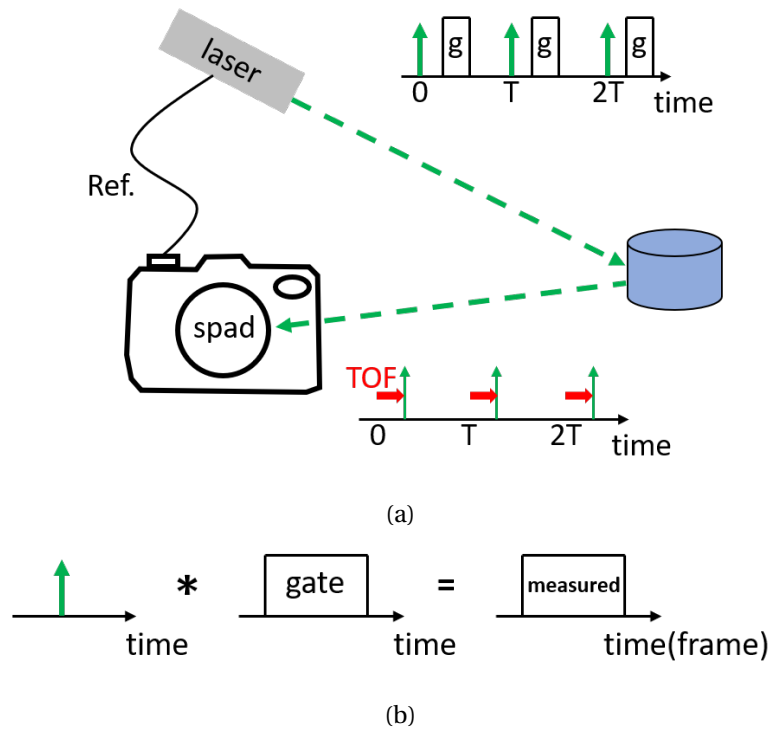


Figure 2.9: The light emitted by the laser is directed towards the target and subsequently reflected back to the camera. The time it takes for the reflected light to travel from the target to the camera is denoted as the TOF. The reflected light is only detected by the camera if it arrives during the period when the gate is open (g). Therefore, the resulting profile captured by the camera is the convolution of the laser's IRF and the gate profile.

With this method, we can determine the distance d to the target object using the formula:

$$d = c \cdot \frac{TOF}{2}, \tag{2.1}$$

where c represents the speed of light.

To utilize this technique for other timing applications, it is necessary to characterize the gate profile using a similar approach. We illuminate a flat surface moderately with a pulsed laser,

which serves as a Dirac delta light source. In this example, an 8-bit image is captured at each gate position. The gate is then shifted by 72 ps per frame, controlled by the FPGA, for a total of 200 frames. Fig.2.10 illustrates the example of the resulting measured profile for a single pixel of the camera. It is worth noting that the edge of the gate exhibits a slight tapering effect, which can be attributed to the rise and fall time of turning on and off the gate transistor. The fluctuation in the measured counts demonstrates how Poisson noise can impact the measured gate profile. In this scenario, the gate length, which is defined as the FWHM, spans across 50 frames, corresponding to a gate width of $50 \times 72 \text{ ps} = 3.6 \text{ ns}$. The acquired gate profile can then be used as the IRF of the system, which encompasses the characteristics of both the laser and the camera. It is important to note that there are slight variations in the travel distance of the gate control signal from the FPGA to each pixel. As a result, each pixel will exhibit a slightly different gate profile and timing. This variability in timing characteristics can be visualized in the subfigure of Fig.2.10. The timing variation is particularly prominent at the rising and falling edge of the gate. This indicates that the timing characteristics vary among different pixels of the camera, and it is crucial to consider these variations when operating in the gating mode.

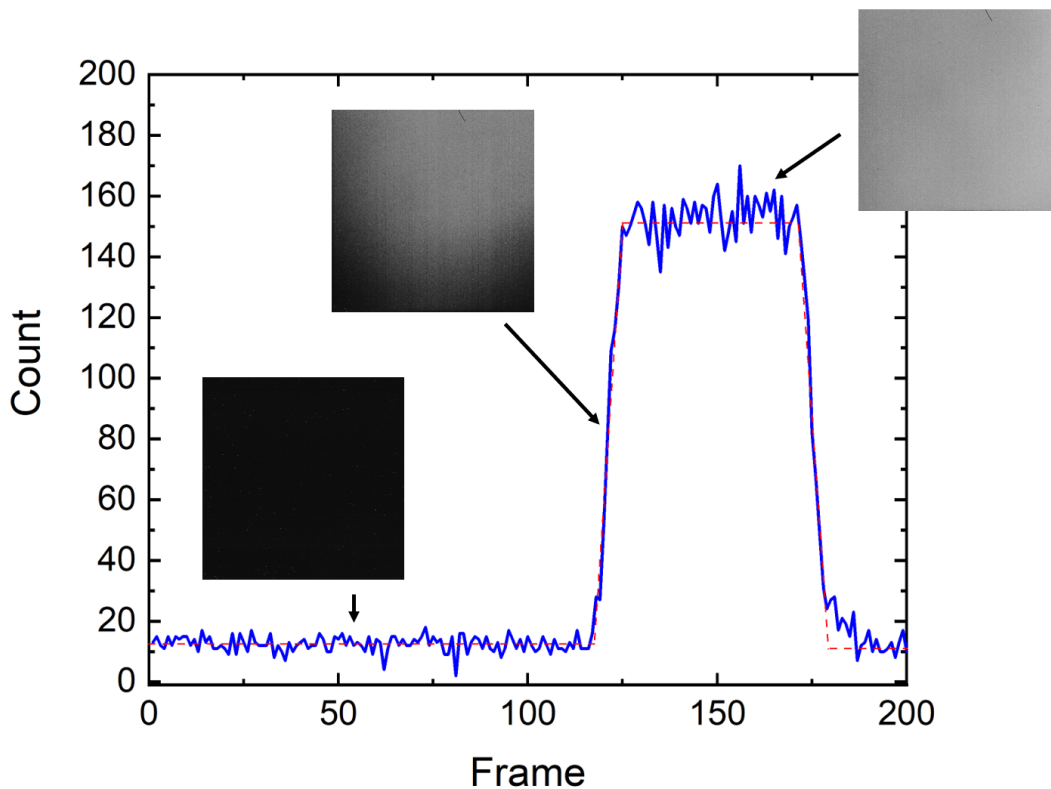


Figure 2.10: An example of the gate profile characterization for the megapixel SPAD camera. The subfigure depicts the timing variation of different pixels at the rising edge of the gate.

Once the gate profile is characterized, the IRF of the SPAD and laser system can be used to

capture any target photon source that exhibits a periodic change in intensity over time. The intensity profile of the target over time can be obtained by performing a deconvolution of the known IRF of the system, as depicted in Fig.2.11. Since the intensity of each frame is a discrete function, discrete deconvolution can be applied to determine the target intensity profile. It is important to note that each pixel has a distinct gate profile, resulting in a unique discrete deconvolution for each pixel. However, this process can be time-consuming due to the large number of pixels. To address this issue, alternative methods like machine learning can be employed to accelerate data processing, which will be discussed in detail in Chapter 4.

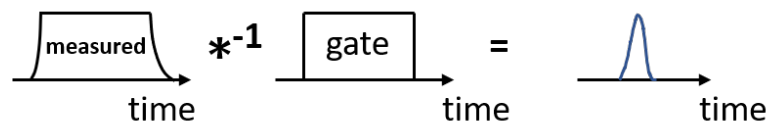


Figure 2.11: By applying deconvolution, the intensity profile of the light source can be obtained from the measured photon profile and the known gate profile.

In the forthcoming chapters, we will leverage both intensity and gating mode to gather information in multiple dimensions, including spatial, temporal, and spectral domains.

3 Radiation hardness study of SPADs

To determine the feasibility of implementing a SPAD-based system in harsh environments, such as space or a particle beamline, it is crucial to investigate the response of SPADs to radiation. In this chapter, we study the influence of proton and neutron radiation on all the figures of merit of SPADs, including DCR, afterpulsing probability, timing jitter, and PDP. The tests were conducted on different SPAD-based systems to study the influence of SPAD structures, technology nodes, and sizes. The results presented in this chapter are based on [65].

3.1 Proton radiation

We first studied the damage to SPADs caused by protons, which are the primary particles present in the Van Allen radiation belts, the solar wind, and the galactic cosmic ray background. Proton can induce both ionizing damage and displacement damage. These damages are quantified by the total ionizing dose (TID) and displacement damage dose (DDD), respectively.

3.1.1 Materials and methods

We irradiated the devices under test (DUTs) using the Proton Irradiation Facility at Paul Scherrer Institute (PSI, Villigen, Switzerland), which supports mono-energetic beams with tunable flux. The protons were collimated into a 30 mm square area with less than 10% non-uniformity. We chose 100 MeV and 10 MeV protons, which are proton energies commonly found in the Van Allen radiation belts, to investigate the effect of proton energy on SPADs. To obtain these energies, we utilized a 230 MeV accelerator source and incorporated degraders, which resulted in an actual delivered energy of 101.34 MeV and 10.29 MeV, respectively. This can be visualized in Fig.3.1a. We adjusted the proton flux, which corresponds to the dose rate, to achieve specific dose increments within a reasonable irradiation period. We set the DDD steps the same for both 100 MeV and 10 MeV protons. The dose steps can be found in Table.3.1.

Table 3.1: Dose steps with target DDD and corresponding TID for 100 MeV and 10 MeV protons.

Dose steps	DDD (TeV/g)	100 MeV			10 MeV		
		TID (krad)	Flux (proton/cm ² /s)	Total fluence (proton/cm ²)	TID (krad)	Flux (proton/cm ² /s)	Total fluence (proton/cm ²)
0	0	0	0	0	0	0	0
1	20	0.63	1.6×10^7	6.78×10^9	1.18	1.0×10^7	2.16×10^9
2	40	1.26	1.6×10^7	1.36×10^{10}	2.36	1.0×10^7	4.32×10^9
3	60	1.89	1.6×10^7	2.03×10^{10}	3.83	1.0×10^7	6.48×10^9
4	100	3.15	3.0×10^7	3.39×10^{10}	5.89	1.0×10^7	1.08×10^{10}
5	150	4.72	3.0×10^7	5.08×10^{10}	8.83	1.0×10^7	1.62×10^{10}
6	200	6.30	3.0×10^7	6.78×10^{10}	11.8	1.0×10^7	2.16×10^{10}
7	300	9.45	6.0×10^7	1.02×10^{11}	17.7	1.0×10^7	3.24×10^{10}
8	400	12.6	6.0×10^7	1.36×10^{11}	23.6	1.0×10^7	4.32×10^{10}
9	500	15.8	1.0×10^8	1.70×10^{11}	29.5	1.0×10^7	5.40×10^{10}
10	600	18.9	1.0×10^8	2.03×10^{11}	35.3	1.0×10^7	6.48×10^{10}
11	700	22.1	1.0×10^8	2.37×10^{11}	41.2	1.0×10^7	7.56×10^{10}
12	800	25.2	1.0×10^8	2.71×10^{11}	47.1	1.0×10^7	8.64×10^{10}
13	900	28.3	1.0×10^8	3.05×10^{11}	53.0	1.0×10^7	9.72×10^{10}
14	1000	31.5	1.0×10^8	3.39×10^{11}	58.9	1.0×10^7	1.08×10^{11}

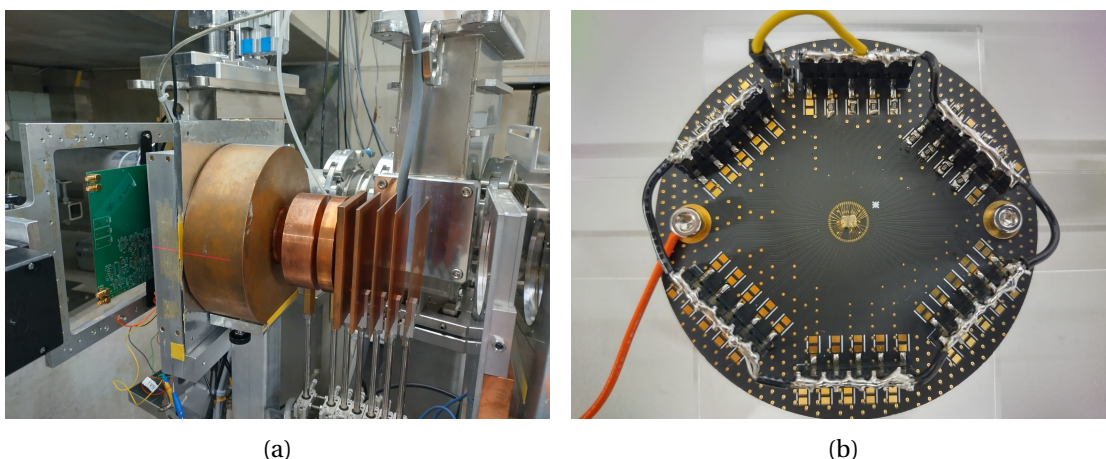


Figure 3.1: (a) The degraders in the proton beamline allow for tunable proton energy. (b) The DUTs that are exposed to proton radiation.

Higher energy protons interact less, or have a lower LET, with the silicon lattice compared to lower energy protons. As a result, devices irradiated with 100 MeV protons received only 31.5 krad TID compared to devices irradiated with 10 MeV, which received 58.9 krad TID.

Several types of SPADs were selected as the DUTs, including 55 nm Bipolar-CMOS-DMOS (BCD) SPADs with either deep or shallow junctions, with radii ranging from 1.6 μm to 4.6 μm [66], [67], a 180 nm CMOS megapixel SPAD camera with 1.4 μm radius SPADs [35], and high precision timing SPADs with radii of 8.8 μm and 21.4 μm [68].

To assess the characteristics of the samples at each DDD level, we wire bonded the 55 nm SPADs to a printed circuit board with 150 $\text{k}\Omega$ passive quenching resistors. An example of the DUT is depicted in Fig.3.1b. The SPAD pulses were then digitized through an array of LP339 comparators and accumulated using an XEM7360 FPGA. The DCR was determined by measuring the number of pulses per second and was defined as the average count per second (cps) from a one-minute measurement in the dark. The DCR of the megapixel SPAD arrays was determined by capturing images under known exposure time in a dark environment. To avoid room-temperature annealing and obtain the highest DCR level, all DCR measurements were taken within 10 minutes after reaching every dose step.

3.1.2 Results

The DCR level was measured at each dose step. As for afterpulsing probability, PDP, and jitter, only the performance before and after irradiation is compared due to the long measurement time required.

Breakdown voltage

The deep and shallow junctions of the 55 nm BCD SPADs exhibit breakdown voltages of 32 V and 19.5 V, respectively, when operating at room temperature [66], [67]. On the other hand, the 180 nm CMOS accurate timing SPAD [68] and the megapixel SPAD camera [35] show breakdown voltages of 22 V and 22.8 V, respectively. The breakdown voltage of a passively quenched SPAD can be determined by subtracting the output pulse voltage measured at the anode from the operating voltage. In the case of SPADs with front-end circuitry, the breakdown voltage of the array can be obtained by measuring the detector output counts at different operating voltages under uniformly illuminating conditions. The breakdown voltage can then be defined as the intercept on the operating voltage axis [69]. Our results, shown in Fig.3.2 show no change in the breakdown voltage of the 180 nm SPADs after the final step of irradiation. The 55 nm SPADs also show the same outcome, which is consistent with previous studies [70], [71] indicating that there is no significant change in doping profile after reaching a DDD of 1 PeV/g.

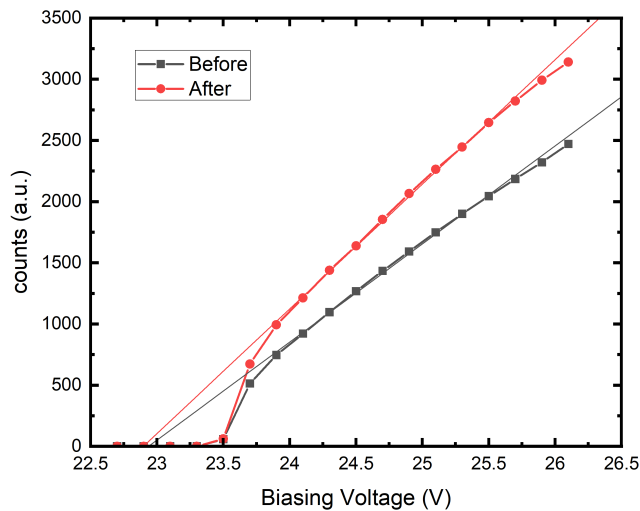


Figure 3.2: Example of breakdown voltage, represented by the intercept on the operating voltage axis, showing no changes before and after proton irradiation.

Dark count rate

Higher DCR can result in lower image quality or signal-to-noise ratio for imagers. In single-photon counting applications, such as quantum key distribution, the noise of the single-photon detector can contribute to the error rate of key transmission. If DCR exceeds a certain threshold, it may cause the failure of the quantum communication protocol [72]. The impact of radiation damage on DCR is presented in the following. Fig.3.3 displays four 55 nm SPADs and DCR measurements performed at five different excess bias voltages (V_{ex}). The cumulative

DDD and TID are indicated on the lower and upper horizontal axes, respectively. The effect of increasing cumulative dose on DCR is illustrated by four behaviors. The first SPAD in Fig.3.3a exhibits a continuous rise in DCR as a function of cumulative dose. The second SPAD in Fig.3.3b displays a peak in DCR at a certain dose, followed by a decrease during irradiation. This behavior is counter-intuitive but was reported in [23] as a short-term relaxation. The third SPAD in Fig.3.3c exhibits a stepwise increase in DCR, which, to the best of our knowledge, has not been reported elsewhere at the time of this thesis writing. Multiple SPADs demonstrate a mixture of the above behaviors.

We hypothesize that the stepwise increase observed in certain SPADs may be attributed to the size of the SPADs tested. The increase in DCR due to high-energy particles is dependent on the creation of damage within or close to the photocollector region of the SPAD. If the SPAD is small enough that no defects are created between dose steps in that region, no degradation of DCR will occur. There may probably be no interaction between the protons and atoms in the SPAD photocollector region. Hence, we observed SPADs that did not exhibit an increase in DCR after the DDD reached 1 PeV/g. This can be seen in Fig.3.3d. We noted that all 55 nm SPADs with active radii less than 2 μm showed either a stepwise increase or no increase in DCR at all.

The aforementioned hypothesis is supported by our observations on larger SPADs with active areas of 8.8 μm and 21.4 μm , which were subjected to 100 MeV and 10 MeV proton irradiation, respectively. The DCR of the former increased from about 100 cps pre-irradiation to 36 kcps at a DDD of 300 TeV/g, while that of the latter rose from roughly 1 kcps to 2 Mcps at a DDD of 200 TeV/g. Larger SPADs undergo worse degradation due to radiation damage. The degradation trend can be found in Fig.3.22

Fig.3.4 displays the progressive change of the cumulative DCR distribution for the megapixel SPAD arrays as the DDD increases. The DDD in TeV/g is indicated in the legend, with DDD = 0 representing the DCR prior to irradiation. The mean and median DCR of both arrays are initially similar. The extensive number of SPADs in the array allows for a more accurate comparison of the impacts of 100 MeV and 10 MeV protons.

The DCR increase is more significant in the DUT exposed to 10 MeV protons than in the one exposed to 100 MeV protons, even though both received the same total dose. This is due to the different damage created at the depth of the photocollector region, as verified by the Transport of Ions in Matter (TRIM) simulation shown in Fig.3.5. This figure shows the interaction of 10 MeV and 100 MeV protons with silicon, with the trajectories of the protons displayed in white. While 10 MeV protons interact with silicon more, 100 MeV protons penetrate the silicon chip with little scattering. The orange and red curves indicate the number of vacancies per proton per angstrom in depth created by 100 MeV and 10 MeV protons, respectively. The estimated displacement damage from 100 MeV and 10 MeV protons at the photocollector region is 7×10^{-7} and 7×10^{-6} vacancies/proton/Å, respectively. The defect counts within the active region of each pixel are estimated to be 43 and 140 for 100 MeV and 10 MeV protons, respectively,

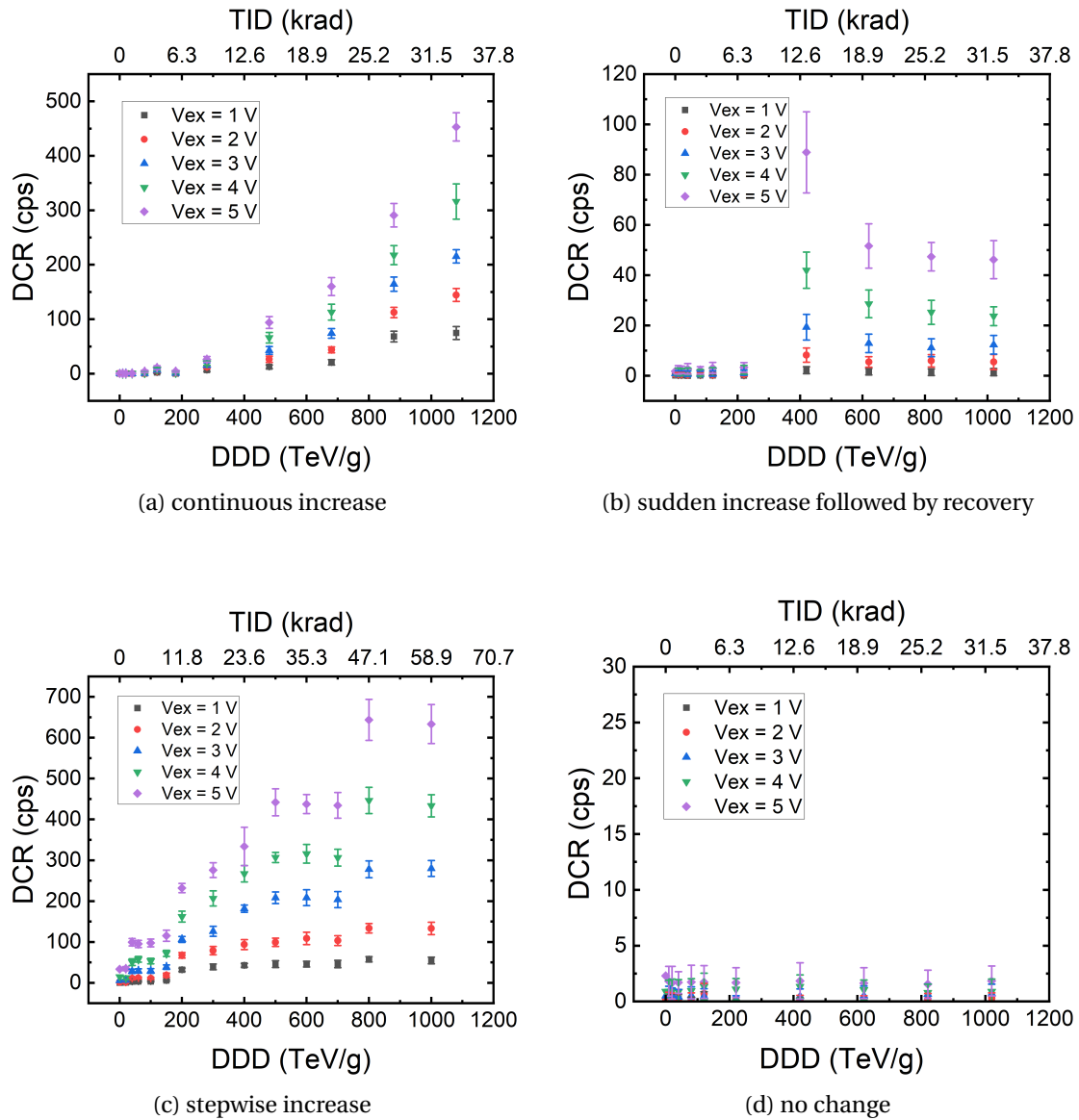


Figure 3.3: Four behaviors of SPAD DCR as observed in our experiments. Each SPAD was measured at 5 different excess biases. The four SPADs shown have active area radii of 2.43, 2, 2, and 2 μm , respectively

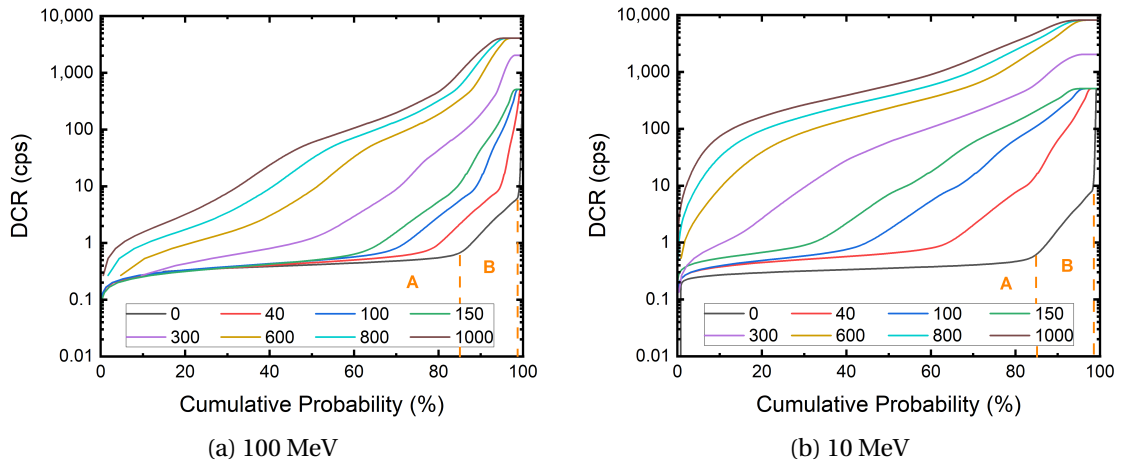


Figure 3.4: Cumulative DCR distribution of the 180 nm megapixel SPAD camera when irradiated with 100 MeV and 10 MeV protons. The DDD in TeV/g is indicated in the legend, where DDD = 0 corresponds to the DCR before irradiation. The plateau near 100% represents the saturated pixels, while the two knees at 85% and 99% cumulative probability before irradiation become less noticeable with a higher cumulative dose. Pixel groups A and B differentiate pixels with different initial DCR levels.

based on the fluences delivered shown in Table.3.1. The defect count ratio matches the ratio of the final mean DCR for both DUTs shown in Fig.3.6. The exposure of the DUT irradiated with 100 MeV protons in Fig.3.6a was discontinuous and separated into three days due to the beamtime arrangement, and the drop in mean DCR between doses on different days indicates room-temperature annealing, which will be discussed later in this chapter.

The SPAD pixels of the megapixel camera also exhibit a mixture of all four cases depicted in Fig.3.3, indicating that the four types of DCR evolution described in Fig.3.3 are not influenced by SPAD structure, doping profile, or the technology node.

The evolution of hot pixels, which are defined as pixels with significantly higher DCR than the median DCR, can be observed in Fig.3.4. Prior to irradiation, there are two distinct knees at 85% and 99% cumulative probability where the pixels show one or more orders of magnitude higher DCR than the rest of the population. This is commonly seen in large format SPAD arrays[35], [48], [73]. As the DDD increases, the knees shift towards the left, indicating a progressively increasing number of hot pixels. The variation in DCR levels is likely due to different types of defects in the silicon bulk or silicon-oxide interface, such as oxygen-vacancy, phosphorus-vacancy, boron-vacancy, and other complex defects that can emerge during fabrication or radiation exposure[74], [75]. Deep-level traps result from all of these defects. Depending on the defect type, electron and hole traps emerge at different energy levels within the silicon bandgap. The generation and recombination rate of charged particles is dependent on trap energy position, according to the Shockley-Read-Hall model and Fermi-Dirac statistics. The difference in DCR levels is likely due to varying trap energy levels. At higher cumulative doses, the knees are less apparent, indicating the formation of all defect types uniformly within

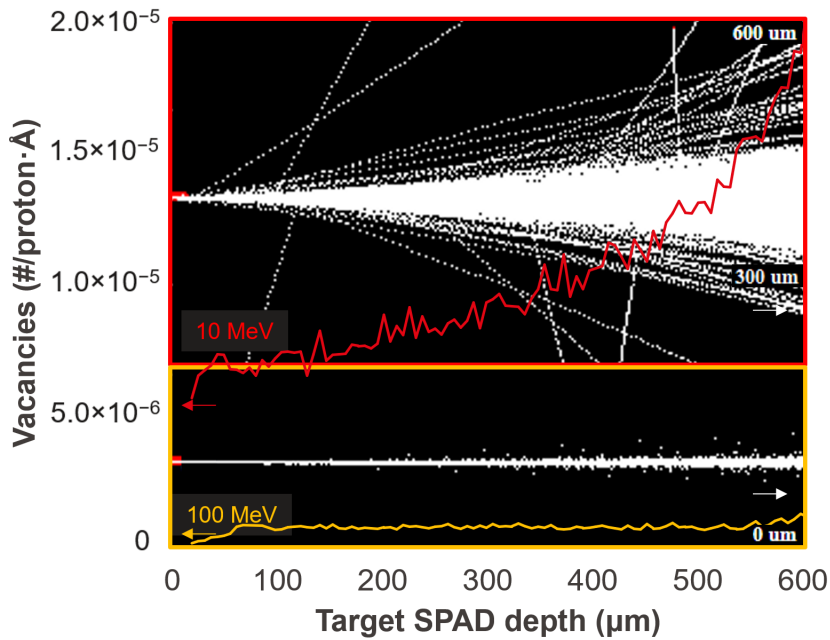


Figure 3.5: The results of TRIM simulations for 100 MeV and 10 MeV protons entering silicon from the left side. The trajectories formed by the protons are shown in white, with the 10 MeV protons interacting more with the silicon compared to the 100 MeV protons, which penetrate the chip with minimal scattering. The number of vacancies created per proton per angstrom in depth by the 100 MeV and 10 MeV protons are represented by orange and red curves, respectively. The right Y-axis shows the lateral distribution of scattered protons.

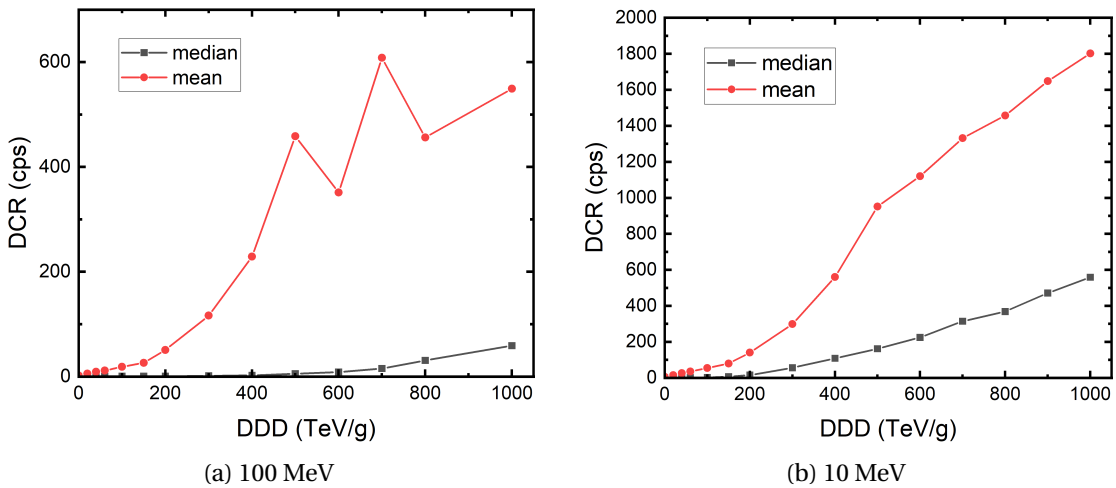


Figure 3.6: The mean and median DCR evolution of the 180 nm megapixel SPAD camera irradiated with 100 MeV and 10 MeV protons.

the array.

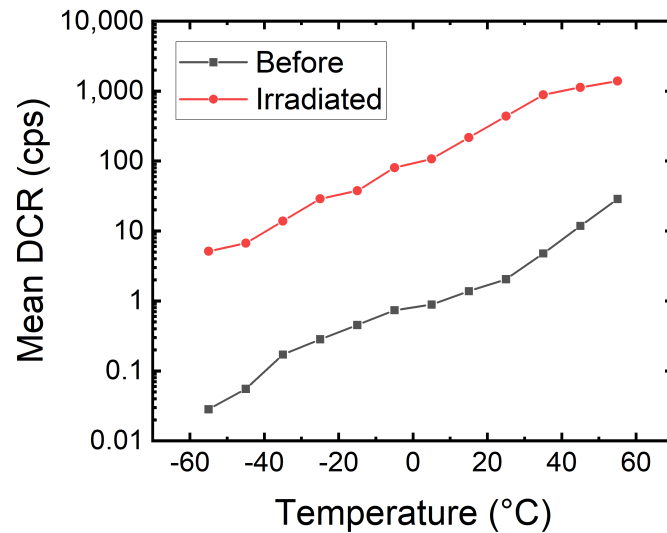


Figure 3.7: Mean DCR of the 180 nm megapixel SPAD camera at different temperatures before and after irradiation

Deep-level trap activation energy

The SPAD's DCR level can be reduced post-radiation by cooling it down. High-energy protons can create defects that serve as deep-level traps, capturing electrons and holes. At higher temperatures, trapped charges have a higher chance of escaping and triggering an avalanche. The temperature dependence of the mean DCR of the megapixel SPAD camera before and after irradiation is shown in Fig.3.7. Afterpulsing is suppressed by taking binary frames, capturing mostly the primary dark count as the time interval between frames is significantly longer than the afterpulsing lifetime. By using the Arrhenius law with $\text{DCR} \propto \exp(-E_{act}/k_B T)$, where E_{act} is the activation energy, k_B is the Boltzmann constant, and T is temperature, the activation energy of these traps can be determined.

Fig.3.8a and Fig.3.8b show the E_{act} of the pixels before and after 100 MeV and 10 MeV proton irradiation. Before irradiation, two groups of pixels, A and B, with E_{act} of approximately 1.1 eV and 0.8 eV, respectively, can be identified. These groups correspond to the two groups of SPADs shown in Fig.3.4, where the two knees are presented. This correlation between trap energy and DCR level demonstrates that, before irradiation, the DCR of the pixels is determined by the type of existing defects from the fabrication process.

After irradiation, the median E_{act} decreases from the silicon bandgap of 1.1 eV to the half bandgap, indicating the emergence of deep-level traps due to radiation damage. This also explains why the knees in Fig.3.4 are less distinguishable at higher cumulative doses. We can observe several distinct activation energies such as 0.16 eV, 0.38 eV, 0.44 eV, and 0.55 eV, which correspond to the energy levels of oxygen-vacancy complex, divacancy, phosphorus-vacancy, and mid-bandgap. These energy levels are also observed in spectroscopy studies of CMOS image sensors and SPADs, as well as in photoconductivity measurements of electron-

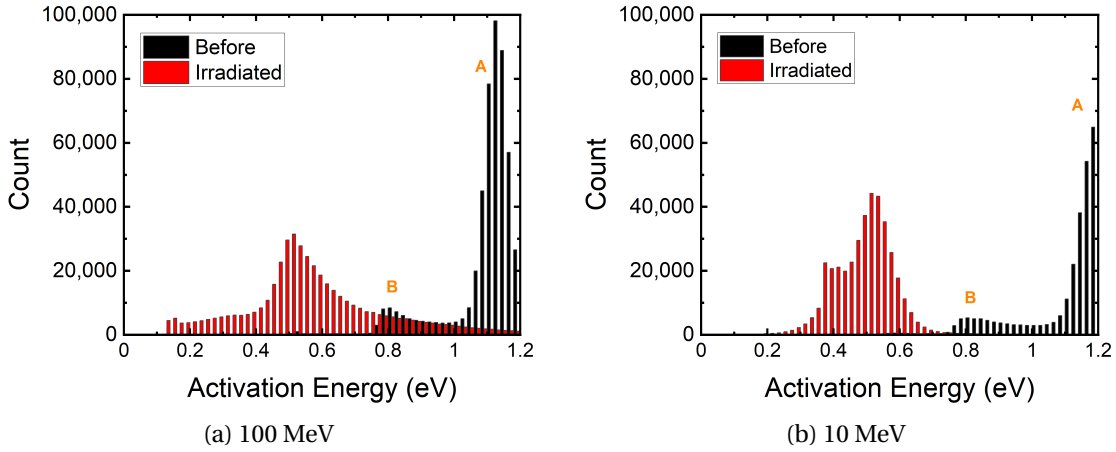


Figure 3.8: The distribution of activation energy in the megapixel SPAD camera is shown before and after exposure to 100 MeV and 10 MeV proton irradiation, which explains how trap energy can impact the DCR levels. Groups A and B correspond to the pixel groups in Fig.3.4.

irradiated silicon [74]–[78]. The spread in activation energies is attributed to trap-assisted tunneling and the Poole-Frenkel effect, which reduces the energy required for carrier transport [77]–[80]. The observed activation energies may vary from the electric field strength where the defect is created spatially. The two DUTs exhibit a similar median activation energy of 0.5 eV, indicating that the DCR levels are more affected by the densities of the defects generated post-irradiation.

Afterpulsing probability

We observed a significant increase in DCR, by orders of magnitude, in several 55 nm SPAD pairs when the DUT was exposed to 10 MeV protons, compared to its counterpart exposed to 100 MeV protons. This contradicts the defect counts obtained from our simulations. Our observation reveals that the dark count statistics in these SPADs are primarily dominated by strong afterpulsing.

Afterpulses can occur when trapped charge carriers from previous avalanches are released, possibly igniting another avalanche and contributing to overall DCR. To measure afterpulsing, SPADs are placed in a dark environment, and the inter-arrival time of noise pulses is measured. In the absence of afterpulses, the inter-arrival time histogram should follow a single exponential decay for a Poisson process, with any contribution above the exponential fit defined as afterpulsing [81]. The afterpulsing probability (APP) is defined as the number of pulses above the exponential fit divided by the total number of pulses, as shown in Equation 3.1.

$$APP = \frac{\text{afterpulses}}{\text{primary dark count} + \text{afterpulses}} = \frac{\text{afterpulses}}{\text{dark counts}} \times 100\%. \quad (3.1)$$

Fig.3.9a displays a SPAD that exhibits minimal afterpulsing prior to radiation, as most of the DUTs demonstrated APP < 1% before radiation damage. Fig.3.9b shows the same SPAD undergoing afterpulsing characterization with various excess bias voltages after radiation damage.

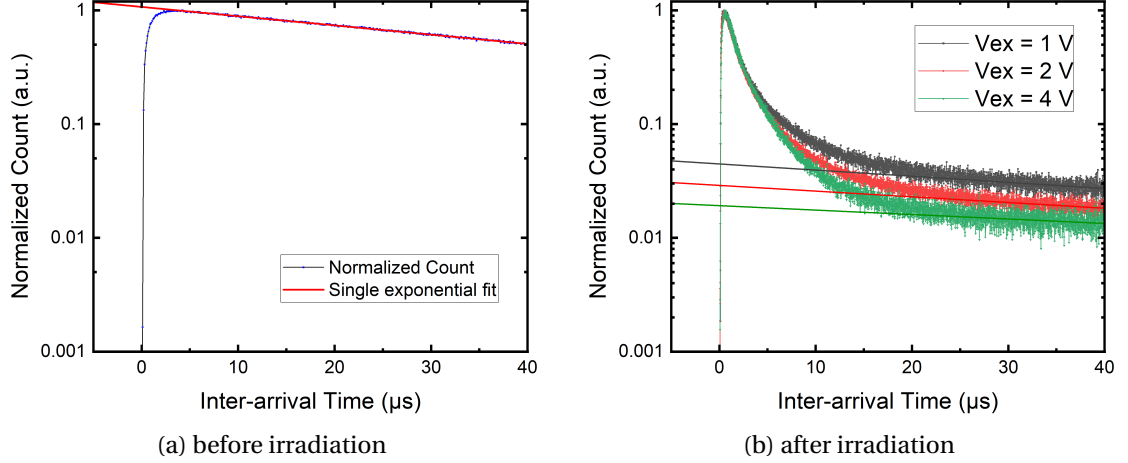


Figure 3.9: Measurement of afterpulsing on a 55 nm SPAD with an active area radius of 2.43 μm showed no pulses above the Poisson single exponential fit, indicating the absence of afterpulsing before radiation. After radiation, the probability of afterpulsing increased with higher V_{ex} , and the single exponential fit is shown by the straight line.

The increase in afterpulsing is significant and becomes dominant in DCR as excess bias increases. This is clearly illustrated in Fig.3.10a, where thirteen SPADs exhibit similar behavior. A 50% afterpulsing probability in a SPAD means that every signal pulse or primary dark count will be followed by an afterpulse. For imagers operating at low frame rates, this may not be a problem since only the first pulse or the pulse originating from the true signal is registered in each binary frame. This is also why DCR is proportional to the defect count for the 180 nm megapixel camera. However, afterpulsing can be problematic for telecommunication applications such as QKD, where it can result in a loss of efficiency in the setup[82], [83]. Additionally, afterpulsing can introduce correlations between pulses in quantum random number generators[84], making it a significant issue.

Fig.3.10a also shows that SPADs irradiated with 10 MeV protons generally exhibit a higher afterpulsing probability compared to those irradiated with 100 MeV protons, potentially due to the presence of more defects within the depletion region as previously discussed. According to [85], the time-dependent afterpulsing count can be modeled as follows:

$$P_{ap}(t) = \sum_{i=1}^N A_i \frac{1}{\tau_i} \cdot e^{-t/\tau_i}, \quad (3.2)$$

where N is the total number of deep-level traps, A_i is an exponential prefactor constant, and

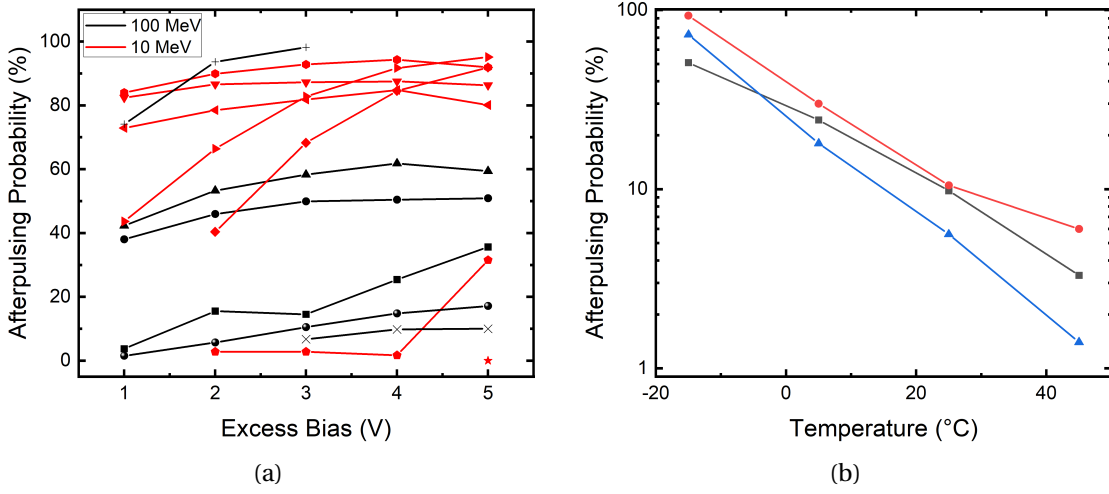


Figure 3.10: (a) displays the APP of thirteen measured SPADs at varying V_{ex} values, indicating a higher afterpulsing probability with higher V_{ex} . SPADs irradiated with 10 MeV proton exhibit more severe afterpulsing (highlighted in red). (b) shows the APP of three measured SPADs (in different colors) irradiated with 100 MeV proton at $V_{ex} = 3$ V, indicating an exponential increase in APP with decreasing temperature.

τ_i is the lifetime of the i -th trap.

We investigated the temperature dependence of the trap lifetime and its relation to APP. To this end, we tested the APP of three SPADs at different temperatures, with the voltage adjusted at each temperature to operate the SPAD at an excess voltage of 3 V. The results are shown in Fig.3.10b. It can be observed that the APP exhibits an exponential increase as the temperature decreases, which is consistent with the simulation results reported in [78]. This is because a longer trap lifetime τ at lower temperatures increases the probability of triggering an avalanche during the recharge phase of a SPAD, while at higher temperatures, the trapped carriers may be released before the SPAD recharges.

We can observe in Fig.3.9b that afterpulses add a multi-exponential component to the single exponential Poisson statistic with a trap lifetime of up to tens of microseconds. This finding supports not only the time-dependent afterpulsing model in Equation 3.2, but also the previously mentioned cumulative DCR distribution of the 180 nm SPAD camera, which showed different trap energy levels. These results suggest that multiple defects with different trap energy levels are created during irradiation.

In most of the existing literature, the increase in DCR is commonly modeled as a linear function of cumulative dose. However, we have found this approach to be inaccurate. To model the DCR more accurately, we must consider not only the cumulative dose but also the APP after radiation. Using Equation 3.1, we can express the primary dark count and afterpulse count in terms of DCR and afterpulsing rate. Therefore, we obtain the following:

$$1 - APP = \frac{\text{Primary DCR [cps]}}{\text{DCR [cps]}}. \quad (3.3)$$

We can then write the DCR under radiation as follows:

$$DCR(DDD, APP) = DCR_0 + \frac{DCR_0 + (K_d \times V_{dep} \times DDD)}{1 - APP} = \frac{\text{Primary DCR}_{rad}}{1 - APP} \quad [\text{cps}], \quad (3.4)$$

where DCR_0 (in cps) is the original DCR before radiation assuming no afterpulsing. The second term in the numerator represents the linear increase in the primary dark count or the linear increase in the leakage current of a diode due to the increase in the number of defects. The constant K_d , or the damage factor (in carriers per cm^3 per MeV/g), describes the density of damage caused by the radiation source, and V_{dep} (in cm^3) represents the depleted volume [23], [86]. This means that the primary dark count will increase linearly with the DDD. On the other hand, the denominator is a scaling factor that takes into account afterpulses triggered by primary dark counts, as described in Equation 3.3.

In Fig.3.11, we compare the linear model, commonly used in literature, with the proposed model shown in Equation 3.4. The mean K_d was obtained using the megapixel SPAD camera, with K_d values of 6.7×10^4 and 2.2×10^5 for 100 MeV and 10 MeV protons, respectively, consistent with previous findings[86]. The acquired K_d and APP were used to calculate the DCR. As shown in Fig.3.11a for five measured SPADs, the afterpulsing correction significantly improves the accuracy of the DCR values for SPADs with high DCR increase, whereas the linear model underestimates the DCR level by not considering the influence of afterpulsing.

It is challenging to determine how APP will change with cumulative dose as the afterpulsing characterization was only conducted before and after the last dose of radiation. However, if we assume that the ratio of afterpulses to primary dark counts increases linearly with cumulative dose, we can anticipate a quadratic increase in DCR. Fig.3.11b shows an example of DCR prediction based on the assumption of APP = 90% at 1 PeV/g and using the known K_d . The model that considers afterpulsing provides a more accurate prediction of DCR increase, as demonstrated in the figure.

DCR Random Telegraph Signal

In some of the damaged SPADs, we observed the occurrence of random telegraph signal (RTS) in DCR. Before irradiation, RTS was not detected in any of the DUTs. Several reports have previously mentioned RTS [87], [88], and we observed it in several DUTs in our study. An example of two 55 nm SPADs displaying RTS behavior is depicted in Fig.3.12. As the 55 nm SPADs are passively quenched and have no integrated readout circuit, we can affirm that this

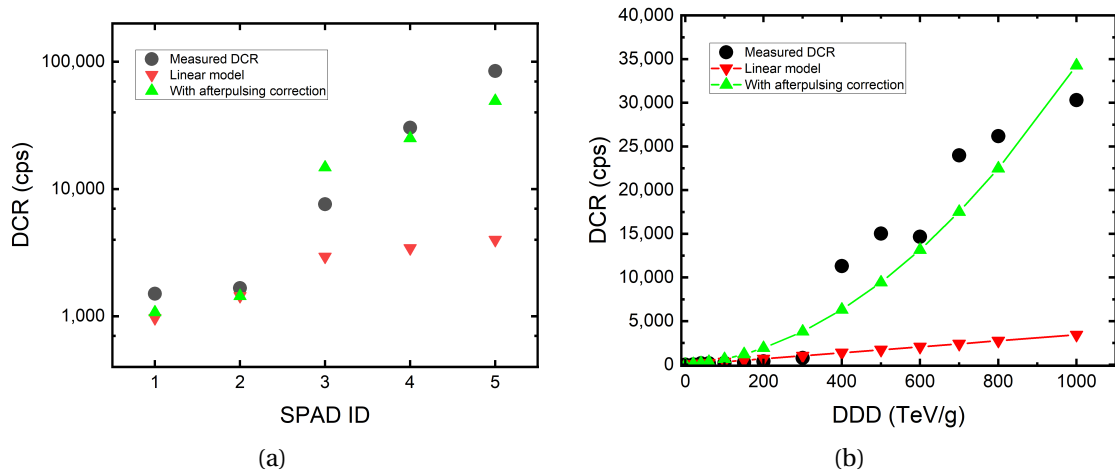


Figure 3.11: (a) shows the comparison between the linear model (red) and the proposed model (green). The proposed model provides more accurate predictions for SPADs with a high DCR increase due to afterpulsing. In (b), the proposed model predicts the DCR increases with cumulative dose under the assumption of 90% of APP at 1 PeV/g.

random telegraph noise originates from the SPADs themselves. RTS can be attributed to the presence of bi-stable or multi-stable defects within the silicon bulk, resulting in a random shift of two or more DCR levels.

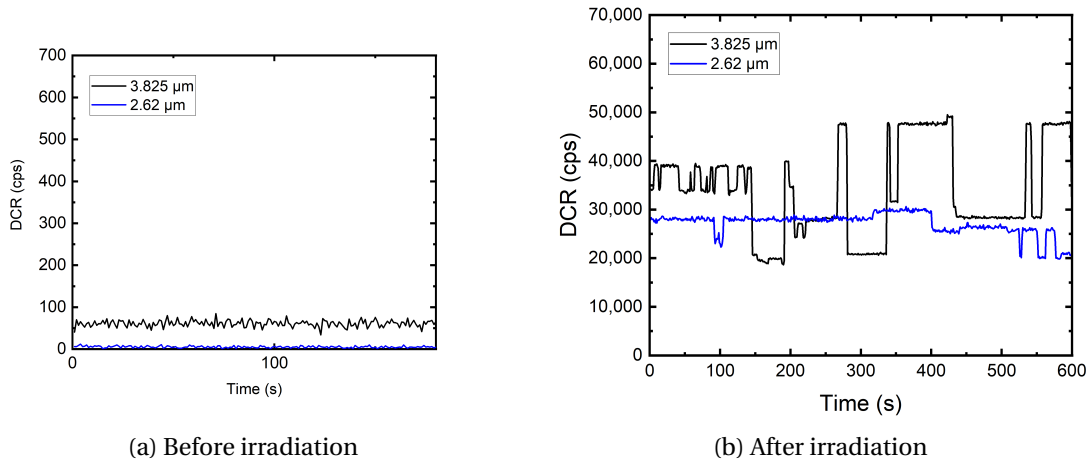


Figure 3.12: Two 55 nm SPADs, with active area radii of 3.825 and 2.62 μm, exhibiting DCR RTS at DDD of 80 TeV/g. The DCR rate in each second fluctuates randomly between several levels during a 600-second measurement.

Photodetection probability

PDP in SPADs depends on various factors such as quantum efficiency and breakdown probability, which are influenced by the SPAD’s structure and doping profile. However, in all tested DUTs, there is no observable change in the PDP, indicating that the radiation does not affect

the SPAD's structure and doping profile, as previously reported in [25]. A comparison of the PDP of the SPAD camera before and after irradiation can be seen in Fig.3.13.

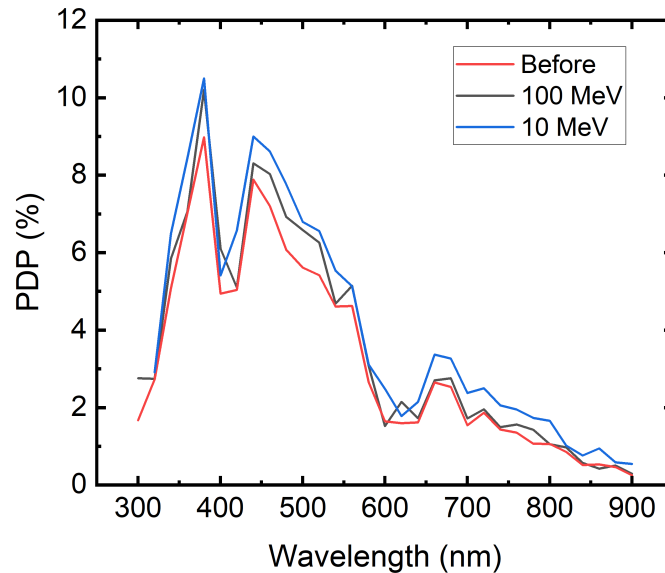


Figure 3.13: Comparison of the PDP of the megapixel camera before and after irradiation shows no observable change.

Jitter

Jitter in DPADs is influenced by the time required for a photoelectron to be multiplied in the high-field avalanche region and for a photoelectron to diffuse to the multiplication region.

To investigate whether radiation damage affects timing jitter, we utilized a 180 nm SPAD specifically designed for precise single-photon counting [68]. This SPAD was tested both before and after being exposed to 300 TeV/g DDD, and the results of the jitter measurement at 780 nm wavelength are displayed in Fig.3.14. As expected, there was no degradation in jitter observed. The error bar indicates the standard deviation among repeated measurements. The slight variation between measurements may be attributed to sample alignment with the experimental setup, causing an error at the picosecond level. These results are consistent with the prediction that a few hundred vacancies within the SPAD should not impact charge diffusion or the avalanche-triggering process.

Annealing

Annealing has been utilized to mitigate the impact of radiation damage not only in SPADs but also in photomultiplier tubes and charge-coupled devices, as reported in previous studies [28], [88], [89]. This work presents the findings of SPAD recovery through both room-temperature and high-temperature annealing.

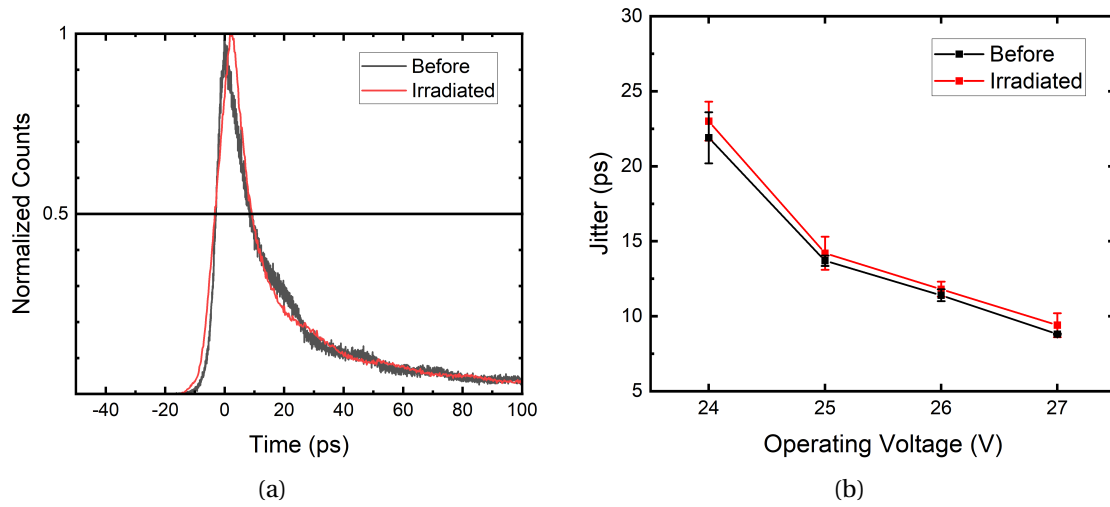


Figure 3.14: (a) The jitter measurement of a 180 nm SPAD with 8.8 μm radius at 26 V operating voltage before and after radiation. The timing jitter is defined as the FWHM of the measured histogram. (b) The comparison of jitter at different operating voltages before and after radiation. The error bar indicates the standard deviation between repeated measurements.

Research has demonstrated that ionizing damage induced by TID is reversible and can recover at room temperature [90]. In contrast, the damage caused by DDD gives rise to vacancy-interstitial defects, which necessitate high energy or high-temperature annealing for recovery [91]. The DCR of each sample was measured multiple times at room temperature after the final dose of proton radiation to monitor changes in DCR over four weeks. Following this, the samples were subjected to high-temperature annealing of up to 160 $^{\circ}\text{C}$ using a universal oven.

1. Room-temperature annealing:

As shown in Fig.3.3 and 3.6a, room-temperature annealing can occur during irradiation or during discontinuous exposure periods, similar to rapid self-annealing as discussed in [21]. After the final dose of exposure, all DUTs were kept at room temperature to observe this phenomenon. Fig.3.15 illustrates the DCR of the megapixel cameras dropping rapidly within three days after the last exposure dose, followed by a slower decrease over four weeks, similar to behavior shown in [71]. The DUT exposed to 10 MeV exhibited a larger DCR drop than the one exposed to 100 MeV, with median DCR recovery percentages of 20% and 40%, respectively. This could be due to the higher TID received by the 10 MeV sample, as recovery from displacement damage is less likely at room temperature. Additionally, the mean DCR ratio of the two DUTs on the last measured day is still similar to the defect count ratio acquired from the TRIM simulation.

The recovery trend observed in our DUTs is similar to that of metal-oxide-semiconductor devices subjected to X-ray and cobalt-60 radiation, where the threshold voltage shift recovers in a logarithmic trend over weeks [92], [93]. This suggests a transient response resulting from ionizing damage at the oxide interface. Accumulated TID can trap charges at the surface of the SPAD or at the isolation-silicon interface, where oxide is used for

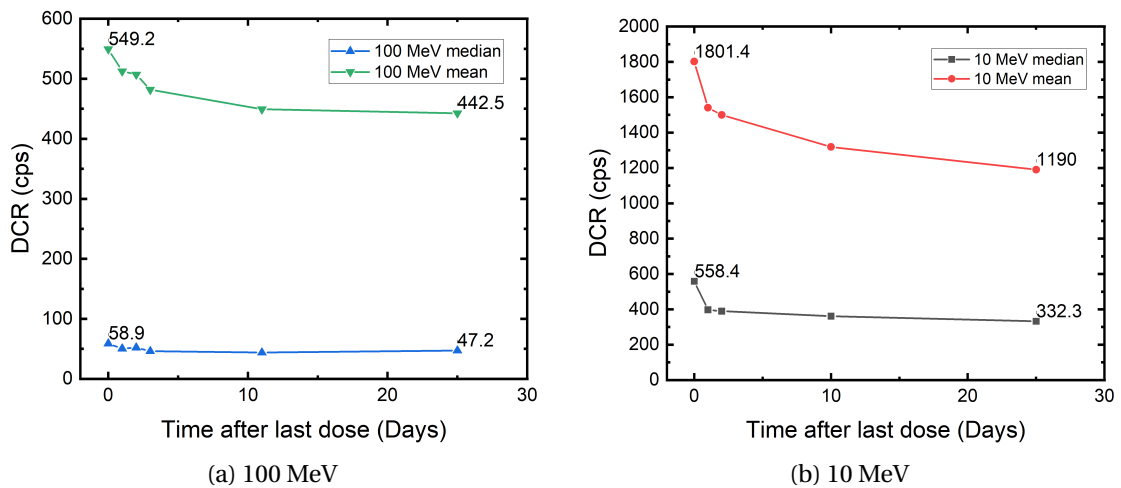


Figure 3.15: Evidence of room-temperature annealing of the 180 nm megapixel SPAD camera.

passivation or in trenches to prevent electric leakage between adjacent devices. The reduction in SPAD DCR may result from neutralizing these oxide-trapped charges.

2. High-temperature annealing:

The DUTs underwent high-temperature annealing after being annealed at room temperature. Each temperature step lasted for an hour, and the DUTs were cooled down gradually to room temperature for DCR characterization. The temperature range used was 100 °C to 160 °C in 20 °C steps.

Fig.3.16 illustrates the outcome of high-temperature annealing of the DUTs, which were exposed to 100 MeV and 10 MeV protons. The DCR drop may be caused by accelerated recovery of ionizing damage due to the higher temperature. The trend is similar to what was observed in [88], with the exception that our DUTs have not yet fully recovered. The behavior of DCR, with a more significant drop between 120 °C and 140 °C, resembles the profile of defect concentration versus annealing temperature of a phosphorus-vacancy complex [74]. Defect complexes, such as oxide-vacancy complexes, arsenic-vacancy complexes, or divacancies [74], may be responsible for the unannealed fraction in our DUTs, requiring higher temperatures for annealing.

Fig.3.17 compares the activation energy of the 180 nm megapixel SPAD camera before and after irradiation and annealing. The results show a uniform shift towards the bandgap 1.1 eV, with the mean activation energy increasing from 0.5 eV to 0.7 eV. However, there is still a noticeable cluster around 0.4 eV for both DUTs, suggesting the presence of unannealed phosphorus-vacancy complexes and divacancies.

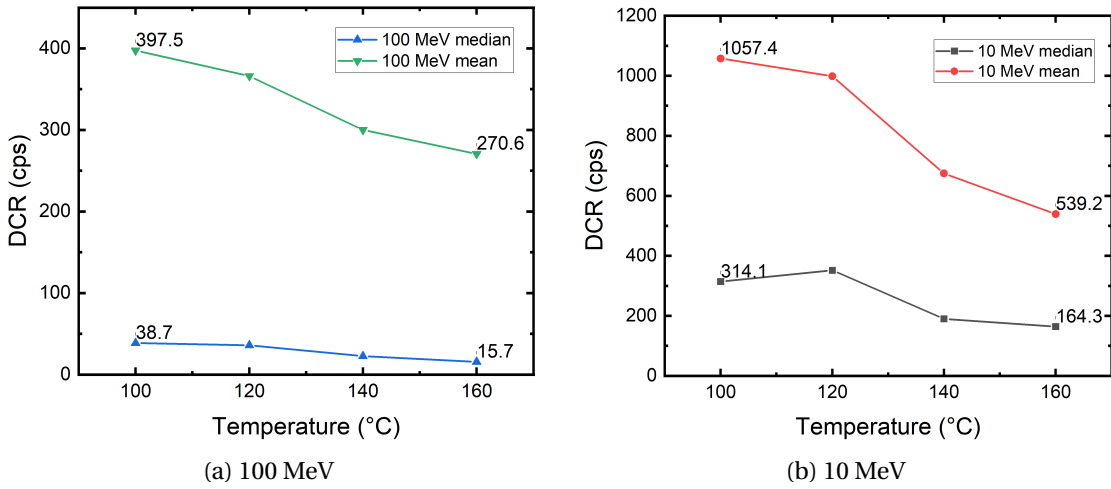


Figure 3.16: High-temperature annealing results of the 180 nm megapixel SPAD camera.

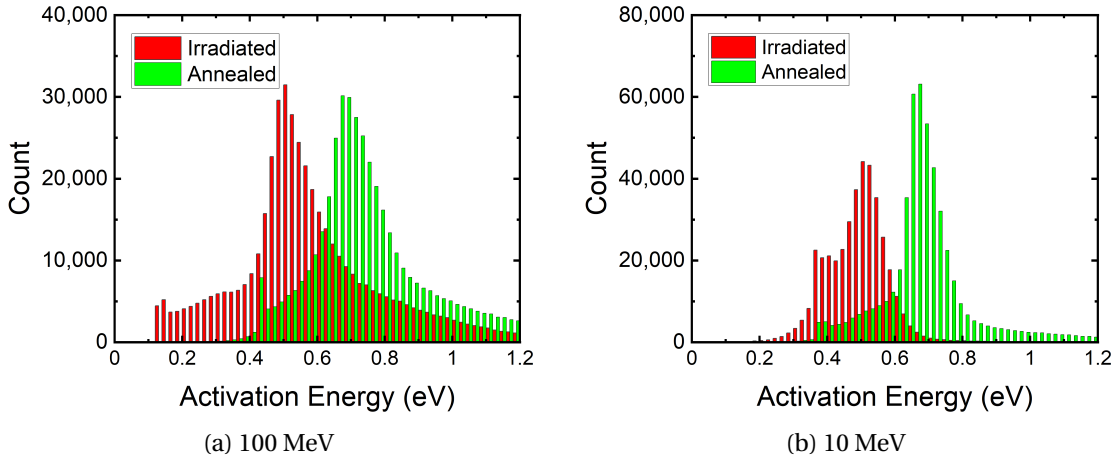


Figure 3.17: Activation energy distribution of the megapixel SPAD camera after irradiation and after high-temperature annealing.

3.2 Neutron radiation

In this section, we studied the effect of neutron irradiation, which is typically encountered in terrestrial and high-energy physics radiation environments. The aim is to provide a preliminary study for an upgrade of the RICH detector of the LHCb [57], Belle II, and ALICE 3 [58] experiments.

3.2.1 Materials and methods

The detectors are expected to maintain adequate performance throughout several years of data-taking despite accumulating radiation damage. The estimated equivalent neutron fluence by the end of the detector's life is approximately 3×10^{12} 1-MeV neutron equivalents per

square centimeter (n_{eq}/cm^2) [94]. We selected 25 μm SPADs with high precision timing [68] as the irradiation target. The DUTs were irradiated using the TRIGA Mark II nuclear reactor at Jožef Stefan Institute (JSI, Ljubljana, Slovenia), which supports a flux of approximately $4 \times 10^{12} n_{eq}/\text{cm}^2/\text{s}$ within the triangular irradiation channels at full power of 250 kW [95]. Three samples were irradiated to doses of up to 10^{10} , 10^{11} , and $10^{12} n_{eq}/\text{cm}^2$. Each sample was irradiated for 143 seconds with the reactor power set at 5.2, 50.2, and 500.2 W, respectively.

3.2.2 Results

In Fig.3.18, three samples with four SPADs each were exposed to doses of 10^{10} , 10^{11} , and $10^{12} n_{eq}/\text{cm}^2$. In Fig.3.18a, we can see that 2 SPADs maintain their original DCR level at 100 cps, which is similar to what we observed in the proton-irradiated samples, indicating no damage at such a dose. With an increasing dose, more SPADs are damaged, and the resulting DCR levels are higher. Fig.3.18c shows the DCR of four SPADs irradiated with a dose of $10^{12} n_{eq}/\text{cm}^2$. All four SPADs show DCR levels approaching the maximum count rate of the SPAD pixel, around 10 Mcps. The average DCR, despite the insufficient statistics, can be visualized in Fig.3.18d. The average shows that the DCR increases by 1 order of magnitude as the delivered neutron dose increases by 1 order of magnitude.

In some of the irradiated SPADs, we observed an increase in APP. APP varies in a wide range amongst SPADs, from negligible afterpulsing ($<0.1\%$) to 44%. With these samples, we extracted the potential reasons for this behavior. Before irradiation, the SPADs showed low APP. After irradiation, we observed afterpulsing, as shown in Fig.3.19. The sample shows an APP of 33.8%. By performing exponential fitting (red) on the tail of the counts (black), we can extract the primary dark counts as they follow a Poisson process. The counts that are on top of the exponential fit are identified as afterpulses (blue). We can see that the afterpulse is also an exponential function. In many cases, as in the proton irradiated samples, the afterpulses can be a multi-exponential function as different traps can have different lifetimes for carrier release. In this particular case, we performed a single-exponential fit on the afterpulses and extracted the afterpulse trap lifetime, which was found to be 55 ns.

In Table 3.2, we show the DCR and APP values for all 12 SPADs after annealing. We found the trap lifetime to be in the range of tens to hundreds of nanoseconds. We can observe that there is no direct relationship between the final DCR and APP. A SPAD with a higher DCR may have a lower APP, and vice versa. In this type of interarrival-time measurement, a SPAD with a high primary DCR may mask its afterpulsing. That is, a primary dark count can trigger an avalanche at the same time a trapped carrier from the last avalanche is released.

We studied the temperature-dependent DCR of these SPADs. The results can be found in Fig.3.20, which shows that the DCR halves roughly every 10°C of temperature decrease. This demonstrates the potential of using a cooling system to lower the overall DCR when SPADs are used in a high-energy physics experiment.

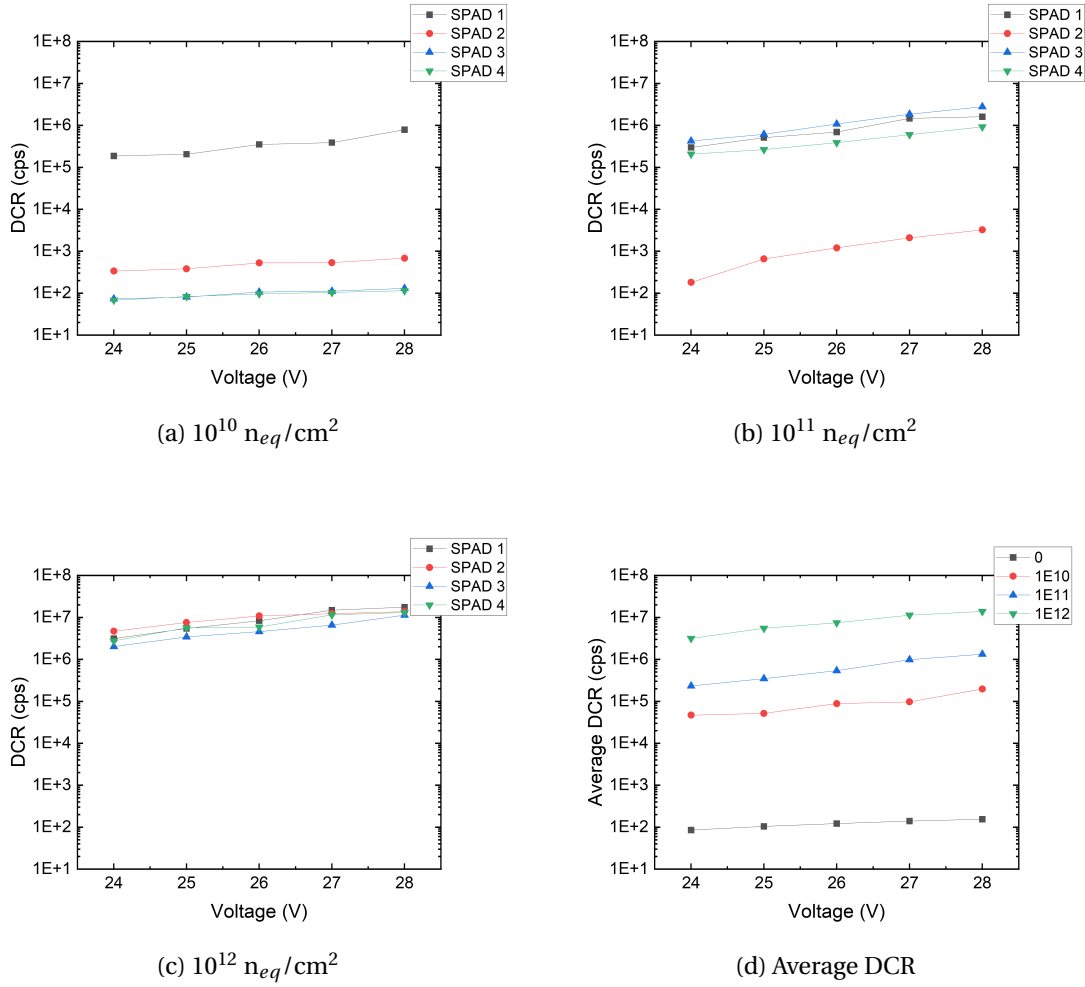


Figure 3.18: The DCR level of three samples with four SPADs each irradiated to doses of 10^{10} , 10^{11} , and 10^{12} neq/cm^2 .

3.3 Discussions

The characterization of traps in semiconductors has been a challenging task since the inception of semiconductor devices. The purpose of this is to evaluate the quality of the devices. To identify the properties of the traps, it is necessary to determine their concentration, energy levels, and carrier capture rates. For irradiated semiconductors, the formation of defects such as A-center (oxygen-vacancy complex) and E-center (group-V impurity-vacancy complex) has been observed. Various techniques have been used to study these defects, including electron spin resonance or paramagnetic resonance (EPR) spectroscopy [96], [97]. This technique uses the interaction of unpaired electrons with a strong magnetic field to identify the energy levels of the defects. It has been shown that the EPR signal arises from the neutral charge state of the defect, which is a lattice vacancy trapped next to a substitutional phosphorus atom [74], [98].

For optical detectors or p-n junction devices, it has been demonstrated that irradiation-

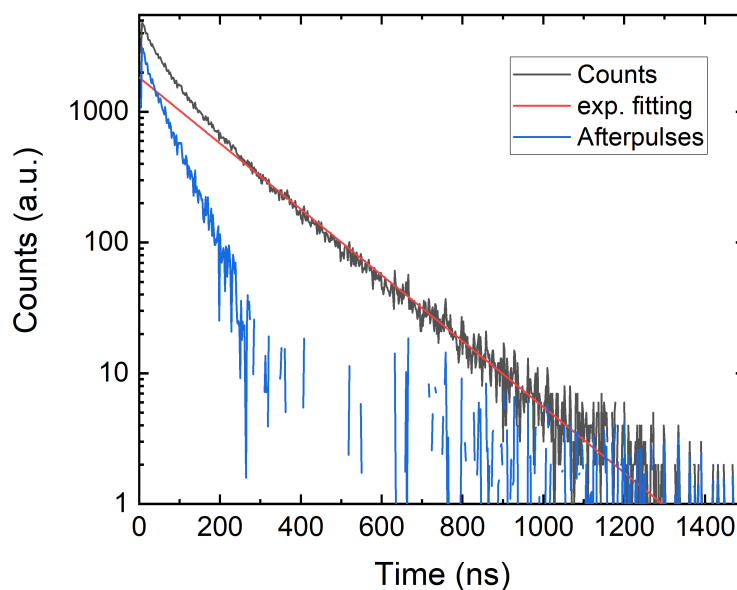


Figure 3.19: An afterpulsing measurement of a 25 μm SPAD that was irradiated with 10^{12} n_{eq}/cm^2 . The black curve represents the counts, the red curve represents the exponential fit, and the blue curve represents the afterpulses. The trap lifetime was found to be 55 ns.

Dose	10^{10}				10^{11}				10^{12}			
DCR	841k	658	109	110	653k	410	704k	98.7k	15.0M	8.4M	8.8M	6.4M
APP	28.7	5.0	5.0	1.0	0	0.3	25.1	10.4	33.8	5.8	8.5	44.0

Table 3.2: Final DCR (cps) and APP (%) of 12 SPADs irradiated with different doses from 10^{10} to 10^{12} n_{eq}/cm^2 .

induced defects can lead to unwanted dark current or noise, which is also reported in this study. Characterization of defects has been performed on CMOS image sensors based on pinned photodiodes [76], [99]. In particular, [99] extracted the activation energy using the carrier generation and recombination characteristics of p-n junctions derived by C.T. Sah [100], which is an extension of the Shockley-Read-Hall (SRH) recombination or trap-assisted recombination [101], [102]. In these studies, the diode devices operate at a low reverse bias below the breakdown voltage. The generation rate of electrons in dark conditions can be quantified by the leakage or dark current. The activation energy of the defects can then be extracted using the Arrhenius equation, which relates the dark current and the operating temperature in an exponential relationship. This is known as dark current spectroscopy.

According to Boltzmann statistics that govern multistage reaction processes, the reaction rate limiting step is expected to occur at energies larger than half the bandgap energy ($E_g/2$). However, in many studies of photodiodes and SPADs, E_{act} smaller than $E_g/2$ have been

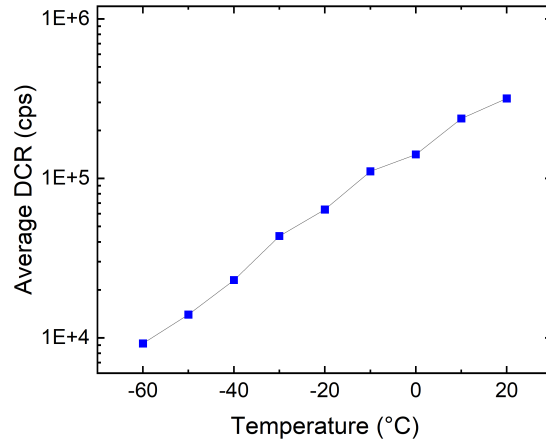


Figure 3.20: Temperature-dependent DCR of the sample irradiated with $10^{11} \text{ n}_{eq}/\text{cm}^2$.

observed [77]. This phenomenon is often attributed to the presence of tunneling or electric field-enhanced emissions [76], [103].

For SPAD operation, noise appears in the form of dark counts. Unlike dark current in conventional photodiodes and linear-mode avalanche photodiodes, where the noise comes in the form of continuous current in a non-equilibrium steady state, when a dark count occurs in a SPAD, the number of carriers changes dramatically. An electron that triggers the avalanche breaks the steady state, and carriers continue to increase until the device is quenched and recharged. While the number of charge carriers changes within the space charge region, the Fermi level shifts resulting in a dynamic behavior [76], [104]. Afterpulsing is a behavior that is unique to SPADs. It occurs when charge carriers become trapped in energy states within the bandgap, resulting in extra dark counts. Taking afterpulsing into account, the charges that trigger an avalanche do not necessarily originate from the valence band within the space charge region. This behavior can potentially affect the extraction of activation energies.

The behavior of carriers releasing from energy states within the bandgap resembles that of defects in semiconductors. In fact, defects in semiconductors are identified using deep-level transient spectroscopy (DLTS), which was introduced by D.V. Lang [105], [106]. In DLTS, a p-n junction is prepared in a quiescent reverse-biased state, as shown in Fig.3.21. In this state, with a reverse bias V_b , the carriers within the depletion region are swept out by the electric field. As the trap energy level (E_T) is raised above the quasi-Fermi level, the carriers are less likely to be trapped in E_T . A pulse of charge is then injected into the depletion region of a p-n junction with forward bias. With sufficient time for minority carrier injection, in this case, electrons, the traps are filled with trapped electrons. The junction is then brought back to reverse bias conditions. As E_T is lifted above the Fermi level, the electrons can thermally escape from the traps to the conduction band, creating a capacitance transient [107] or a voltage transient [108], [109].

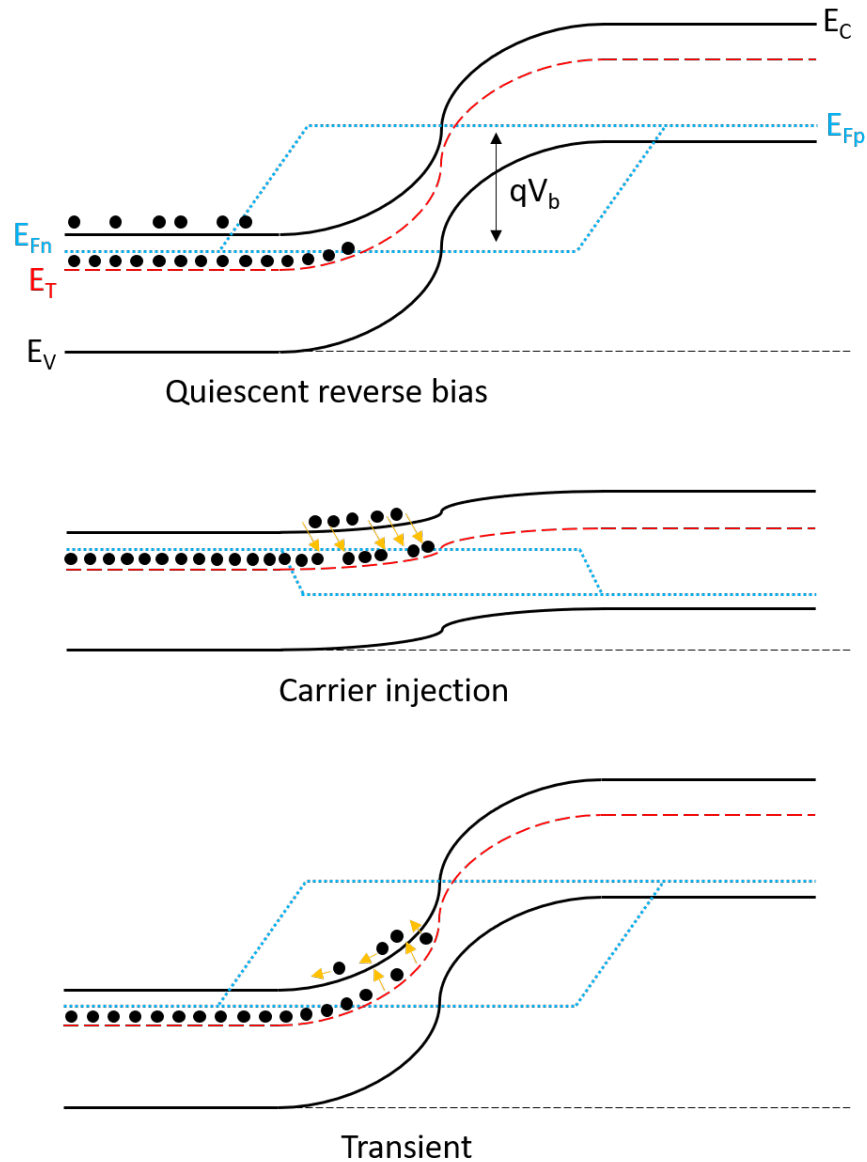


Figure 3.21: The working principle of deep level transient spectroscopy.

To characterize the trap with the transient response, we need to find a link between the emission probability and time. This can again be done with the help of the SRH recombination process. We need to consider two processes, R_{C-T} and R_{T-C} , which represent the rate with which electron density transits from the conduction band to the trap level and the rate with which electron density transits from the trap to the conduction band, respectively. We can write R_{C-T} [$1/\text{cm}^3 \cdot \text{s}$] as follows:

$$R_{C-T} = r \cdot n_e \cdot n_T^0, \quad (3.5)$$

where r is the rate of the volume that is probed by the electron and can be represented by the thermal velocity of the electron v_{th} [cm/s] and the capture cross-section of the trap level for conduction-band electrons σ_e [cm²], with the relation of $r = v_{th} \cdot \sigma_e$. The second term, n_e [1/cm³], is the electron density. n_T^0 is the density of trap levels with no electron in it, which can be described by the total density of deep-level states N_T and the Fermi-Dirac statistic with $n_T^0 = N_T \cdot [1 - f(E_T, T)]$. We can then write R_{C-T} as:

$$R_{C-T} = v_{th} \cdot \sigma_e \cdot n_e \cdot N_T \cdot [1 - f(E_T, T)]. \quad (3.6)$$

By the same principle, we can derive the rate at which electrons transition from the trap level to the conduction band, denoted by R_{T-C} . This rate can be expressed as:

$$R_{T-C} = r' \cdot (N_C - n_e) \cdot n_T^-. \quad (3.7)$$

Here, $(N_C - n_e)$ gives the density of unoccupied states in the conduction band, which is typically much larger than the electron density n_e . n_T^- is the density of negatively charged traps with one electron in each trap and can be written as $N_T \cdot f(E_T, T)$. Combining these expressions, we can write R_{T-C} as:

$$R_{T-C} = r' \cdot N_C \cdot N_T \cdot f(E_T, T). \quad (3.8)$$

Here, r' represents the rate of the volume that is probed by the electron for the emission process. We can define the emission rate e_n [1/s] as $r' \cdot N_C$. In local equilibrium, we can assume the rate of electrons going from the conduction band to the traps and the rate of electrons going from the traps to the conduction band are the same ($R_{C-T} = R_{T-C}$). With equation 3.6 and equation 3.8, we can find:

$$e_n = \frac{v_{th} \cdot \sigma_e \cdot n_e \cdot [1 - f(E_T, T)]}{f(E_T, T)}. \quad (3.9)$$

Depending on the Fermi level E_F , we get $n_e = N_C e^{-(E_C - E_F)/k_b T}$ and $f(E_T, T) = 1/(e^{(E_T - E_F)/k_b T} + 1)$. We can then find the electron emission rate as:

$$e_n = v_{th} \cdot \sigma_e \cdot N_C \cdot \exp\left(-\frac{E_C - E_T}{k_b T}\right). \quad (3.10)$$

With the same method, we can derive the hole emission rate e_h . We can see that if the trap energy level is closer to the conduction band, the trap has a higher emission rate. This is also why electron traps lie mostly above the mid-bandgap, closer to E_C .

The observable, i.e. the capacitance or the voltage across the junction, is linearly proportional to the number of charges changing in the traps, in other words, the density of filled traps n_T^- .

With the ratio of e_h and e_n , we can represent n_T^- as the following:

$$n_T^- = \frac{e_h}{e_h + e_n} N_T, \quad (3.11)$$

where N_T is the total density of trap states. We can also write the variation of n_T^- with respect to time as:

$$\frac{dn_T^-}{dt} = -e_n \cdot n_T^- + e_h \cdot (N_T - n_T^-), \quad (3.12)$$

which considers both the emission of filled traps and the emission of holes from empty traps. The solution to this differential equation 3.12 is:

$$n_T^-(t) = \frac{e_h}{e_h + e_n} N_T + \frac{e_n}{e_h + e_n} N_T \cdot \exp\left(\frac{-t}{1/(e_h + e_n)}\right). \quad (3.13)$$

We can now determine the time constant $\tau = 1/(e_h + e_n)$, which characterizes how the number of carriers changes in the traps and thus how the observable changes over time. For simplicity, let's consider an n^+p junction, in which most of the depletion region lies in the p region. For an electron trap, by definition, $e_h \ll e_n$, meaning that the trap is most of the time empty and ready to trap an electron. The time constant τ can then be approximated as $1/e_n$, where e_n is given by equation 3.10.

With the measurement result, we can thus find that the emission rate follows the Arrhenius relation. The plot of the natural log of the emission rate $\ln(e_n)$ versus the reciprocal of $k_b T$ will give us a negative slope, which is the activation energy $E_{act} = E_C - E_T$.

Now, we can draw an analogy between DLTS and SPAD operation. When a SPAD fires, a large number of carriers flow into the depletion region. Similarly to applying a forward bias, the carriers traveling through the depletion region can become trapped. When the SPAD is recharged with a reverse bias, the energy levels of the traps are lifted above the Fermi level, thus allowing carrier emission and causing another avalanche. A similar idea has been proposed for avalanche photodiodes [110]. In the case of irradiated SPADs, we observe strong afterpulsing, which indicates that the DCR is dominated by carriers that are released from the trap levels.

As both v_{th} and N_C are temperature dependent, with $v_{th} \propto T^{0.5}$ and $N_C \propto T^{1.5}$, researchers have plotted $\ln(e_n/T^2)$ versus $1/T$ in various studies [111]–[113]. The σ_e is weakly dependent on temperature but strongly dependent on energy [114]. In our study, we extracted the E_{act} values using the conventional $\ln(\text{DCR})$ vs. $1/T$ plot. As the temperature range measured was small, the resulting E_{act} values did not change much, even when fitted with $\ln(\text{DCR}/T^2)$. The afterpulsing in the DCR of SPADs and the capacitive transient in DLTS both originate from carrier emission from traps. Interestingly, this could be the reason why activation energy smaller than half bandgap can be measured from our samples.

3.4 Conclusion

We conducted a study to analyze the impact of proton and neutron radiation on SPADs. With proton, we irradiated the 55 nm BCD and 180 nm CMOS SPADs up to a displacement damage dose of 1 PeV/g. SPADs that were irradiated with lower energy protons exhibit larger and quicker increases in DCR than those exposed to higher energy protons. This behavior is consistent with measurements performed on other, older, technologies [9]. The reason for this behavior is that lower energy protons have a more effective interaction with the silicon lattice, creating a greater number of defects and more significant ionizing damage. We found that afterpulsing plays a significant role in the increased DCR. When SPADs are operating in a more favorable regime with higher V_{ex} for higher PDP and lower temperature for lower DCR, the afterpulsing effect becomes more pronounced. This issue has not been addressed in most literature on radiation damage in SPADs, but we believe it should always be taken into consideration because afterpulsing can impact applications such as quantum communication and quantum random number generation. We have introduced a new model for predicting SPAD DCR considering afterpulsing. The experimental data of SPADs with high afterpulsing probability are better fitted by the model. We hypothesize that the presence of afterpulsing and different DCR level populations in the megapixel SPAD camera can be attributed to the creation of multiple trap energy levels resulting from radiation damage. These energy levels are believed to correspond to various complexes, including divacancies, oxide-vacancy, and phosphorus-vacancy complexes formed by proton radiation. Our findings also reveal that the DCR level is influenced by different trap energy levels before irradiation, while it is more dependent on the number of defects created after irradiation. Moreover, the DCR RTS effect also shows how proton radiation can create bi-stable or multi-stable defects. We observed that the SPAD DCR showed recovery under room-temperature annealing and high-temperature annealing during irradiation. This recovery may be attributed to the transient response of ionizing damage, as the oxide-trapped charges are neutralized, and dark counts from the oxide-silicon interface are reduced. The logarithmic trend observed in the SPAD DCR recovery is similar to radiation effects on MOS devices, and further improvement is observed after high-temperature annealing. Our findings suggest that the drop in DCR could be the result of phosphorus-vacancy annealing, as the recovery trend follows the defect concentration versus the annealing temperature of the phosphorus-vacancy complex. We also investigated the effect of neutron radiation, the results agree with the finding in proton-irradiated samples.

We can see from Fig.3.22 that even after normalizing DCR to the area, larger SPADs exhibit a higher increase in DCR. Smaller SPADs are naturally more radiation-hard as their photo-collector regions are less likely to be damaged due to the probabilistic nature of radiation damage [115]. The newly found stepwise increase in DCR observed in this study supports the idea that defect creation within or near the photocollector region is necessary for DCR to increase. Therefore, for applications that require high radiation tolerance and low DCR, a smaller SPAD size is recommended, despite the potential drawback of lower PDP [9], [63]. Optical enhancements such as microlenses can be employed to improve PDP in smaller SPADs.

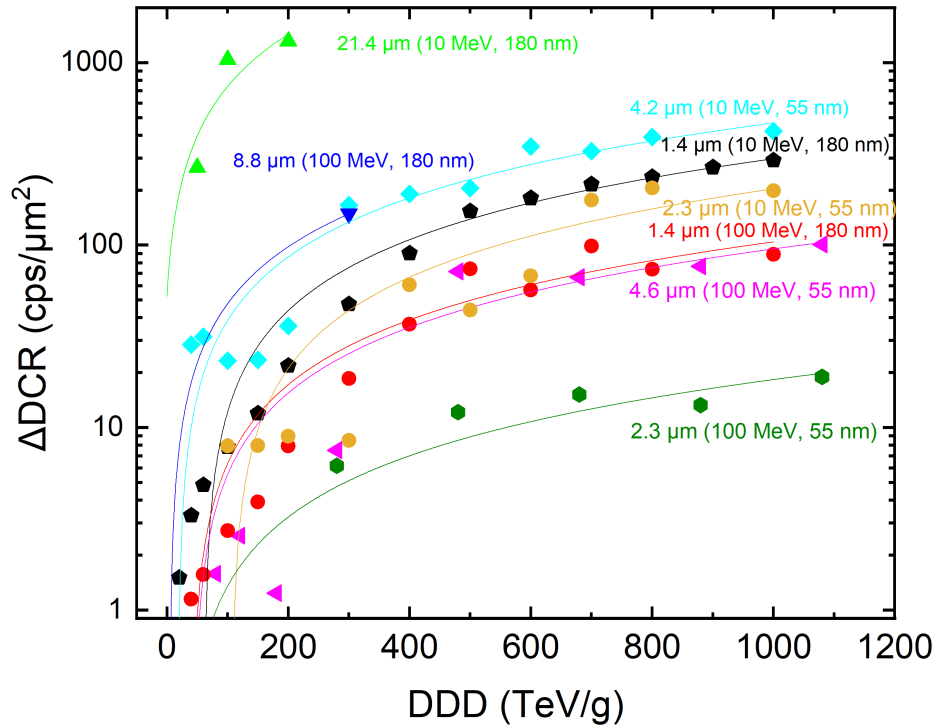


Figure 3.22: Normalized DCR of the DUTs at various DDR values with linear fitting. The trend indicates that larger SPADs undergo more degradation even after normalizing for the active area. This may be due to a higher probability of afterpulsing. Moreover, it is observed that even at the same DDR, lower energy protons cause more damage to the photocollector region.

For mitigating afterpulsing, one can implement a longer hold-off time, during which biasing is below breakdown, to reduce the trapped charges [116].

Despite the radiation damage, most samples maintained acceptable DCR levels after irradiation. As shown by previous research, radiation damage can cause dark current to increase by 2-4 orders of magnitude in photodiodes and CCDs [9], [14], [15]. However, due to their photon counting capabilities, SPADs have greater potential for diverse applications in space-based systems compared to conventional sensors. In summary, the radiation effects observed in this study demonstrate that SPADs are not only suitable for long-term space missions with much lower proton flux than our experiments (e.g., 10 protons/cm²/s at 10 MeV for a 400 km polar orbit mission [117]), but also for high energy physics studies where high radiation doses are expected.

4 Results of SPAD-based applications

The advancement of SPAD-based systems has paved the way for significant breakthroughs in various applications. In this study, we investigate the potential of SPAD-based arrays in applications including space-based imaging, ranging, and astronomy. Additionally, we leverage the single-photon sensitivity of SPADs for material characterization, specifically in the realm of fluorescence lifetime imaging. Furthermore, we leverage the precise timing capabilities of SPADs for direct radiation detection, highlighting their potential as beam trackers in high-energy particle beamlines exposed to demanding radiation environments. By conducting these investigations, we aim to shed light on the versatility and advantages of SPAD technology across diverse fields of research. The results presented in this chapter are based on [35], [49], [118] and several conference presentations.

4.1 2D high dynamic range imaging

Radiation damage has been observed to elevate the DCR of SPAD-based cameras [65]. By considering the anticipated radiation dose in various space missions, it becomes possible to estimate the rate at which the DCR increases [117]. This understanding proves valuable in assessing camera performance over its projected lifespan and devising mitigation strategies to minimize the detrimental effects of radiation damage.

The increase in DCR naturally affects image quality, making it a critical factor to consider in SPAD-based cameras. Unlike conventional CCD or CMOS cameras, which demonstrate linear response characteristics, SPAD cameras operate as a quanta image sensor (QIS) and exhibit nonlinear response behavior [119], [120]. Leveraging this nonlinear response, we can derive theoretical limits for SNR and dynamic range as a function of exposure time, noise, bit depth, and incoming light. This quantitative approach allows us to assess image quality under diverse lighting conditions.

We establish the following proposition:

Chapter 4: Results of SPAD-based applications

The signal-to-noise ratio (SNR) of a clock-based SPAD camera is defined as:

$$\text{SNR}[\text{dB}] = 20 \log_{10} \left(\frac{1}{\sqrt{F}} \cdot \frac{T_{exp} \cdot \lambda}{\sqrt{e^{\frac{T_{exp} \cdot (\lambda + \text{DCR})}{F}} - 1}} \right) = 20 \log_{10} \left(\sqrt{F} \cdot \frac{t_{exp} \cdot \lambda}{\sqrt{e^{t_{exp} \cdot (\lambda + \text{DCR})} - 1}} \right), \quad (4.1)$$

where F is the number of binary frames, which is two to the power of the bit depth. T_{exp} is the total exposure time, t_{exp} is the exposure time per frame (T_{exp}/F), and λ is the actual incoming signal rate.

Proof of Proposition:

Assuming a SPAD camera is uniformly exposed to a light source governed by Poisson statistics, with $\Pr(k) = r^k e^{-r} / k!$ and k representing the number of events experienced by one SPAD, we can calculate the probability of the SPAD firing ($\Pr(k \neq 0)$), m_1 , and registering a 1 at the measured output as:

$$m_1 = 1 - e^{-r}, \quad (4.2)$$

where r is the mean number of events. We can see that the probability of a SPAD firing follows the Bernoulli distribution with m_0 being the probability of a binary frame registering a 0 and equals to $1 - m_1$. Now, we substitute r with the total number of impinging photons and dark counts per binary frame, denoted as N' . The expression for m_1 is then rewritten as follows:

$$m_1 = 1 - e^{-N'} = 1 - e^{-\frac{T_{exp}(\lambda + \text{DCR})}{F}}. \quad (4.3)$$

If we focus on a single pixel of the camera exposed to this light source, we can expect the measured output of F frames to be:

$$M_F = F \cdot m_1 = F[1 - e^{-N'}], \quad (4.4)$$

which aligns with the well-known nonlinear relationship between detected count and incoming signal observed in quanta image sensors [119]. It can also be understood as a binomial distribution with F trials and a success rate of m_1 . To assess the impact of photon shot noise across the entire camera, we must determine the variance of M_F across all pixels. Based on binomial distribution, we can express the variance as follows:

$$\sigma_m^2 = F \cdot m_1 \cdot m_0 = F \cdot [1 - e^{-N'}] \cdot [e^{-N'}]. \quad (4.5)$$

If our goal is to achieve dynamic range extension [121] by applying the inverse function to obtain the impinging photon counts over the entire exposure time $T_{exp} \cdot \lambda$, we must write the standard deviation of the impinging photon count as:

$$\sigma_n = \frac{\sigma_m}{\partial M_F / \partial (T_{exp} \cdot \lambda)} = \frac{\sqrt{F} \cdot \sqrt{1 - e^{-N'}} \cdot \sqrt{e^{-N'}}}{e^{-N'}} = \sqrt{F} \sqrt{e^{N'} - 1}. \quad (4.6)$$

We can then find the SNR as:

$$\text{SNR} = \frac{T_{exp} \cdot \lambda}{\sigma_n} = \frac{1}{\sqrt{F}} \frac{T_{exp} \cdot \lambda}{\sqrt{e^{N'} - 1}}. \quad (4.7)$$

The proposition is supported by both the experimental results performed with the 180 nm CMOS megapixel SPAD camera detailed in [35] and a Monte Carlo simulation that considers a 1% photo response non-uniformity. The nonlinear measured photon count (M_F) is visualized in Fig.4.1a, where a 12-bit image is formed with a total exposure time of T_{exp} of 1 second and F of 4096. The resulting SNR as a function of dark count and incident photon count is shown in Fig.4.1b. It can be observed from the figure that the SNR of a low-noise SPAD camera operating in low-light regions is limited by shot noise, as:

$$\lim_{T_{exp} \cdot \lambda \rightarrow 0} \frac{1}{\sqrt{F}} \cdot \frac{\sqrt{T_{exp} \cdot \lambda}}{\sqrt{e^{\frac{T_{exp} \cdot \lambda}{F}} - 1}} = 1. \quad (4.8)$$

Furthermore, it is evident that the SNR significantly degrades under low-light conditions as the DCR increases.

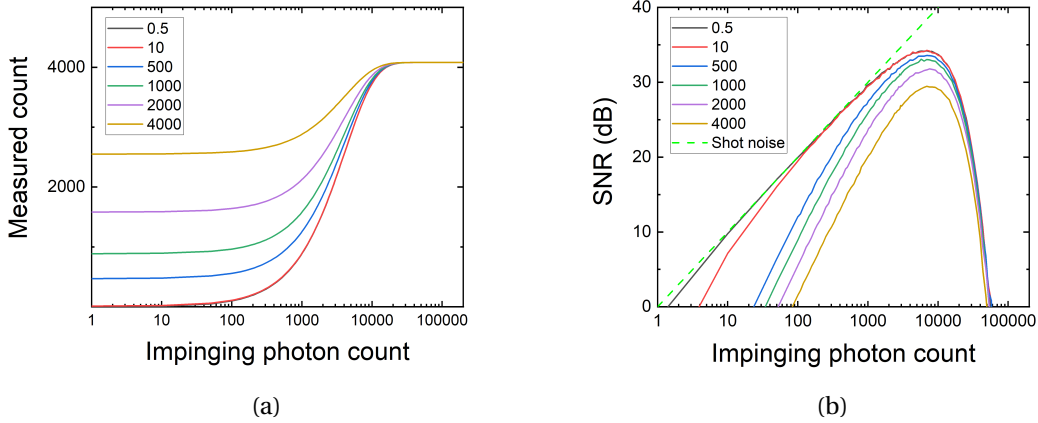


Figure 4.1: In the case of a 12-bit image captured by a SPAD camera with a total exposure time of 1 second, (a) depicts the measured photon count (M_F) of the 12-bit image under various incident photon counts and dark count levels. Dark count levels of 0.5 and 10 are superimposed. (b) illustrates the SNR of the resulting image.

The dip in SNR at higher illumination levels can be attributed to the implementation of standard deviation correction described in Equation 4.6. At elevated signal strengths, as evident from Fig.4.1a, the camera's measured count output becomes saturated. When all pixels are at their maximum count, this leads to a diminished standard deviation below the shot noise limit. Consequently, the standard deviation, σ_m , loses its mathematical significance, as illustrated in Fig.4.2a. To achieve dynamic range extension through linearizing the measured count to the impinging photon count, it is necessary to apply the correct standard deviation

Chapter 4: Results of SPAD-based applications

using Equation 4.6. This involves dividing the standard deviation by the first derivative of the measured count with respect to the impinging photo count. The resulting corrected standard deviation, σ_n , is depicted in Fig.4.2b.

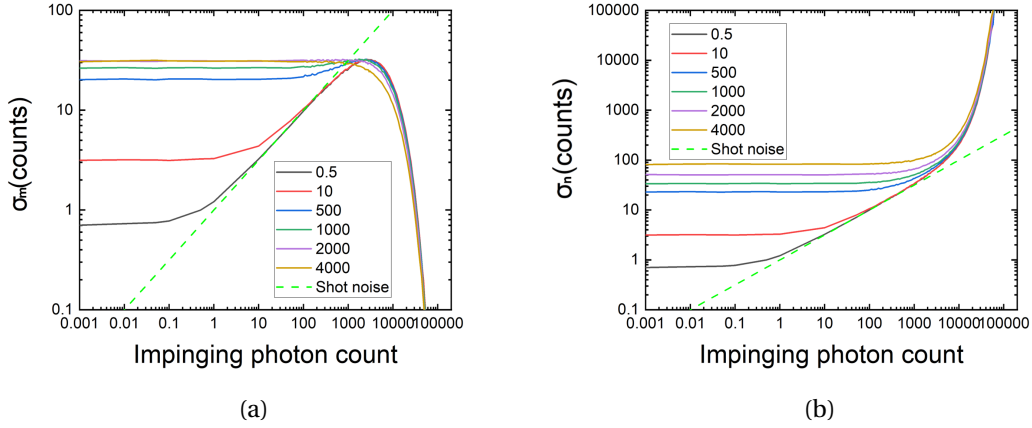


Figure 4.2: In the case of a 12-bit image captured by a SPAD camera with a total exposure time of 1 second, (a) shows the standard deviation of the output measured count, σ_m ; (b) shows the corrected standard deviation considering dynamic range extension, σ_n .

The proposition presented is in agreement with the findings proposed in [121], assuming that the DCR is not considered in a clock-driven SPAD system. Without accounting for the impact of DCR, the maximum SNR is solely dependent on the frame rate F . This emphasizes the significance of the bit depth in a SPAD-based imaging system. Additionally, it demonstrates that the SNR is directly proportional to the square root of the frame rate, or equivalently, the inverse of the dead time of a binary frame. By increasing the frame rate of a SPAD camera, which enables more temporal oversampling [64], we can enhance the SNR towards the shot noise limit, as:

$$\lim_{F \rightarrow \infty} \frac{1}{\sqrt{F}} \cdot \frac{T_{exp} \cdot \lambda}{\sqrt{e^{\frac{T_{exp} \cdot \lambda}{F}} - 1}} = \sqrt{T_{exp} \cdot \lambda}. \quad (4.9)$$

We can visualize the affect of both DCR and frame rate on the SNR at different illumination condition in Fig.4.3.

The dynamic range, which determines the range of brightness levels that can be captured in a single image, is another crucial metric for assessing image quality. We can determine the dynamic range of the SPAD camera by considering the working condition where the SNR exceeds unity [119], or SNR = 0 dB. This condition allows us to extract the camera's dynamic range based on the proposition.

As the DCR increases, the SNR deviates from the shot noise limit, particularly in low light conditions. This deviation not only impacts the image quality of low light regions but also

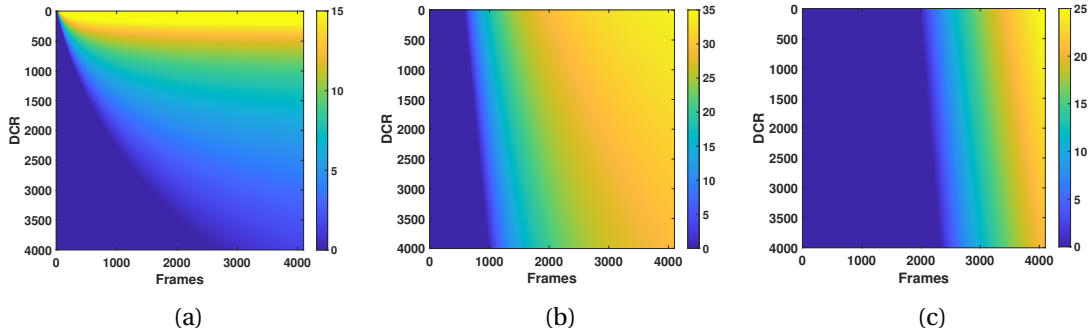


Figure 4.3: The SNR of a SPAD camera with DCR at different illumination condition ($T_{exp} \cdot \lambda =$) (a) 100, (b) 6530, and (c) 25000.

affects the dynamic range. Fig.4.4a demonstrates the dynamic range degradation of 8-bit, 10-bit, and 12-bit images as the DCR increases. Even a small increase in DCR leads to a rapid degradation of the dynamic range, especially for images with lower bit depths.

As mentioned earlier, the frame rate plays a crucial role in improving the maximum SNR and, consequently, the dynamic range. Fig.4.4b displays the dynamic range of images with different bit depths. It is evident that a SPAD camera with no noise can achieve a dynamic range of over 100 dB with a bit depth of 13. However, as the DCR increases, a higher frame rate becomes necessary to maintain a reasonable dynamic range.

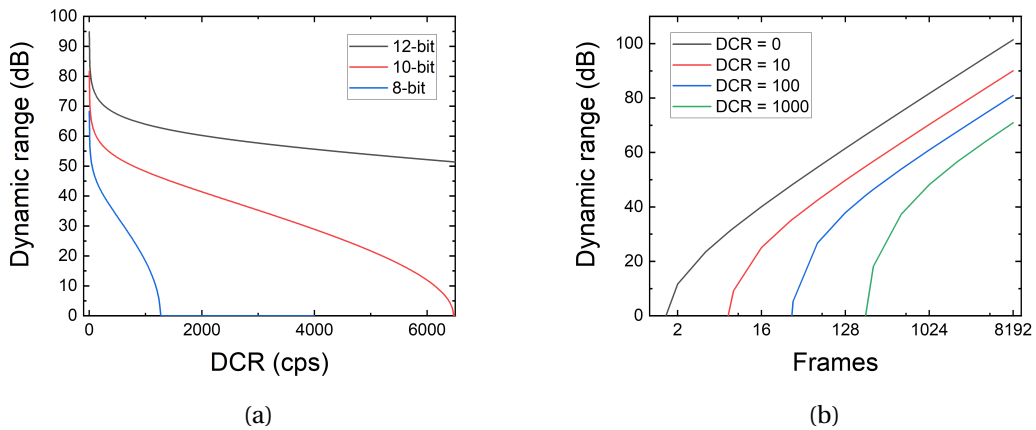


Figure 4.4: (a) depicts the degradation of dynamic range in 12-bit, 10-bit, and 8-bit images captured by a SPAD camera with a total exposure time of 1 second, as the DCR increases. (b) illustrates the improvement of dynamic range with an increasing bit depth at different DCR levels.

To further improve the dynamic range of the system, one can integrate images using a mixed exposure technique. This is similar to what is known as exposure bracketing in conventional cameras. The exposure timing sequence is illustrated in Fig.4.5, where both mono-exposure

and dual-exposure modes are depicted. In the mono-exposure mode, the exposure time, τ_m , for each binary frame is kept identical. In the dual-exposure mode, the image is composed of alternating long and short exposure times, τ_L and τ_s , respectively. To maintain the same total exposure time over F frames, the sum of τ_L and τ_s should equal to $2\tau_m$.

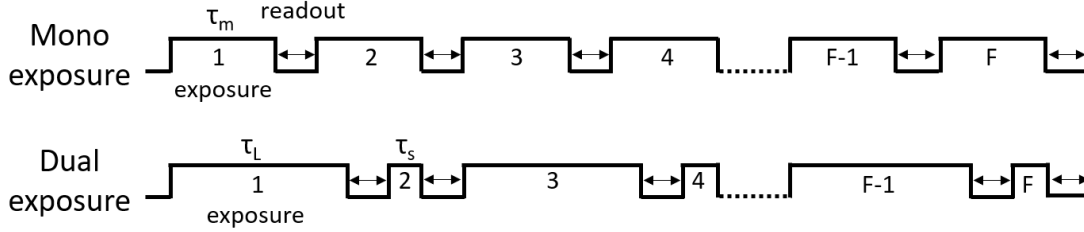


Figure 4.5: Exposure timing of the mono- and dual-exposure mode.

Assuming the DCR is significantly lower compared to the impinging photon rate, we can derive the estimated measured count of the mono-exposure mode using Equation 4.4 as follows:

$$M_{mono} = F[1 - e^{-N}] = F[1 - e^{-\frac{\tau_{exp}\lambda}{F}}], \quad (4.10)$$

where N is the number of impinging photons per binary frame. The estimated measured count in the dual-exposure mode is a combination of two mono-exposure images with different exposure times. We can then estimate the measured count as follows:

$$M_{dual} = \frac{F}{2}[1 - e^{-2N \cdot \frac{\tau_L}{\tau_L + \tau_s}}] + \frac{F}{2}[1 - e^{-2N \cdot \frac{\tau_s}{\tau_L + \tau_s}}]. \quad (4.11)$$

Using Monte Carlo simulation, we can observe the measured photon count for both the mono-exposure mode and dual-exposure mode with ratios of 1:2, 1:4, and 1:8, as depicted in Fig.4.6a. This simulation was validated through measurements using a uniformly illuminated white scene. The measurement results are superimposed onto the same figure, demonstrating the accuracy of both the simulation and the equation in predicting the measured count of the SPAD camera. The SNR values for both the mono-exposure and dual-exposure modes are depicted in Fig.4.6b. Once more, the comparison demonstrates that the proposition accurately characterizes the SNR of an image under specific illumination conditions.

Finally, we demonstrate high dynamic range imaging with a real-life scene in Fig.4.7. Both images were captured using the same exposure time. It can be observed that in the mono-exposure image, the mountains and the lamp appear overexposed, leading to a loss of details. In contrast, the dual-exposure image, which utilized a 1:8 ratio, reveals the mountains in the background and the distinct edges of the light bulb.

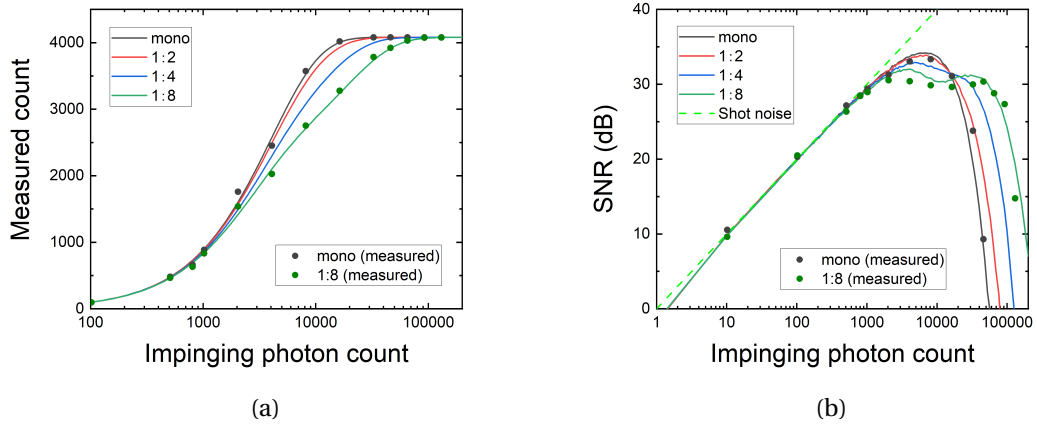


Figure 4.6: Measured count and SNR of mono- and dual-exposure mode. The solid lines correspond to the results of the Monte Carlo simulation, while the data points represent actual measurements.



(a) Mono-exposure



(b) Dual-exposure (HDR)

Figure 4.7: 2D 18-bit images of a real-life scene. The improvement of dynamic range can be visualized in the dual-exposure image.

4.2 3D imaging

4.2.1 Object ranging

We employed the same camera as previously mentioned and transitioned to gating mode for the purpose of object detection and ranging. The methodology is comprehensively explained in Chapter 2. In Fig.4.8, we depict the setup detailed in [35], which is used as an illustration for multi-object ranging. This setup incorporates a synchronized diffused light source and the SPAD camera. The scene consists of a Semi-transparent plate and an opaque sphere.

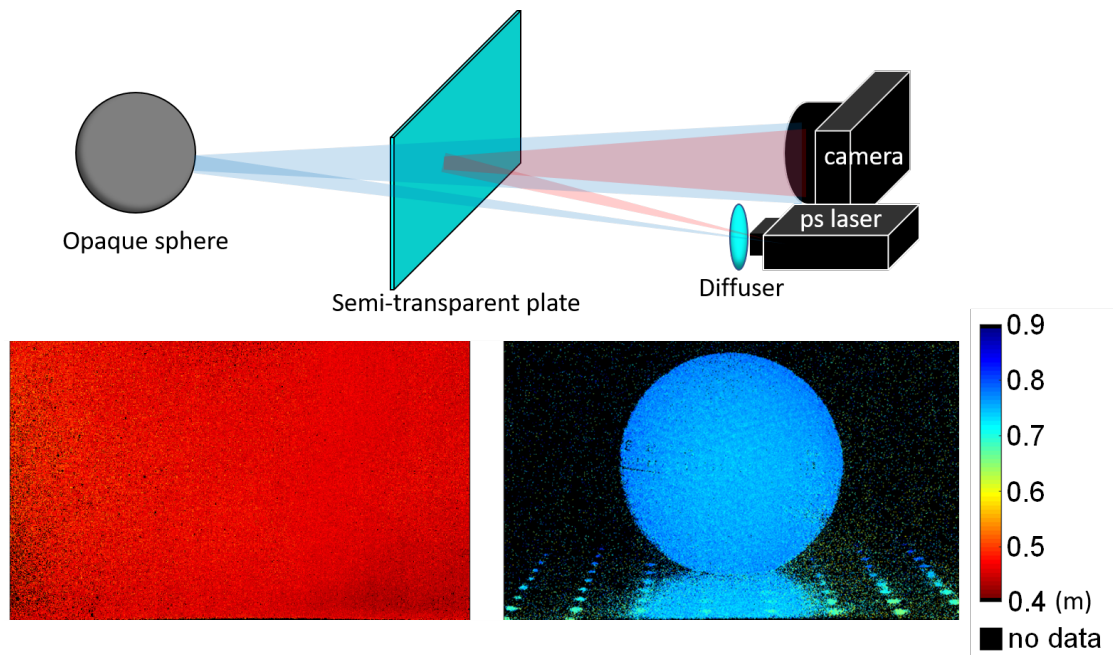


Figure 4.8: Multi-object ranging setup (top) and measurement result (bottom) [35].

As the depth reconstruction is done by finding the rising edge of the gate as shown in Chapter 2 Fig.2.10, the noise component does not have a noticeable effect on the accuracy of ranging unless the reflected signal is completely overpopulated by the dark counts.

The resolution in depth is determined by the precision of the gate shift step. Consequently, achieving greater depth resolution and extending the maximum measurable depth involves trading off acquisition time as the total acquisition time is proportional to the total number of gate positions. In comparison to Direct Time-of-Flight (DToF) LiDAR systems, where the reflected photons are directly time-binned, gating methods do indeed exhibit a speed disadvantage. In applications demanding rapid response times like automotive sensors, DToF LiDAR systems would be more suitable. Nonetheless, DToF LiDAR systems necessitate time-binning components like Time-to-Digital Converters (TDC), which introduce complexity to the circuitry and consequently hinder the scalability of the sensor array. In contrast, gating circuitry, as demonstrated in this study, offers improved scalability for sensor arrays.

To demonstrate the advantages of a large-scale array with gating circuitry, we further explore applications that require 3D information acquisition.

4.2.2 Fluorescence lifetime imaging

As mentioned in the introduction, efforts have been made to downscale microscopy systems for use in various challenging environments. We utilized the timing capabilities of the SPAD camera to showcase an application that offers enhanced functionality in such contexts. Fluorescence lifetime imaging microscopy, referred to as FLIM, stands apart from conventional fluorescence imaging methods as it focuses on assessing the temporal characteristics of a fluorophore, namely its fluorescence lifetime [122]–[124]. The fluorescence decay can be influenced by factors in the fluorophore’s environment, including oxygen concentration, pH levels, and protein-protein interactions, among others [124]–[126]. Consequently, the derived lifetimes can unveil contrasts within the sample that wouldn’t be perceptible from fluorescence intensity measurements alone. FLIM finds extensive application in the field of biological sciences [127], [128]. For example, in cancer research, FLIM has been employed for tasks such as cancer cell detection [129]–[132], anti-cancer drug delivery [133], [134], and studies on the effectiveness of anti-cancer drugs [135], [136]. Moreover, FLIM has started gaining significance in clinical diagnostics [136]–[138]. However, its widespread implementation in clinical settings is still limited due to constraints related to imaging speed and field of view (FOV) of existing FLIM systems [138]. These challenges stem from the fact that the intrinsic lifetimes of endogenous fluorophores and fluorescent proteins typically fall within the range of 0.1 to 7 ns [127]. Given the presence of various potential quenching interactions that further reduce lifetimes [124], [139], [140], detectors with sub-nanosecond temporal resolution are necessary for accurate FLIM. Commercially available systems often rely on confocal microscopes equipped with detectors suitable for point-scanning, such as photomultiplier tubes or Charge-Coupled Device (CCD) camera, and utilize time-correlated single-photon counting (TCSPC) electronics to meet the demanding temporal resolution requirements [141].

However, point-scanning systems are susceptible to photo-bleaching due to the high optical energy in the employed light pulses. These systems are also more complex to scale down. Additionally, they cannot immediately provide comprehensive information for the entire FOV, a limitation that becomes significant when dealing with dynamic scenes or in vivo applications. It is worth noting that while higher laser power in each spot with 2-photon excitation can be beneficial, in our case of 1-photon excitation, the samples are already prone to bleaching even with an average power of only a few mW. In this context, an analytical comparison between raster scanning and wide-field data acquisition for FLIM experiments suggests that in the scenario of dim or sparse samples, wide-field acquisition can accelerate the process by up to N^2 times in comparison to raster scanning. Here, N represents the number of pixel rows in a square array detector [142]. Consequently, larger detectors, like the SPAD array employed in this study, hold significance for imaging dim samples commonly encountered in biologically relevant experiments.

The primary benefits offered by SPAD arrays in comparison to conventional CCD/CMOS cameras include their picosecond temporal resolution and single-photon sensitivity. Moreover, gated SPAD cameras provide an enhanced pixel fill-factor, resulting in improved photon detection probability compared to TCSPC SPAD cameras, which necessitate more on-pixel electronics. We employ the Megapixel SPAD array operating in gating mode, described in Section 2.2.2, to showcase this advantage.

The fluorescence signal follows an exponential decay after the fluorophore is excited by a laser. With a defined gate length of 3.8 ns, the gate is scanned in steps that can be as small as 36 ps. To obtain the full characteristic of a single-exponential fluorescence decay, the starting gate position is tuned to be prior to the laser excitation. At each gate position or frame, an 8-bit spatially resolved image is obtained. The data within the image stack along the temporal axis representing the convolution of the lifetime response with the camera's temporal gate, which is shown in Fig.4.9.

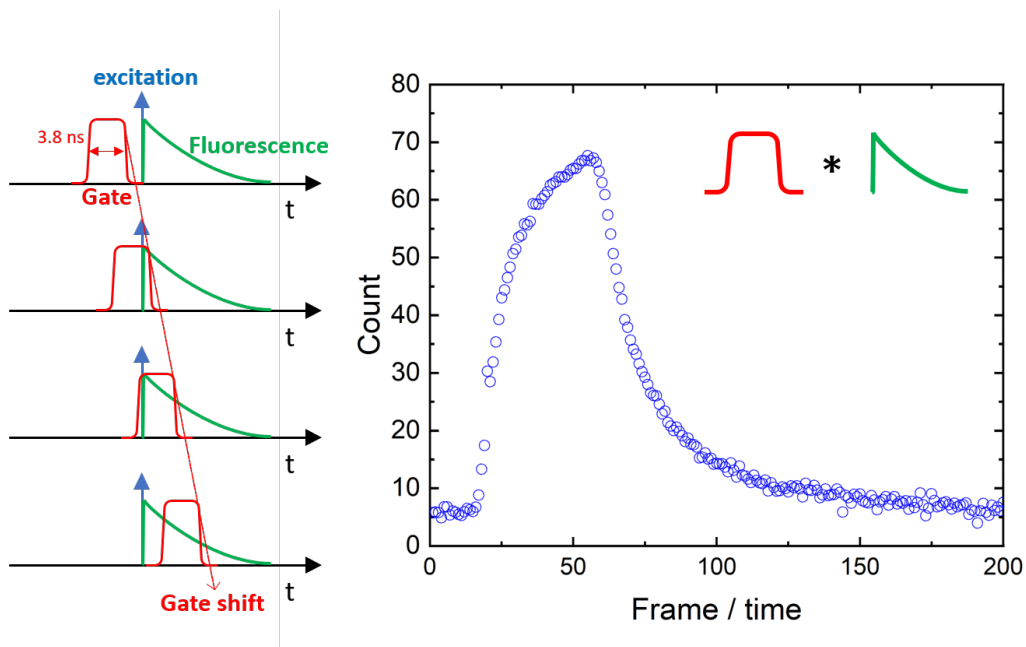


Figure 4.9: Principle of time-gated acquisition. Fluorescence decay is captured using a series of gates (3.8 ns width), each shifted by a minimum of 36 ps. Each 8-bit image frame corresponds to the convolution of the gate and a distinct segment of the fluorescence decay signal.

Lifetime retrieval: We employed different methods to extract the fluorescence decay lifetime and subsequently compared the results obtained from these methods.

The first method is the least-squares (LSQ) deconvolution. This approach usually requires significant computational resources, even with the computational speed improvements offered by Graphics Processing Units (GPUs). Prior to processing, the data undergoes background subtraction and pile-up correction. The pile-up correction process is described by the equation:

$$I_{cor} = -I_{max} \ln \left(1 - \frac{I_{rec}}{I_{max}} \right). \quad (4.12)$$

In this context, I_{cor} represents the pile-up corrected counts, I_{max} stands for the maximum achievable photon count (which varies based on the bit depth, such as 255 for 8-bit image), and I_{rec} denotes the specific recorded value at a pixel. To provide a clearer understanding, this equation serves as the inverse function of Equation 4.4. The importance of the pile-up correction arises from the nonlinear response characteristics of SPADs. This correction provides us with the accurate impinging photon count.

Background, or noise, removal is achieved by calculating the average of the initial few frames, taken before the decay signal starts, and subtracting this average value from all frames. We apply a thresholding procedure to exclude pixels with photon counts less than a certain threshold value, denoted as N_{tot} , which signifies the cumulative counts across gate position. This step effectively removes pixels with negligible signals.

In the deconvolution method, a model representing the fluorescence decay is convolved with the IRF, and then compared to the measured data through least squares minimization. The fluorescence decay is modeled as:

$$d(t) = \begin{cases} A_0 \exp(-\frac{t-t_0}{\tau}) + b & t \geq t_0 \\ b & t < t_0, \end{cases} \quad (4.13)$$

where τ is the fluorescence lifetime, t_0 is a temporal offset, b is a constant that accounts for a signal offset induced by a non-zero background, and A_0 is an amplitude parameter corresponding to the number of photon counts. The IRF, which represents the gate profile, is modeled as a super-Gaussian function that matches the measured gate profiles of each pixel. The least-square fitting outcome provides the fluorescence lifetime.

Alternatively, rapid visualization techniques like phasor analysis have been suggested [143] and effectively applied in the analysis of time-gated SPAD array FLIM data [144]. Moreover, beyond the numerical methods discussed earlier, the progression of machine learning techniques [145] has empowered researchers to employ deep learning frameworks to swiftly extract information about the exponential decay time and component fractions from FLIM data without the need for extensive fitting [146], [147]. In this context, we utilize an artificial neural network (ANN) to extract the lifetime information for each pixel within the SPAD array.

The configuration of the ANN is illustrated in Fig.4.10. The ANN architecture comprises an input layer, three hidden layers, and an output layer. Each of these layers consists of a fully-connected dense layer, followed by a rectified linear unit (ReLU) activation function. The input layer, consisting of 200 nodes in the example illustrated in Fig.4.9, is fed with a normalized fluorescence decay signal, presented as a 1D vector with elements equal to the number of gate shifts (frames). Subsequently, the output of the input layer is passed sequentially through the

ANN. As the layers progress, the subsequent hidden layer were optimized to 100, 50, and 25 nodes, respectively. Finally, the output layer generates an estimated value for the fluorescence decay lifetime. All computations were performed using TensorFlow.

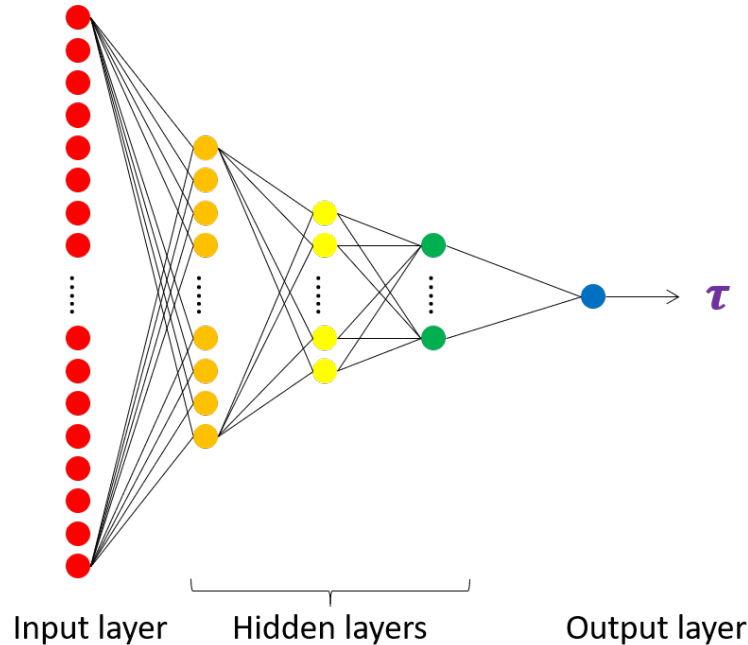


Figure 4.10: The ANN architecture for retrieving fluorescence lifetime.

We utilized synthetic fluorescence decay curves-lifetime pairs, which were numerically generated, as the training data for the ANN. For parameter ranges, we selected the following intervals: decay lifetime (τ) from 0.5 ns to 5 ns, decay start time (t_0) from 5 ns to 10 ns, decay amplitude (A_0) from 2 to 32, and gate width from 3.6 ns to 6 ns. Our range of lifetimes covers the domain of lifetimes characteristic to the dye, acridine orange. Differences in the starting points of decay result from variations in the signal transmission time across different regions of the SPAD array. The variation in decay intensity can come from factors like the local concentration of fluorescent dye due to cellular structure. Gate width variations are inherent to the SPAD array itself.

We conducted training using mini-batch gradient descent, employing a mini-batch size of 128 and utilizing the adaptive moment estimation (Adam) algorithm as our gradient descent optimizer. The loss function employed was the mean squared error (MSE), calculated between the actual ground truth lifetime values of our mini-batches and the corresponding predictions made by the ANN. The results indicate that the test set loss was approximately equivalent to the validation loss and did not differ significantly from the training set loss. This suggests that the network did not undergo overtraining.

Samples of *Convallaria* and the human fibrosarcoma cell HT1080 are projected onto the camera with a spatial sampling of 0.47 μm and 0.33 μm per pixel. The outcomes of datasets

comprising 30 frames are depicted in Fig.4.11.

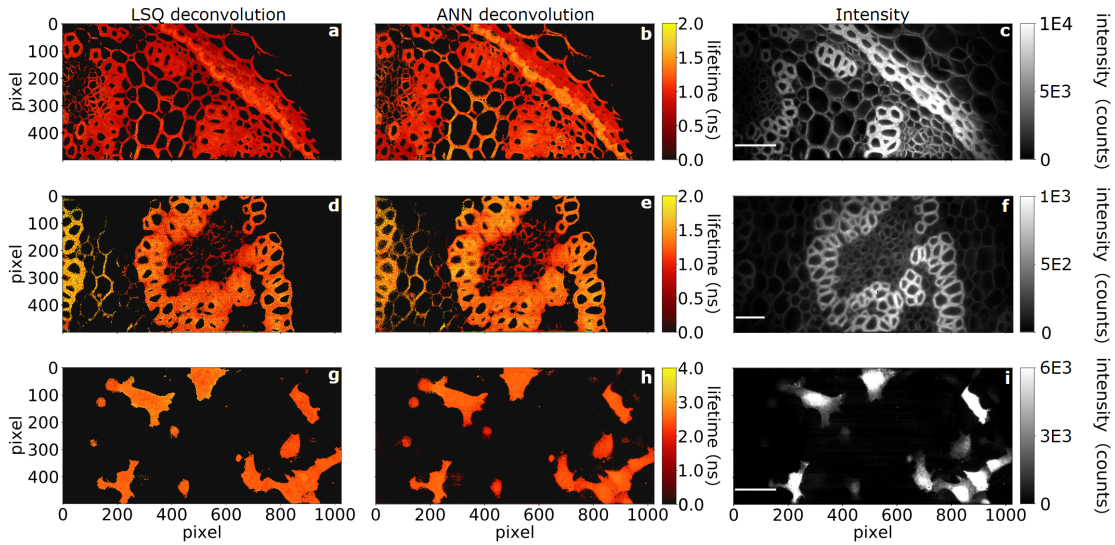


Figure 4.11: Wide-field fluorescence lifetime measurements of Convallaria and HT1080 cells. The first column shows results from LSQ deconvolution, the second column from ANN lifetime retrieval, and the third column displays a temporal sum of pile-up and background corrected intensity data, with selected intensity values to enhance dim structures. (a)–(c) shows the HPC measurements (acquisition time: 10 s). LSQ deconvolution took 56 minutes, while ANN took only 2.7 seconds, producing similar mean lifetime values. Spatial sampling was at 0.47 $\mu\text{m}/\text{pixel}$. (d)–(f) shows the LPC measurements of Convallaria obtained in 1 second. LSQ and ANN have processing times of 58 minutes and 2.7 seconds. Spatial sampling remained at 0.47 $\mu\text{m}/\text{pixel}$. (g)–(i) shows the HT1080 cells expressing Clover. LSQ and ANN retrievals had processing times of 23.2 minutes and 3.6 seconds respectively, while spatial sampling was at 0.33 $\mu\text{m}/\text{pixel}$. Notably, HT1080 cells appeared dimmer than Convallaria cells, generating around 100 photons per second on average in the brightest region compared to around 2500 for Convallaria. All images are presented with a 50 μm scale bar.

We captured images of Convallaria samples using both 'high photon counts' (HPC) at a 10-second acquisition rate (Fig.4.11a–c) and 'low photon counts' (LPC) at a 1-second acquisition rate (Fig.4.11d–f). The HPC dataset was generated using a gate shift of 504 ps and an exposure of approximately 330 ms. To achieve a 1 Hz acquisition rate, the exposure was reduced to approximately 33 ms per frame. Fig.4.11 illustrates that lifetime data can be successfully extracted from both the HPC and LPC datasets. However, analyzing the LPC data is more complex due to its lower SNR. In these cases, the total photon count in the LPC data falls below 2700 photons per pixel, while the HPC data exceeds 8500 photons. Nevertheless, both the LSQ and ANN methods yield similar mean lifetime values for both HPC and LPC data. The mean lifetime and standard deviation values are shown in Table.4.1.

The primary advantage of the ANN lies in its potential for significantly faster processing compared to LSQ. Leveraging a pre-trained model, the ANN-based retrieval process takes less than 4 seconds to process the entire image. This time efficiency is three to four orders of

Table 4.1: Comparison of LSQ and ANN results for different datasets

Data	LSQ (ns)	ANN (ns)
HPC	1.29 ± 0.49	1.22 ± 0.27
LPC	1.20 ± 0.53	1.28 ± 0.34
HT1080	2.41 ± 0.29	2.31 ± 0.34

magnitude faster than the LSQ method, which, as evidenced in our tests, took tens of minutes. It's important to highlight that our approach involves the independent fitting of each pixel, without relying on conventional 'global fitting' strategies, where data is averaged spatially and/or temporally [148].

Although *Convallaria* is widely used for evaluating FLIM systems [149]–[152], its high signal intensity may not accurately reflect the signal levels observed in various biological samples, such as transfected mammalian cells. In order to offer a more practical illustration, we present FLIM data obtained from samples relevant to cancer research: fixed HT1080 (fibrosarcoma) cells that were transfected with pcDNA3-Clover [153], resulting in the expression of a protein with a single fluorescence lifetime (depicted in Fig.4.11g,h). The HT1080 cell data was collected using a 108 ps gate shift, with a total acquisition time of approximately 400 seconds.

Similar to the *Convallaria* results, the quantitative agreement between the ANN and LSQ outcomes shows a small difference between LSQ and ANN of 0.10 ± 0.05 ns. Our determined lifetime for HT1080 cells transfected with Clover is similar to a previously documented value of 2.6 ns [154]. The large size of the sensor enables the concurrent high-resolution imaging of multiple cells over a wide field of view. It's worth mentioning that the acquisition time could be shortened by increasing the gate shift and acquiring fewer frames, although this might result in reduced sampling of the fluorescence decay and potentially less accurate lifetime retrieval.

The experimental results validate that the noise model in our experiments could be best described as a mixture of Poissonian noise originating from photon counting statistics, exhibiting a square root relationship with the signal, and Gaussian noise, stemming from the light source and electronics. Testing with synthetic data with 4 times more noise than the actual measured value has shown that both methods can accurately recover lifetimes with a resolution of 300 ps (equivalent to 2 standard deviations) within the range of 0.75 to 4.75 ns. This shows the inherent robustness of both LSQ and ANN against noise.

Lastly, we present a 3.64 megapixel image of our *Convallaria* sample to demonstrate the possibility of acquiring a very large FOV using the 0.5 megapixel SPAD array. The result is shown in Fig.4.12. The FOV is 618×640 μm , maintaining the same spatial sampling of 0.33 μm per pixel as in the previous figures. Employing mosaic acquisition with approximately 10% overlap between mosaic tiles, we acquired the data. Notably, our ANN method required only 36 seconds to recover lifetime information from this dataset. This retrieval time could

potentially be reduced further by processing individual pixels or batches of pixels in parallel.

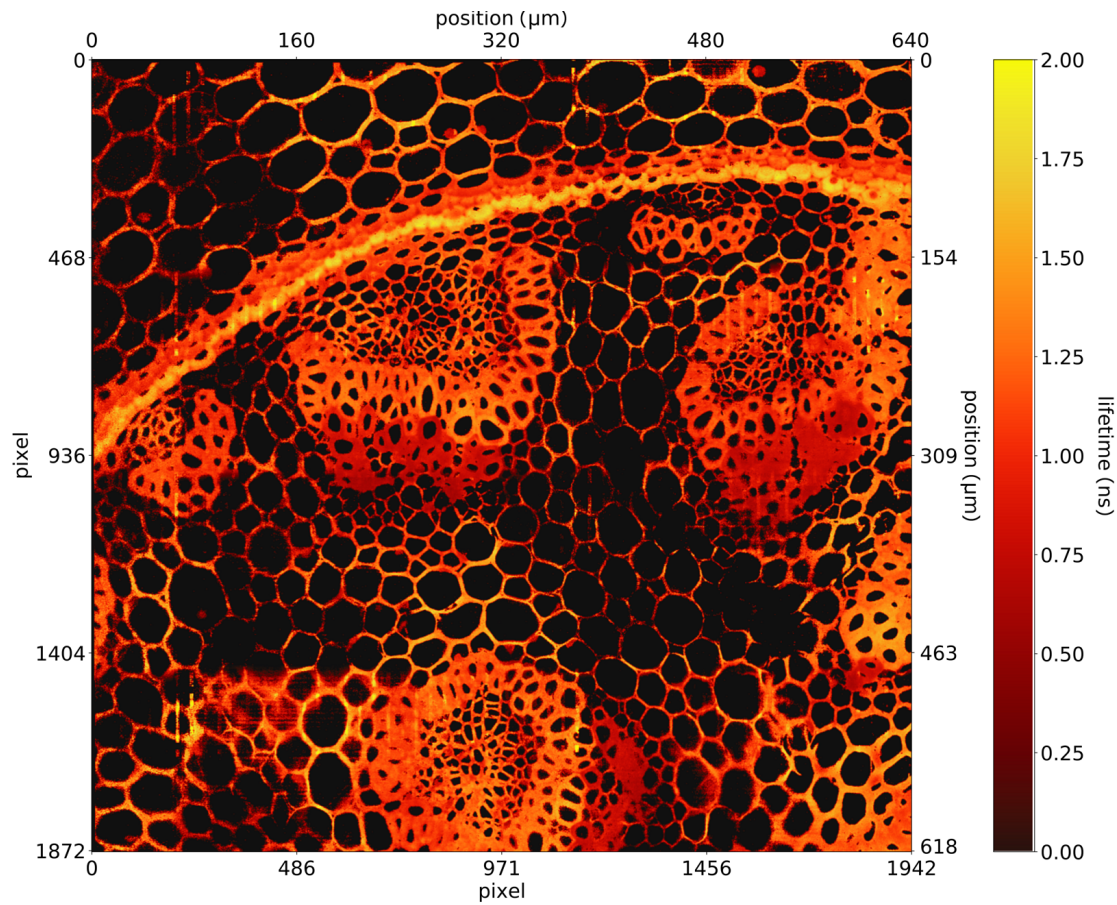


Figure 4.12: A 3.64 megapixel wide-field FLIM image created by stitching together 8 tiles of the Convallaria sample dataset, corresponding to a field of view of about $618 \times 640 \mu\text{m}$. The entire acquisition process took around 16 minutes in HPC mode (which can be decreased to 10–20 s in low photon count mode), and the subsequent ANN lifetime retrieval required approximately 36 seconds.

4.3 4D imaging

4.3.1 Hyperspectral fluorescence lifetime imaging

To further explore the advantages of the 2D SPAD array, we have attempted to use the camera as a tool for an application that is typically performed with a 1D linear array, namely, obtaining spectral information. As previously mentioned, 1D SPAD arrays are well-suited for projecting spectral information and integrating timing electronics on the array periphery. These systems, such as FLIM and Raman spectroscopy, operate in a point (0D) scanning mode, where spectral information is projected onto a 1D sensor [155]–[158].

With the addition of a second dimension to the sensor array, we can, in principle, obtain an extra spatial dimension. Instead of point scanning the sample in a plane, we perform line scanning, which reduces the scanning process to a single line. This reduction in scanning dimensions results in a significant reduction in scanning time, effectively reducing it by one order of magnitude. The concept was initially introduced in [159] and has now been realized in this work as a proof of concept.

We built a confocal microscope system, depicted in Fig.4.13, that can interchange between (a) point scanning and (b) line scanning mode.

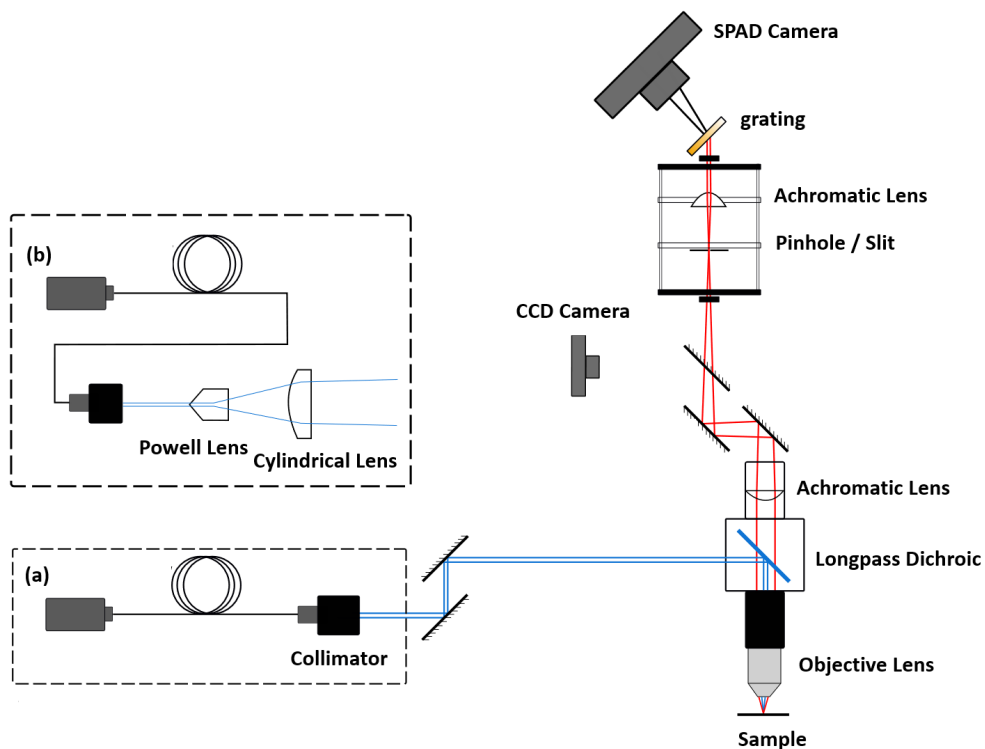


Figure 4.13: Hyperspectral fluorescence lifetime imaging setup

The setup consists of a pulsed laser operating at a 25 MHz repetition rate with a wavelength

Chapter 4: Results of SPAD-based applications

of 482 nm. The laser is fiber-coupled into a collimator, resulting in a 1 mm spot size. For the line illumination configuration, the spot then passes through a Powell lens [160] with a 30° fan angle and a cylindrical lens with a focal length of 38.12 mm, resulting in a line length of 10 mm. The laser is then used to excite the sample, reflecting from a long-pass 505 nm dichroic mirror. The signal from the sample, which has a longer wavelength, is collected by an objective lens with an entrance pupil of 8.4 mm. The signal that passes through the long-pass dichroic mirror then has two paths selected by a flip mirror. One path goes to a CCD camera for real-space alignment and tuning of the laser focus, while the other goes through either a pinhole or a slit, depending on the operating mode. The spectral information is then dispersed to the camera by a transmission grating with 1600 lines/mm.

We can position the camera using the known transmissive grating expression:

$$a[\sin(\theta_m) - \sin(\theta_i)] = m\lambda, \quad (4.14)$$

where a is the grating spacing, θ_m is the angle of the light of order m exiting the grating, and θ_i is the incident angle.

By positioning the SPAD camera, we can project the spectrum with roughly a 150 nm range onto the array distributed over 1024 SPAD pixels. This gives us approximately 0.15 nm spectral resolution. We calibrate the spectral resolution using a supercontinuum source and acquire the result shown in Fig.4.14.

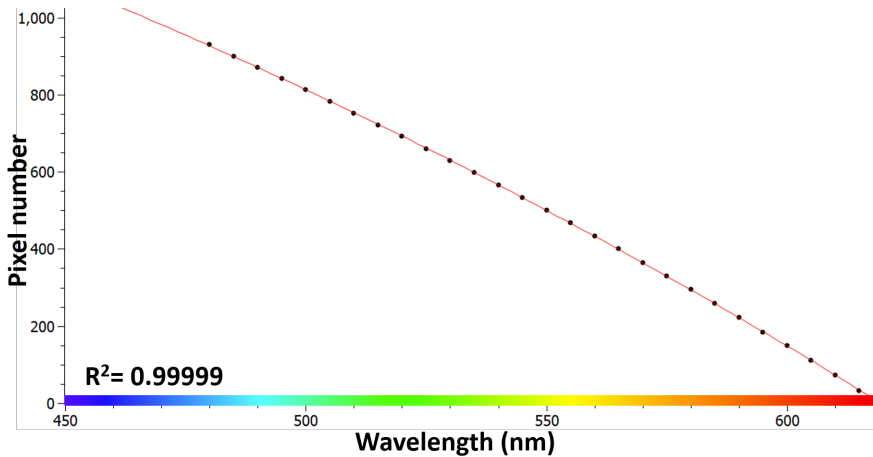


Figure 4.14: Spectral resolution calibration

The principle of spectral fluorescence lifetime imaging is depicted in Fig.4.15. To begin, we locate the region of interest using the CCD camera, as illustrated in the top left of the figure. The laser line is then focused onto the sample. Here, we define the laser line as the x-axis and the scanning direction as the y-axis. At each y-position, the signal emitted from the excited sample is projected onto the vertical axis of the camera, as shown in the top right of the figure. This provides us with a spatial resolution of 500 pixels in the x domain. The horizontal axis of

the camera, with 1024 pixels, corresponds to the signal wavelength, as explained earlier. At every y -position, the gating mode is applied with a certain number of gate shifts, or frames, as detailed in the previous FLIM chapter. Once the gate shift is completed, the sample is automatically shifted using a translation stage to move to the next y -position.

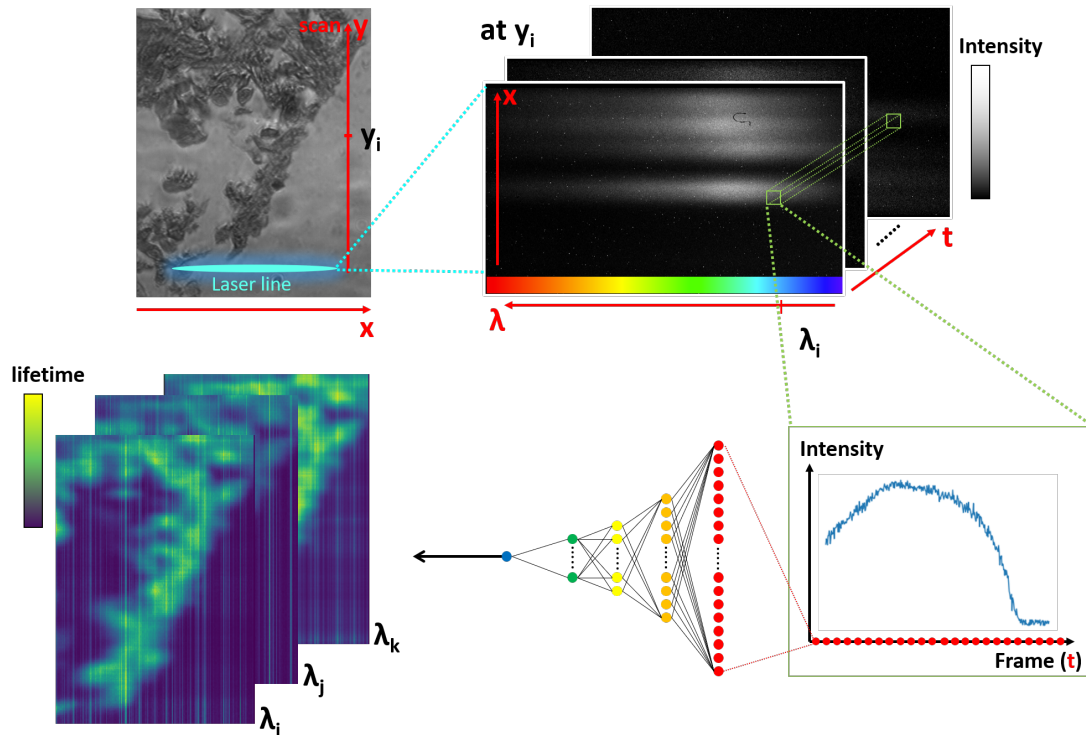


Figure 4.15: Principle of hyperspectral fluorescence lifetime imaging

An example of the image stack with information for x , λ , and t at position y_i is shown in the top right of the figure. After completing the scanning in the y -direction, we obtain a 4D matrix of intensity values for each x , y , t , and λ .

To determine the lifetime, we have the flexibility to choose a specific wavelength of interest, denoted as λ_i , or a range of wavelengths, and plot the intensity profile over time. This yields the same intensity profile as demonstrated in the previous FLIM section. Using this intensity-over-time profile, we employed a neural network to calculate the lifetime. Overall, this method allows us to obtain lifetime measurements at any wavelength within the entire region of interest.

We implemented reverse gate shifting since the tail of the fluorescence exponential decay is the primary factor influencing the lifetime. By reversing the gate, we effectively bypass the convolution of the gate with the rising edge of the fluorescence signal. This reduction in data processing cuts acquisition time by one third, resulting in a faster overall process.

The total acquisition time depends on two factors: the total number of steps in the y -direction,

Chapter 4: Results of SPAD-based applications

affecting the total field of view, and the number of gate shifts, influencing the accuracy of lifetime fitting. As demonstrated in the previous section, the neural network is capable of accurately determining the lifetime even with a limited number of gate shifts. Therefore, one can optimize the number of gate shifts using the neural network to achieve an optimal acquisition time.

Regarding spatial and spectral resolution, there is a trade-off between resolution and the SNR. To improve SNR, one can combine several pixels, as demonstrated in the example.

Fig.4.16 displays the results obtained from a sample consisting of mixed microbeads, each with a known fluorescence lifetime. Specifically, we have beads emitting with a 5.54 ns lifetime within the wavelength range of 528 to 708 nm, and beads emitting with a 2.71 ns lifetime within the range of 545 to 800 nm. The image on the left is captured in brightfield, while the right-side image represents the lifetime data.

The lifetime image was acquired through a process involving 50 steps of 50 μm scanning in the y-direction, 400 steps of gate shifting with an interval of 36 ps, and subsequent retrieval of the lifetime map using a neural network. It's important to note that some beads are missing in the lifetime image, as indicated by the encircled areas. This demonstrates the system's capability to distinguish beads with different characteristics.

Our range of interest in terms of wavelength falls between 500 nm and 650 nm. The majority of the signal from the 5.54 ns lifetime beads can be collected by the horizontal axis of the camera. Beads with lower lifetimes emit primarily at wavelengths above this range, where SPAD sensitivity is also lower. Additionally, as confirmed by the Leica SP8 FLIM Microscope, beads with lower lifetimes emit weaker signals. Furthermore, our laser source, with a maximum average power of 2 mW, is considerably weaker compared to the source used in [160] (2 W), where a Powell lens was used to achieve line illumination. Additionally, our system has a much larger field of illumination due to the selected objective lens, resulting in an overall power per unit area that is 9 to 10 orders of magnitude lower.

Despite these drawbacks, it's noticeable that the edges of the visible beads adjacent to the missing beads exhibit a lower lifetime. This phenomenon can be attributed to the low intensity of these missing beads, which may have influenced the neural network to provide a lower lifetime estimation due to the averaging effect with the scattered light from the low lifetime beads.

In summary, our system serves as a proof of concept for utilizing a 2D SPAD array as the detector in line scanning hyperspectral FLIM systems. This versatile optical system can be adapted for use in various applications, such as Raman spectroscopy or Laser-induced breakdown spectroscopy, both of which find common usage in exoplanet exploration [161].

For further enhancements of such a system, several considerations should be made. Firstly, it is crucial to select a laser with power that corresponds to the field of illumination to maintain

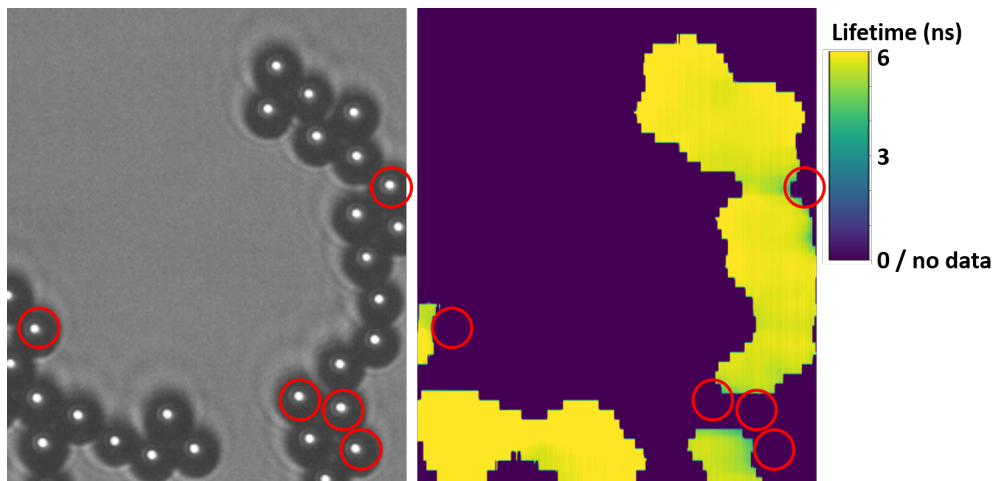


Figure 4.16: Hyperspectral fluorescence lifetime imaging results

a reasonable power per unit area for the target sample. This ensures optimal excitation and signal collection. Additionally, one can explore the option of sacrificing spectral resolution to achieve a wider range of collectable wavelengths. This trade-off allows for the capture of more comprehensive spectral information, which can be particularly advantageous in applications demanding broad wavelength coverage. By addressing these factors, we can advance the capabilities and utility of such hyperspectral imaging systems.

4.3.2 Light-in-flight imaging

To demonstrate the potential of SPAD-based sensors in the field of astronomy imaging and astrophysics, we showcase light-in-flight imaging that captures apparent superluminal motion, an apparent faster-than-light motion observed in several astronomical events, to highlight the capabilities of high-speed imaging. Various methods have been explored to capture light while it is in motion [162]. One of the earliest techniques for light-in-flight imaging is holography [163]–[165]. More contemporary approaches involve the use of streak cameras [166], [167]. In recent times, the application of 1D and 2D SPAD arrays, each comprising a maximum of a few thousand pixels, has successfully enabled light-in-flight imaging systems [168]–[173]. These sensors, benefitting from enhanced data acquisition speed through pixel-parallel detection with picosecond time resolution and single-photon sensitivity, are capable of capturing 3D spatiotemporal information (x, y, t) . However, due to the limited information acquired by these smaller arrays, the depth information has remained insufficient.

Researchers have explored a method for extracting additional positional information along the z -axis from the collected spatiotemporal data [174], [175]. The authors highlight that variations in the propagation angles within the xy plane result in distinct apparent velocities of light. Consequently, comparing the acquired spatiotemporal dataset with this theory could lead to an estimation of the z component within the light propagation vector. However, this

Chapter 4: Results of SPAD-based applications

analysis is limited to simplified scenarios involving either straight light paths within the xz plane that intersect a fixed point or situations where the angle between the light propagation vector and the focal plane is less than 10 degrees. The accuracy of estimating the z component is also influenced by the number of pixels. While CMOS cameras achieve megapixel ranges [176], their timing precision at the nanosecond scale restricts their spatiotemporal resolution.

To tackle these challenges, we utilize the capacities of the large-scale SPAD array along with its remarkable timing resolution by employing the gating mode. This approach enabled us to capture the superluminal phenomenon, indicating apparent motion faster than the speed of light. Leveraging a sufficient number of pixels, we successfully reconstructed the complete 4D light-in-flight trajectory (x, y, z, t) .

The experimental setup is illustrated in Figure 4.17. An arbitrary 3D light trajectory is generated by a 510 nm laser emitting pulses with an average power of 2nW and a pulse width of 130 ps. This trajectory is achieved using a combination of mirrors positioned on an optical table. Synchronization between the laser and the SPAD camera is maintained through a reference function generator operating at 40 MHz. In our setup, the xy -plane is considered as the camera plane, while the z direction is defined as perpendicular to the camera plane.

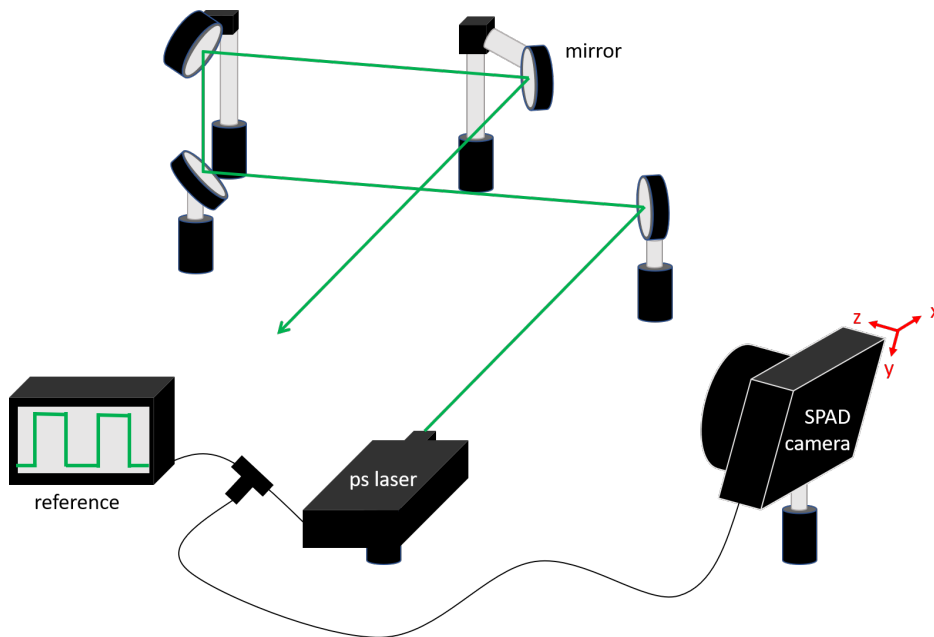


Figure 4.17: The experimental setup. The laser and the SPAD camera are synchronized with a reference function generator.

It's important to note that what the camera actually observes is **not** the light within the defined light path, but the light that reaches the camera through **scattering events** along the path. To predict the observed outcome, we can visualize the light propagation and the scattering events using a light cone in Minkowski spacetime. An example is presented in Figure 4.18a, where the light travels in the direction of $-z$. The light moves at its speed, c , along the $(0,0,-1)$ vector. The

light scatters along its path and generates a new light cone at various scattering points (each marked with different colors). The observers, or cameras (C_1 to C_5), are fixed in 3D Euclidean space (xyz -space). They can only observe the scattered light when the projection of the light cone reaches them, or, in other words, when the scattered light reaches the cameras. In this context, the variable t represents the moment when the light originating from a laser source arrives at a specific point (x, y, z) , or the scattering point along the light path.

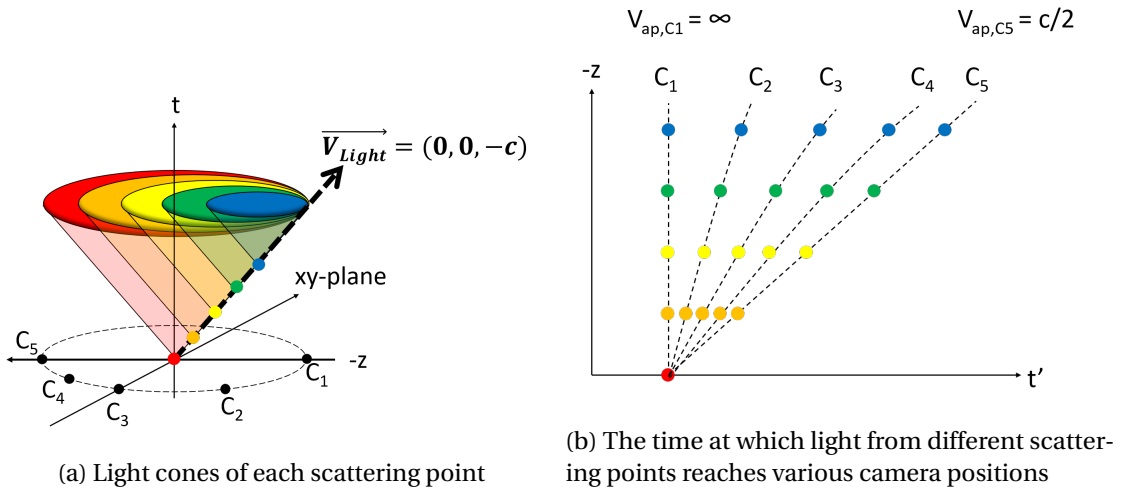


Figure 4.18: In this example, light travels along the $(0,0,-1)$ direction. The resulting apparent light speed is infinite for C_1 and $c/2$ for C_5 .

The time of arrival, also known as the moment when the scattered light becomes visible to the camera, is indicated as t' . The relationship between t' and the camera positions is illustrated in Fig.4.18b. For C_1 , the light approaches the camera directly, causing the scattered light from any point along the light path in space to reach the camera simultaneously. This leads the observer to perceive the light as if it's moving at an infinite speed. In contrast, for C_5 , where the light moves away from the observer, the scattered light takes twice the time to reach the camera, resulting in an apparent light speed that is half of c . In this scenario, as the orientation of the light pulse changes concerning the camera, the observer will perceive an apparent light speed different from c . Generally, if the light approaches the camera in space, the observer will perceive a faster-than-light, or superluminal, motion.

The measurement outcomes are shown in Fig.4.19. In this figure, 9 frames from the complete gating measurement are displayed, each representing a different gating position. During this measurement, the gate width was configured to be 3.8 ns. To enhance clarity, the gating outcomes are overlaid with an intensity image of the setup captured by the SPAD camera in room light conditions. To provide a more precise representation of the laser pulse front's exact location, we compute the first derivative of the measured gate profile. Consequently, the illuminated pixels indicate the specific locations where the laser pulse front has arrived, offering a timing resolution of approximately 150 ps, which aligns closely with the rise time of the gate profile.

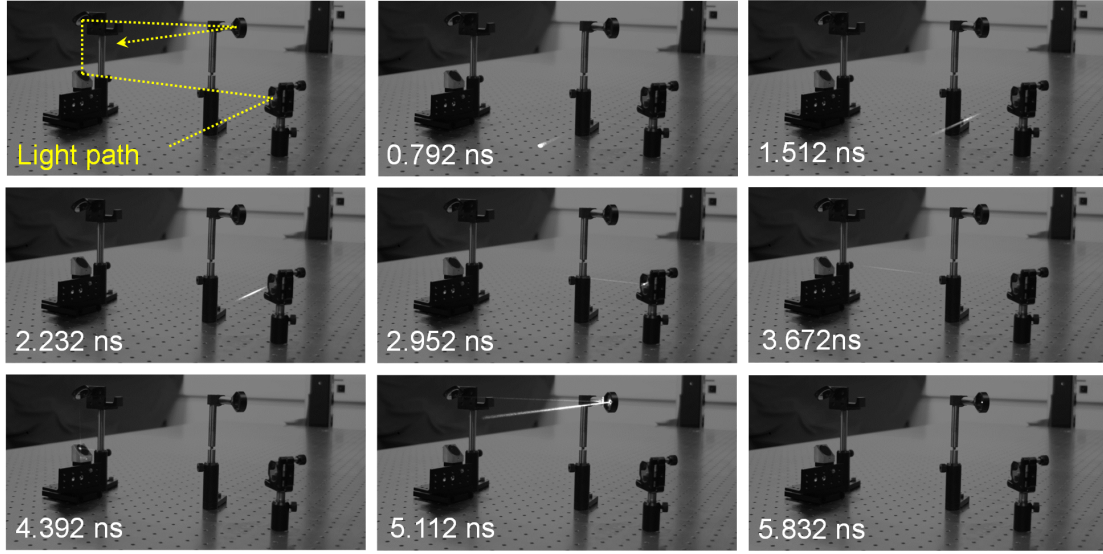


Figure 4.19: Experimental result of the light-in-flight measurement

The initial frame ($t = 0$) displays the intensity image before the laser pulse enters the field of view (FOV). The dashed line on the image corresponds to the predefined light path illustrated in Fig.4.17. The laser pulse front takes approximately 2 ns to reach the initial mirror, which is evident in the first 5 frames. As it reflects off the last mirror at $t' = 5.112$ ns, the apparent velocity of the laser pulse noticeably increases compared to the preceding 5 frames. With each frame offering a resolution of 150 ps, the apparent laser pulse's motion covers a distance significantly greater than $c \times 150$ ps, equivalent to 4.5 cm. This observation reveals superluminal motion. Leveraging this newfound information about the apparent light speed, we can derive an additional dimension beyond the xy-plane of the camera.

To develop an algorithm for reconstructing the light-in-flight path in 3D space, it is essential to establish a model that describes the relationship between the path itself and its corresponding projection onto the sensor. This is depicted in Fig.4.20. We define the center of the lens as the spatial origin. The initial position of the laser pulse is represented by the vector $\vec{r}_0 = (x_0, y_0, z_0)$, and the laser pulse's direction is given by $\vec{n} = (n_x, n_y, n_z)$. The position after the laser pulse has traveled for a duration of time t is thus $\vec{r}(t) = \vec{r}_0 + ct \cdot \vec{n}$.

Given the optical magnification of the lens, the laser's projected position on the sensor can be expressed as $\vec{r}_p = (x_p(t), y_p(t), z_p(t)) = \alpha(t) \cdot \vec{r}(t)$, where $\alpha(t)$ represents a time-dependent coefficient. As the sensor is situated on the lens's focal plane, it follows that z_p remains constant, corresponding to the lens's focal length. Consequently, we can deduce $\alpha(t) = z_p / (z_0 + ct \cdot n_z)$.

The laser pulse originating from r_0 at $t = 0$ arrives at $r(t)$ after a time interval of t . To observe

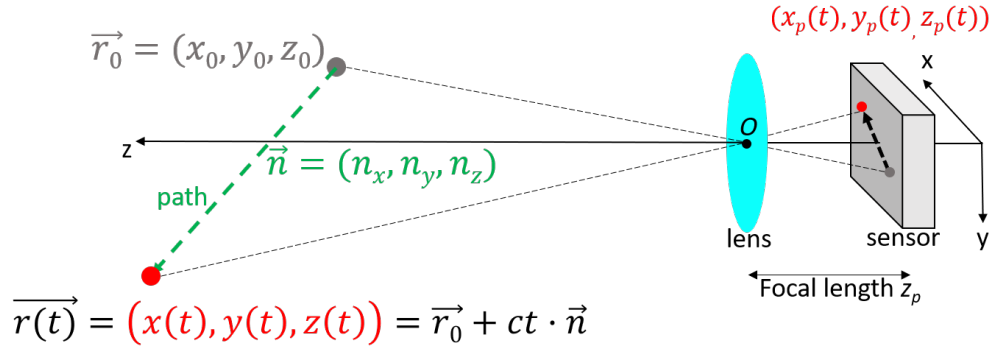


Figure 4.20: The model for reconstructing the light-in-flight path

the scattered light from $r(t)$ on the sensor, the time taken is given by:

$$t' = t + \frac{|\vec{r}(t)|}{c} = t + \frac{1}{c} \cdot \sqrt{|\vec{r}_0|^2 + 2ct(\vec{r}_0 \cdot \vec{n}) + c^2 t^2}. \quad (4.15)$$

Consequently, we can express the effective travel time of the laser pulse as:

$$t = \frac{1}{2} \cdot \frac{c^2 t'^2 - |\vec{r}_0|^2}{c^2 t' + c(\vec{r}_0 \cdot \vec{n})}. \quad (4.16)$$

Utilizing these equations, we can determine the projection of the laser pulse onto the sensor as follows:

$$x_p(t) = \frac{z_p}{z_0 + ct \cdot n_z} \cdot (x_0 + ct \cdot n_x), \quad y_p(t) = \frac{z_p}{z_0 + ct \cdot n_z} \cdot (y_0 + ct \cdot n_y). \quad (4.17)$$

The collected dataset is depicted in Fig.4.21a. Each data point corresponds to the projection of the scattered laser onto the sensor, providing 3D information (x_p^i, y_p^i, t^i) , where i denotes the label of each point. To reconstruct the light-in-flight path, it is necessary to segment the entire trajectory of the laser into multiple paths. This segmentation was achieved through the utilization of a 2D Gaussian mixture model for data clustering. Distinct clusters within the model represent paths originating from different points \vec{r}_0 and having various directions \vec{n} , which can be visualized in Fig.4.21b.

The data points within each cluster are then input into an optimization function:

$$(\vec{r}_0, \vec{n}) = \arg \min_{\vec{r}_0, \vec{n}} \left\{ \sum_i^N \left[x_p^i - \frac{z_p}{z_0 + ct^i \cdot n_z} \cdot (x_0 + ct^i \cdot n_x) \right]^2 + \sum_i^N \left[y_p^i - \frac{z_p}{z_0 + ct^i \cdot n_z} \cdot (y_0 + ct^i \cdot n_y) \right]^2 \right\}, \quad (4.18)$$

where N represents the total number of points within each segment. The resulting 4D light-in-flight reconstruction can be seen in Fig.4.22. It can be observed that the discrepancy between the reconstructed path and the actual light-in-flight path becomes more pronounced

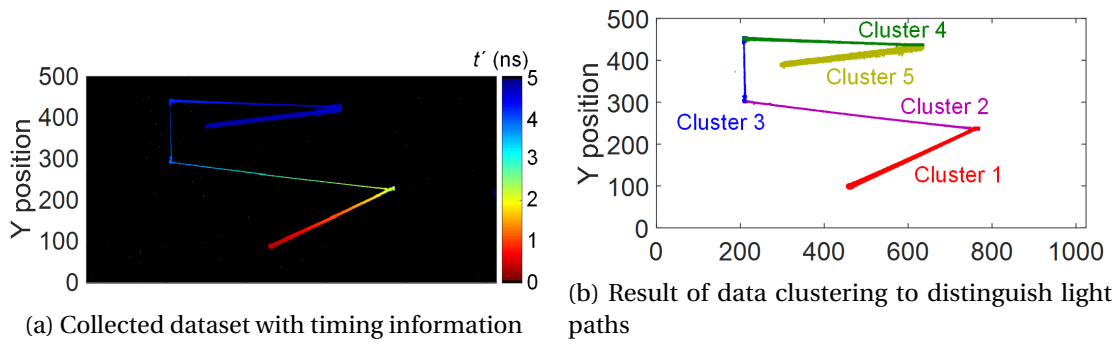


Figure 4.21: Dataset of the light-in-flight measurement

as the apparent light speed increases or when the laser pulse is moving towards the sensor. This phenomenon arises from the fact that these data points arrive at the sensor in close proximity in time t' . Consequently, the reconstruction experiences enhanced timing accuracy constraints owing to the restricted timing resolution. The presence of noise or hot pixels within the sensor array does not adversely impact the performance of path reconstruction. This is due to their elimination through the differentiation process applied to the brightened pixels.

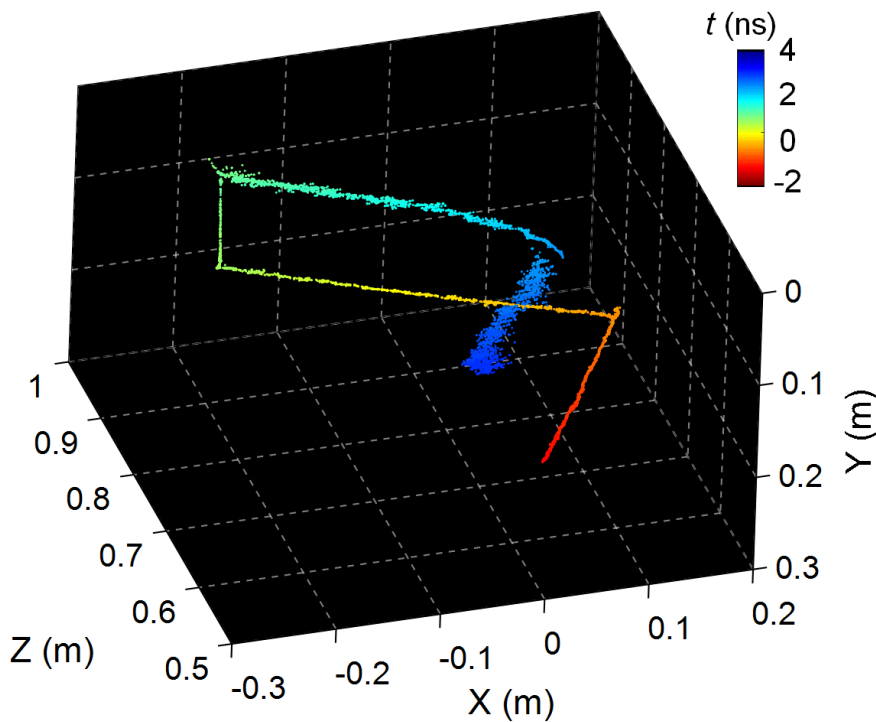


Figure 4.22: The light-in-flight reconstruction result with 4D information

4.4 Particle/radiation detection

Particle and radiation detection play a crucial role in both high-energy physics and space exploration. In the realm of high-energy physics, particle detectors serve to study the characteristics of subatomic particles generated during diverse experiments. These detectors are also instrumental in the quest for dark matter. In the realm of space exploration, radiation detectors are indispensable for study the space environment. They aid in detecting charged particles, high-energy photons, and cosmic rays. This knowledge is vital for charting upcoming exploration ventures and safeguarding spacecraft and astronauts against potential threats.

Solid-state detectors stand out among various particle detectors due to their exceptional granularity, which translates to high spatial resolution and fast time response. An illustrative example of a solid-state detector is the Timepix sensor family. This family encompasses hybrid pixel detectors, which have found utility in astronaut dosimetry and monitoring space events [177]. Another form of solid-state detectors comes in the form of monolithic detectors, where the complete readout circuitry is directly integrated into the sensor area, eliminating the need for 3D bonding, and making them more cost-efficient. Monolithic detectors have been harnessed for tracking charged particles, exhibiting impressive timing accuracy extending down to tens of picoseconds [178]. These detectors consist of diode structures that facilitate the collection of charge carriers generated during ionization as electrical signals. Their operation under moderate reverse bias enables linear-mode avalanche gain and the aforementioned exemplary timing performance.

Previous studies have already delved into the exploration of SPADs as particle detectors [60], [179]. Just like in the case of monolithic detectors, the increasing compatibility with CMOS technology permits the design of readout circuitry in close proximity to the sensor. Owing to the elevated electric field, SPADs are anticipated to exhibit enhanced timing capabilities compared to other types of radiation detectors. In this work, we introduce an updated iteration of the setup employed in the measurement detailed in [62].

For this particle detection experiment, we employed the identical variety of high-precision timing SPAD [68], each featuring a 25 μm diameter active area. These SPADs, which underwent proton radiation testing, are built with a circuit founded on cascode passive quenching and active recharge, as elaborated in Chapter 1. The chip is integrated into a compact system-on-board setup, drawing all control voltages from programmable digital-to-analog converters that are powered by a single 5 V supply. Within the pixel structure, digital inverters are utilized to discriminate the signal, employing a threshold set at half of the digital supply. However, due to the low power-supply-rejection-ratio in this gate, noise along the supply line could introduce timing uncertainties. To mitigate this, low-dropout regulators are positioned near the readout circuitry, supported by filtering capacitors that ensure stable and low-noise voltage levels for the front-end circuits. The sensor's high voltage was maintained with a ripple of less than 1 mV RMS, ensuring its stability. The output of the front-end circuit is linked to rapid SiGe comparators equipped with differential outputs. These comparators can drive

high-frequency 50 Ω cables, establishing a connection to the time-stamping electronics, specifically an oscilloscope. The output signal's slew rate is approximately 1.6 V/ns. Two of the aforementioned systems were arranged with the SPADs positioned back-to-back at a few centimeters' distance, which is visible in Fig.4.23.

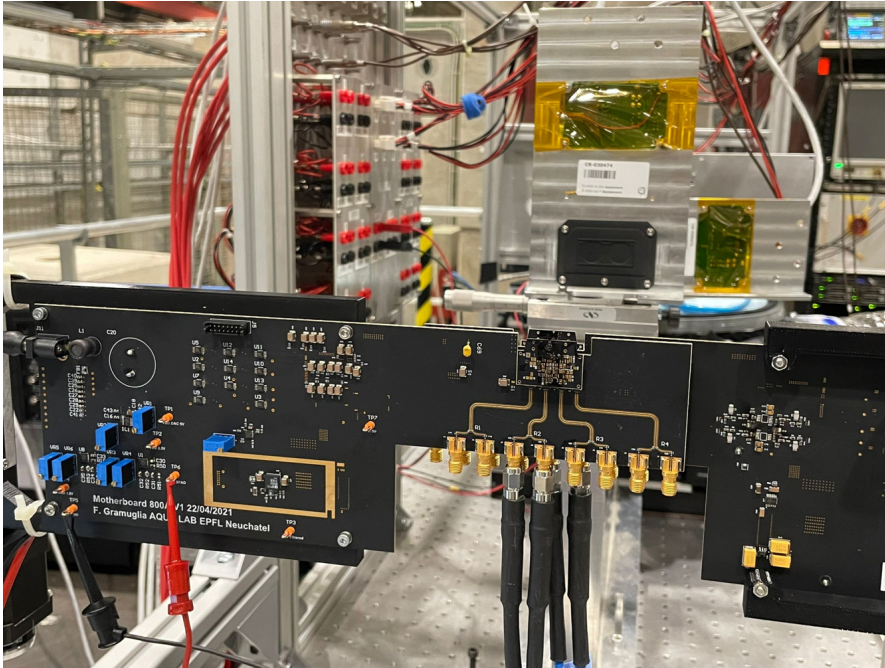


Figure 4.23: Particle detection experimental setup

Remote alignment was achieved using a stepper with 1 μm precision, aided by the UniGe FEI4 telescope [180], [181]. The SPADs and the telescope can be seen in the front and the back of Fig.4.23, respectively. To align two 25 μm diameter SPADs in the x-y plane, the following procedure was implemented: The telescope comprises six planes of pixels with a $250 \times 50 \mu\text{m}^2$ pitch. Initially, the upstream SPAD was employed as a trigger for an arbitrary plane. When the beam traversed the SPAD and the telescope, the most illuminated pixel of the telescope indicated the SPAD's position relative to the telescope. Subsequently, the downstream SPAD was aligned with the same pixel on the identical telescope plane, utilizing the downstream SPAD itself as a trigger. At this stage, it was established that the two SPADs were situated within a $250 \times 50 \mu\text{m}^2$ area. The downstream SPAD was then gradually adjusted in the x-y plane using 1 to 5 μm steps until both SPADs exhibited a maximum coincidence rate under the beam.

To prevent stray light interference, the SPADs are coated with black paint. Pions with a momentum of 120 GeV/c were employed as minimum ionizing particles (MIP) at the CERN T4-H6 beamline. As pions pass through a SPAD, the process of ionization generates a track of ions and free electrons. Consequently, an avalanche signal is triggered. By detecting the coincidence of signals from the two SPADs, illustrated in Fig.4.24, the direct detection of pions can be performed.

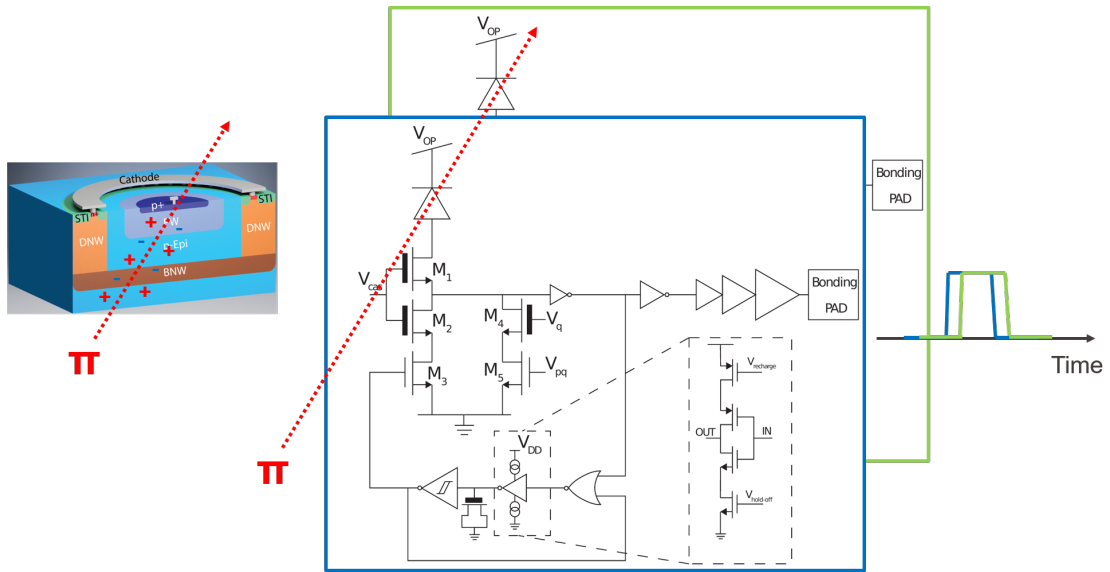
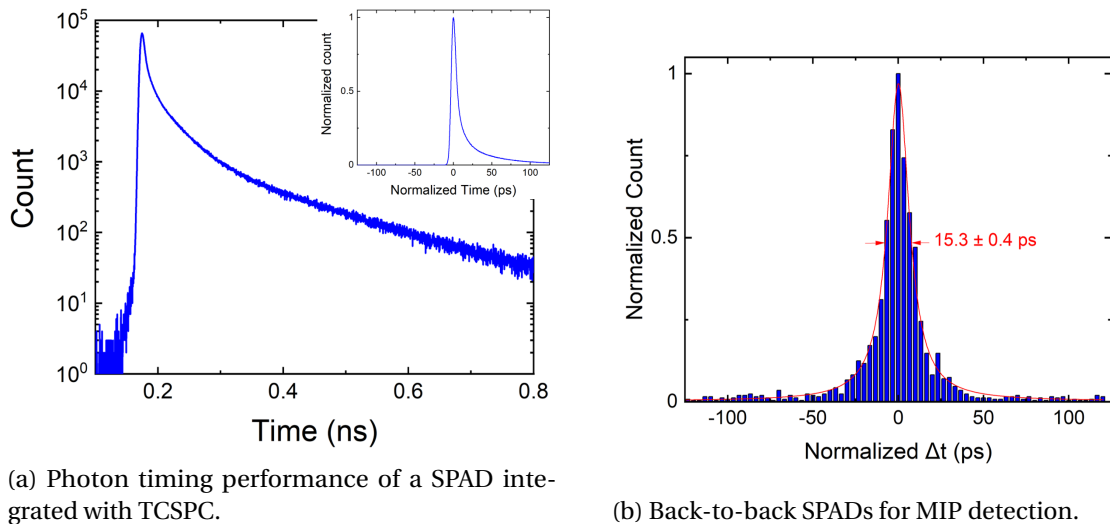


Figure 4.24: Schematic of the particle detection setup [68]

The timing histogram result is obtained by the measurement of the particles' time-of-flight between two adjacent SPADs. A standard SPAD's timing response usually exhibits a primary peak characterized by a Gaussian distribution along with an accompanying exponential tail [182]–[184]. This behavior is illustrated in the sample presented in Fig.4.25a. Consequently, the resultant histogram shape in a particle detection setup employing two SPADs is a convolution of two timing responses.



(a) Photon timing performance of a SPAD integrated with TCSPC.

(b) Back-to-back SPADs for MIP detection.

Figure 4.25: Timing response of SPAD for photon and MIP. The SPADs were biased at 27 V.

As presented in Fig.4.25a, it was demonstrated that an operational voltage of 27 V enables us to achieve a $FWHM_{single}$ of 8.7 ps for photon detection. The same voltage setting also facilitated the highest timing precision for MIP detection using two SPADs. Fig.4.25b displays

Chapter 4: Results of SPAD-based applications

the distribution of time-of-flight between two SPADs under 27 V. To evaluate the FWHM, we employed a Lorentz distribution with $R^2 = 0.99$. The calculated FWHM for MIP timing at 27 V was determined to be 15.3 ± 0.4 ps. It's important to highlight that these outcomes were directly extracted from the timing instruments, and no timewalk correction was needed due to the digital output of the SPADs.

The timing performance depends on the physical location of the starting point of the avalanche for particle detection, similarly as in photon detection. If the avalanche is initiated within the high-field region, the resultant time-stamp will be closer to the center of the histogram, where Gaussian statistics dominates. Conversely, if the avalanche starts subsequent to a free carrier's diffusion to the high-field region from the diffusion area, the time-stamp will be situated within the tail of the timing distribution. Adjusting the operational voltage, either by increasing or decreasing it, induces changes in the electric field distribution within the p-i-n structure. This phenomenon is illustrated in Chapter 1, Fig.1.2b.

Enhancing the extent and uniformity of the high-field region yields improved timing performance. As depicted in Fig.4.26, we present the FWHM and full-width-at-tenth-maximum (FWTM) timing resolution at varying operational voltages. A pattern is noticeable wherein the jitter performance for particle tracking mirrors the inverse of the average breakdown probability across the active region interval, along with the photon timing responses.

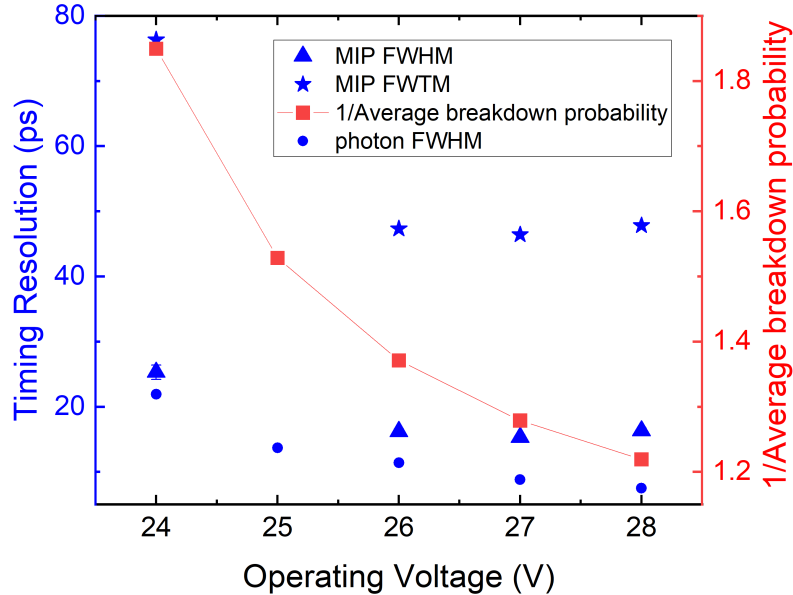


Figure 4.26: MIP and photon timing resolution and the inverse of the average breakdown probability within the active region at different operating voltages

Following pion exposure, a noticeable rise in the DCR of the detectors was observed. As depicted in Fig.4.27, a one-order magnitude escalation in DCR occurred within a week of

pion exposure. Despite subsequent room temperature annealing for another week, the DCR sustained its elevated level. This suggests that the SPADs' deterioration is not solely attributed to ionization, but also to displacement damage. This unexpected phenomenon arises from the fact that pions, though predominantly inducing ionization, may generate secondary particles like protons upstream of the pion beamline, contributing to the increase in DCR.

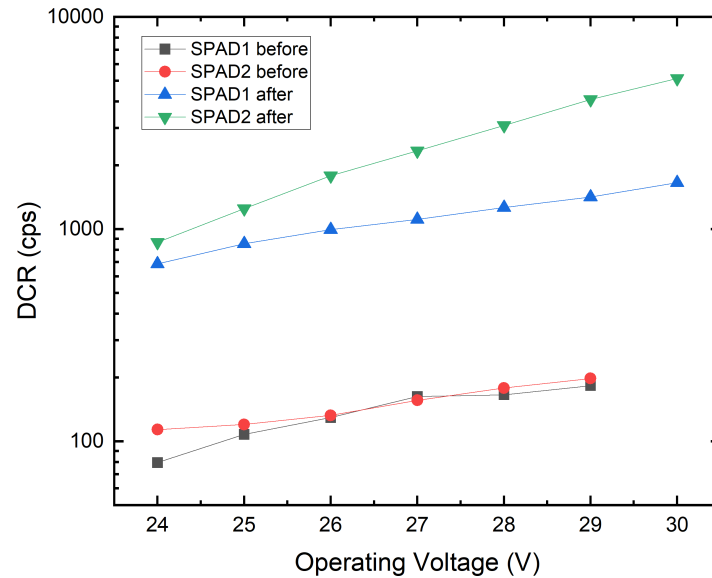


Figure 4.27: DCR of the two SPADs before and after operating on the beamline

Discussion

Opting for a larger detector proves advantageous in particle tracking and radiation sensing. However, the trade-off is a higher base DCR in larger SPAD or detection areas. This noise factor can be mitigated by employing additional AND logic for collecting coincidence signals, as demonstrated in a previous study [61]. This entails defining a coincidence resolution time window. In this scenario, a coincidence dark count only occurs if both SPADs exhibit dark counts simultaneously within the established window. A simulation, assuming dark count generation follows the Poisson process and both SPADs share the same DCR, yielded results as displayed in Fig.4.28. For a resolution time window of 0.5 ns, the coincidence DCR is 14 μ Hz when both SPADs have a DCR of 100 cps, a situation corresponding to the start of our beamline measurement. This equates to just 1 count of noise in a 24-hour measurement. Toward the conclusion of the beamtime, with the DCR escalated to around 1 kcps, the coincidence DCR amplified to 1.1 mHz, corresponding to 95 counts of dark count within 24 hours.

Cooling can also be employed when utilizing larger SPADs. Illustrated in Fig.4.29, the DCR of a 100 μ m diameter SPAD was evaluated under an operating voltage of 27 V. Notably, at room

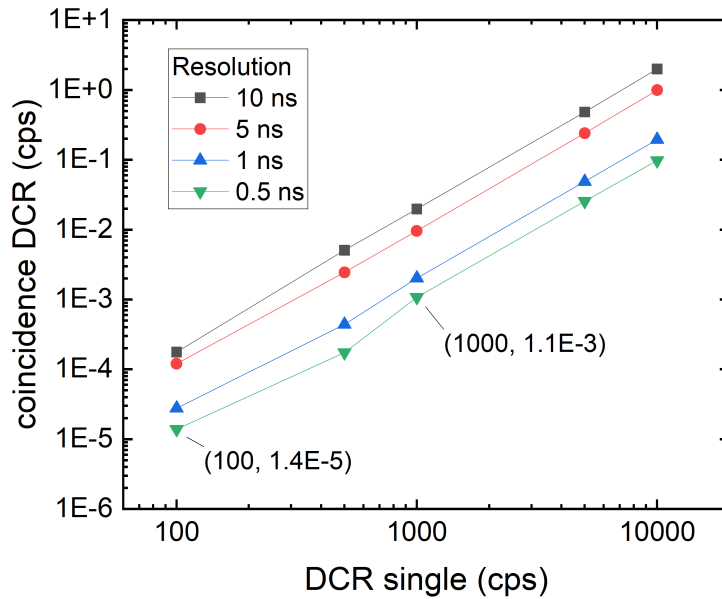


Figure 4.28: Simulation results of the coincidence DCR are shown for various coincidence resolution time windows and single SPAD DCR levels. The annotations mark the DCR level before and after exposure.

temperature, the DCR of the 100 μm SPAD exceeds that of the 25 μm SPAD by two orders of magnitude. Nevertheless, when cooled to -50°C , it can be operated while maintaining the same noise level.

When aiming for scalability, achieving a more compact system becomes imperative. In our scenario, the elimination of the timing oscilloscope is essential. To assess this, we conducted additional experiments utilizing a TCSPC module (BH SPC-150-NXX). Remarkably, this setup allowed us to achieve an FWHM as low as 8.7 ps for a single SPAD, as demonstrated in Fig.4.25a, with consistent performance regardless of count rate, up to 1.1 MHz [185].

Three notable examples of detectors renowned for their high timing resolution, employed for MIP detection, include the PicoAD, a multi-PN junction monolithic silicon detector [178], [181]; Ultra-Fast Silicon Detectors (UFSD), which are based on Low-Gain Avalanche Detectors (LGAD) [186]; and TIMESPOT, utilizing 3D silicon sensors [187]. All these detectors exhibit a Gaussian timing profile. A comparison of the optimal timing outcomes can be found in Table 4.2. Concerning MIP detection efficiency, SPADs are anticipated to surpass an efficiency exceeding 99% above the breakdown threshold [188], akin to the other two detectors. It's noteworthy that all the aforementioned detectors necessitate time-walk correction and pre-amplification.

One example of a particle discriminator is the time-of-flight detector, which is capable of

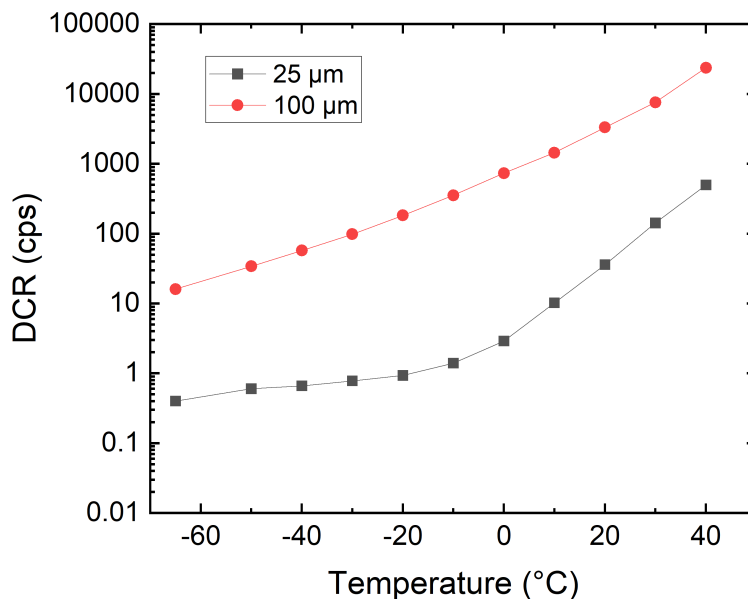


Figure 4.29: DCR of the 25 μm and 100 μm SPADs at different operating temperature. Both SPADs were biased at 27 V.

Table 4.2: Comparison of the performance presented with state-of-the-art systems

Detectors	Resolution best (ps)	Timewalk	Efficiency
PicoAD	$\sigma = 17.3$	yes	> 99%
UFSD	$\sigma = 16^a$	yes	> 99%
TIMESPOT	$\sigma = 11.5$	yes	~ 99%
This work	FWHM = 15.3	no	> 99%

^a 3 UFSD $V_{\text{bias}} = 230$ V

distinguishing elementary particles of the same momentum based on their time of flight between two detectors, typically using scintillators. In this context, we examine the minimum timing performance required when considering the use of SPADs as direct detection time-of-flight detectors. The two particles, characterized by different masses m_1 and m_2 , possess respective velocities v_1 and v_2 . The time-of-flight difference between two relativistic particles traveling between two detectors separated by a distance L can be expressed as follows:

$$\Delta t = L \left(\frac{1}{v_1} - \frac{1}{v_2} \right) \simeq \frac{Lc}{2p^2} (m_1^2 - m_2^2), \quad (4.19)$$

where p is the particle momentum. Consider a typical pair of particles that need differentiation: kaon ($m_k \sim 500 \text{ MeV}/c^2$) and pion ($m_\pi \sim 140 \text{ MeV}/c^2$). Assuming a momentum of $1 \text{ GeV}/c$ and $L = 10 \text{ m}$, a timing resolution of $\Delta t = 3 \text{ ns}$ is sufficient to distinguish these particles in this scenario. However, if the particle momentum increases to $10 \text{ GeV}/c$, the timing resolution

must be lowered to 30 ps. This requirement arises because the time-of-flight difference scales with the inverse square of the momentum. This calculation emphasizes the significance of enhancing the timing resolution of particle detectors.

4.5 Conclusion

We have demonstrated several applications that can be implemented in a challenging environment and the affect of such environment on the performance of each applications.

In the context of 2D intensity imaging, we have established a significant relationship between several key factors: SNR, dynamic range, DCR, frame rate, exposure time, and the bit depth of a clocked SPAD camera. The findings suggest that an elevation in DCR could potentially undermine the SNR and dynamic range, particularly when the combination of bit depth and frame rate falls short. Notably, our study underscores the superiority of SPAD-based cameras over conventional cameras by achieving dynamic ranges exceeding 100 dB. This superiority can be realized either through the interplay of high bit depth and frame rate or by adopting a mixed exposure approach.

In the realm of 3D imaging, alongside multi-object ranging for depth information acquisition (x,y,z), the incorporation of a SPAD camera also permits the capture of the temporal dimension (x,y,t). We have successfully demonstrated the largest-to-date wide-field FLIM application with a gated SPAD array designed for biologically relevant samples. Utilizing the adaptability to modify gate shift sizes during camera exposures, we have substantiated the viability of rapid acquisition speeds of up to 1 Hz. Employing a spatial mosaic acquisition strategy, we have achieved the creation of 3.64-megapixel FLIM images. This method holds the potential for further expansion, encompassing even larger FOVs and shortened acquisition times through the integration of specialized and efficient translation stages. Furthermore, the implementation of artificial neural networks has enabled the achievement of a four orders of magnitude improvement in lifetime fitting speed compared to conventional least square fitting methods.

In the domain of spectral applications, where a 1D sensor array is typically employed, we ventured to use a 2D SPAD array to showcase hyperspectral FLIM, enabling the collection of 4D information encompassing spatial coordinates, lifetime, and wavelength (x, y, t, λ). Furthermore, we successfully demonstrated 4D light-in-flight imaging. This achievement within high-speed imaging serves as a testament to the potential integration of large-format SPAD arrays in astronomical observation and imaging, as well as in various sophisticated imaging realms such as non-line-of-sight imaging [189]–[195]. The devised reconstruction technique showcases its capability to trace the path of emitted and reflected light, thereby providing depth and time information.

Finally, we successfully demonstrated timing jitter performance at the 10-ps FWHM level for direct MIP detection using SPADs. The inherent avalanche process of SPADs eliminates the need for timewalk correction or post-processing to achieve such high timing resolution. Our

investigation encompassed the influence of the operating voltage on timing performance. Our findings indicated that the jitter profile closely resembled that observed in SPADs employed for photon detection, implying that the electric field profile significantly affects the timing performance of MIP detection. Following exposure, we observed an increase in DCR, yet the noise remained negligible due to the nature of coincidence detection. These results pave the way for the potential design of future high-precision particle tracking systems utilizing SPAD-based technology.

5 Conclusion

In this section, we offer a summary of the goals of this thesis and our contributions to the field. We aim to include an overview of the state-of-the-art in SPAD technology and assess its suitability for space and radiation environments, as well as other relevant applications. We also undertake a technology comparison with existing systems that employ optical sensors other than SPADs to evaluate the feasibility and potential advantages of transitioning to SPAD-based systems for improved performance.

5.1 Summary

The objectives of this thesis include studying the effects of harsh environments, including radiation damage, extreme lighting conditions, and temperature fluctuations, on the performance metrics of SPAD-based systems. We also aim to investigate strategies for mitigating these effects. Additionally, we aim to assess how these environmental factors impact performance across various applications. Furthermore, we endeavor to demonstrate the applicability of SPAD-based systems in these scenarios, showcasing their state-of-the-art performance as a proof of concept for SPAD-based systems to replace conventional image sensors in various applications.

To achieve these objectives, in Chapter 2, we discussed the development of SPAD-based system functions and methods to utilize such systems as tools for studying harsh environmental effects and for various applications. We emphasized the concept of gating, which is crucial for enabling the effective use of large-scale SPAD arrays across a wide range of applications.

In Chapter 3, we studied the effects of protons and neutrons on various SPAD-based systems. We thoroughly examined the figures of merit of SPADs and demonstrated that radiation damage plays a crucial role in noise performance, particularly in the form of afterpulses.

We employed the methods and findings from the two preceding chapters to assess their impact on various applications, as discussed in Chapter 4. These case studies offer relevance to space-based applications to varying degrees.

5.2 Scientific contribution

In this section, we provide a summary of the scientific contributions made in this thesis. Our work began by focusing on space-based applications, which formed the basis for structuring our study. This involved identifying anticipated challenges, creating predictive models, designing experiments, and subsequently analyzing data from a variety of experiments. The primary scientific contributions of this thesis can be summarized as follows:

- Comprehensive study of the impact of proton and neutron radiation on SPAD-based systems, along with the exploration of effective mitigation strategies.
- Theoretical derivation and experimental confirmation of the signal-to-noise ratio and dynamic range limits for clock-driven SPAD cameras.
- Practical demonstrations of advanced imaging techniques, including object ranging, fast fluorescence lifetime imaging, hyperspectral fluorescence lifetime imaging empowered by machine learning, and the novel concept of 4-dimensional light-in-flight imaging.
- Demonstration of the state-of-the-art capabilities of SPAD-based sensors for radiation and particle detection, highlighting their potential in harsh radiation environments.

In Chapter 2, the megapixel SPAD camera was designed by Kazuhiro Morimoto (KM), and firmware development for gating mode and binary intensity mode was undertaken by KM and Ming-Lo Wu (MW), under the supervision of Edoardo Charbon (EC). In Chapter 3, the DUTs consisted of SPADs designed by Ekin Kizilkan, Francesco Gramuglia (FG), Pouyan Keshavarzian, and KM. The experiment's concept was developed by MW and EC, executed by MW and Emanuele Ripiccini (ER), and analyzed by MW. In Chapter 4, MW derived the theoretical dynamic range limit for 2D intensity imaging. The theory was experimentally confirmed by MW and KM. KM and MW conceived the 3D object ranging experiment. The fluorescence lifetime imaging microscopy work was conceptualized by EC and Daniele Faccio, while the experiment was conducted by MW and Vytautas Zickus (VZ), and results were analyzed by MW, VZ, Valentin Kapitany, Areeba Fatima, and Alex Turpin. The 4D hyperspectral fluorescence lifetime imaging was conceptualized by EC, with the experiment and analysis carried out by Mingsong Wu and MW. The 4D light-in-flight reconstruction was conceived by KM and MW, and the experiment was conducted and analyzed by KM, MW, and Andrei Ardelean. The pion detection experiment was conducted by MW, ER, and Jad Benserhir, with the chip designed by FG, and the results were analyzed by MW and ER. All studies were performed under the guidance of EC.

To conclude, this work highlights the significant potential of SPAD-based technology, showcasing its adaptability in high-radiation environments and its broad applicability across scientific domains. Incorporating SPAD-based systems in these applications enhances performance standards. In the next section, we undertake a comparative analysis of SPAD-based systems against conventional sensors to demonstrate the feasibility of their replacement.

5.3 Technology comparison

In various applications, whether they involve photon counting or imaging, the choice of the system requires either a single-pixel photodetector or an array as an image sensor. We differentiate between these two types of modules and compare SPADs to existing systems.

For single-pixel photodetectors, we compare SPADs to silicon photomultipliers (SiPMs), also known as Multi-Pixel Photon Counters (MPPCs) in Hamamatsu, for silicon-based detectors. SiPM is a single-output detector that combines SPADs in parallel. We also make comparisons with Photomultiplier Tube (PMT) technology, developed in the 1930s and utilizing dynodes to multiply primary electrons generated by a photocathode within a vacuum tube. This technology is still widely used for its well-established reliability. Lastly, we include Avalanche Photodiodes (APDs), which are photodiodes operating in linear gain or proportional mode. The comparison of the typical performance measures of these detectors is presented in Table 5.1.

Table 5.1: Comparison of single photodetectors

	SPAD	SiPM(MPPC)	PMT	APD
Scalability	High	High	Low	Low
Detector Area	μm^2	mm^2	mm^2	mm^2
Dynamic range	Low	High	High	High
Timing Precision	High	Low	Low	Low
Peak efficiency(%)	> 40	> 40	~ 30	> 40
Noise performance:				
Dark count/current	< 0.1 cps/ μm^2	< 0.1 cps/ μm^2	< 100 cps, < 1 nA	< 1 nA
Read-out noise	no	yes	yes	yes
Excess noise	no	no	yes	yes
afterpulsing(%)	< 0.1	$\gg 1$	$\gg 1$	< 0.1

SPAD-based technologies offer high scalability due to their CMOS compatibility, as demonstrated in recent large-format array works. In contrast, PMTs are strictly limited by vacuum tubes, which cannot be miniaturized beyond a certain point and which do not operate in strong magnetic fields. While APDs are CMOS compatible, they operate in a linear gain regime, where small fluctuations within an array can cause significant variations in gain, leading to high nonuniformity within the array. This limitation restricts their scalability.

SPADs have a disadvantage in terms of detector area dimension because they exhibit dark counts that scale with the area. A larger area directly influences the probability of dark counts. Typically, SPADs have active areas in the order of tens to thousands of μm^2 . In contrast, SiPMs, PMTs, and APDs rely on the integration of current signals originating from carrier multiplication.

The current integration mechanism also influences the dynamic ranges of these detectors, as a higher photon flux can be translated into higher current. However, SPADs are limited

by their small detection area and by deadtime or count rate in high photon flux conditions. On the other hand, SPADs' Geiger mode operation and instant digital response allow them to be integrated with timing instruments for high-timing precision applications, which is not available in other detectors.

In terms of peak efficiency, this highly depends on the detector design, as described in Chapter 1. Silicon-based sensors can typically achieve peak efficiency above 40% at various wavelengths by design. PMTs use a photoelectric-effect cathode, which typically exhibits lower efficiency compared to other detectors.

The noise performance of these detectors is quantified by either dark counts or dark current. Due to their smaller detector size, SPADs generally exhibit lower noise levels. The noise per unit area can be expected to be similar to SiPMs. PMTs and APDs typically have dark currents below 1 nA. SPADs excel in terms of other noise sources such as read-out noise and excess noise. Read-out noise arises during the analog-to-digital conversion process, while excess noise results from uncertainties in the multiplication process. Since SPADs operate in Geiger mode with infinite gain, and their read-out is digital, SPADs do not suffer from these noise factors. In contrast, SiPMs may experience read-out noise during current-to-count conversion, and the other two detectors exhibit both noise sources. Finally, undamaged SPADs and APDs typically exhibit afterpulsing probabilities lower than 0.1%. MPPCs demonstrate a higher afterpulsing probability compared to SPADs, as SPADs output in parallel. The afterpulsing observed in PMTs has been identified as originating from either the ionization of gaseous impurities within the tube by the accelerated photoelectrons [196], [197] or from back-scattered electrons at the PMT dynodes returning to the first dynode.

As previously mentioned, SPADs have limitations when it comes to their dynamic range under high photon flux conditions. To address this challenge, it is common to employ arrays of SPADs. This approach leverages the scalability of SPAD arrays, effectively extending and enhancing the dynamic range of detection.

An array of SPADs also allows imaging applications. Prior to SPAD-based arrays, the imaging sensor market was dominated by CCD and CMOS cameras. We compare the developed SPAD camera to existing cameras, especially those designed for low-signal imaging. This includes electron-multiplying CCD (EMCCD), which integrates electron-multiplying structures into CCDs, intensified CCD (ICCD), which leverages optical amplification from image intensifiers, and CMOS cameras that utilize photodiodes as optical detectors. This encompasses scientific CMOS (sCMOS) camera and two-tap CMOS camera designed for various research applications. The comparison of the typical performances of these image sensors is presented in Table 5.2.

The table compares existing cameras with more than 1-megapixel resolution. Due to the limited size of the sensor chip, pixel sizes are scaled down to the range of tens to hundreds of μm^2 for all the cameras. The low fill factor of SPAD arrays (typically on the order of 10%) results in a relatively low detection efficiency compared to other types of image sensors. This is attributed to the per-pixel readout electronics that occupy the area of a single pixel. This

Table 5.2: Comparison of array/image sensors (≥ 1 Megapixel)

	SPAD	EMCCD	ICCD	sCMOS	Two-Tap CMOS
Pixel size	μm^2	μm^2	μm^2	μm^2	μm^2
Peak efficiency(%)	> 40	> 90	> 50	> 50	> 30
Frame Rate	~ 25000	< 100	< 10	< 100	< 100
Minimum Exposure	< 10 ns	> 10 ms	< 2 ns	< 2 ns	> 10 ms
Gating resolution	< 20 ps	> 1 ns	10 ps	10 ps	> 1 ns
Dynamic Range (dB)	> 100	~ 100	> 80	> 80	> 60
Noise performance:					
Read-out noise	no	yes	yes	yes	yes
Excess noise	no	yes	yes	no	no

issue can be mitigated by applying microlenses or opting for 3D chip integration.

On the other hand, the per-pixel readout architecture and binary response of SPADs allow for much higher frame rates compared to other cameras in which photons are accumulated in the form of photoelectrons, limited by the full well capacity. The close proximity of readout electronics also allows for low exposure times or shutter speeds down to the nanosecond range, while only ICCD and sCMOS cameras can achieve such speeds by utilizing optical gating. Moreover, this enables gating resolution down to tens of picoseconds for these cameras.

In terms of dynamic range, CCD and CMOS cameras are limited by the full well capacity and the readout noise. Dynamic range is typically defined as the full well capacity divided by the minimum readout noise. As demonstrated in Chapter 4, SPAD-based cameras can achieve a dynamic range of higher than 100 dB by acquiring high bit-depth images and using a mixed exposure scheme. Additionally, the absence of read-out noise and excess noise in SPAD-based image sensors extends their dynamic range in low-light conditions while CMOS cameras suffer from read-out noise and CCD cameras suffer from both noise sources.

Other single-photon detectors, such as Superconducting Nanowire Single-Photon Detectors and Transition-Edge Sensors, have been omitted from the comparison due to their need for cryogenic operating conditions. However, it's worth noting that SPAD-based sensors can achieve performance levels similar to these cryogenic detectors [198]–[200]. Therefore, we have focused our comparison on room-temperature operational detectors.

With this comparison, we can conclude that single-pixel SPAD detectors exhibit superior performance in terms of timing and low signal detection, thanks to their Geiger mode operation and zero read-out noise. In the realm of image sensors, SPAD-based technology enables high frame rates with a wide dynamic range, making them the most suitable detectors for low signal and ultra-fast phenomena.

5.4 Future perspective

In the context of developing optical imaging SPAD-based sensors capable of withstanding high radiation doses, the size of the SPAD's active area emerges as a crucial factor. Incorporating microlenses presents a viable strategy to enhance the effective active area while maintaining a compact SPAD structure, thereby minimizing susceptibility to radiation-induced damage. Recent literature also investigates the radiation hardness of microlenses and color filters [201], adding valuable insights to this approach. Within the domain of radiation sensing, the implementation of 3D-integrated, back-to-back large-area SPADs, complete with active recharge circuitry and coincidence detection, provides an effective solution for achieving precise timing responses while simultaneously mitigating the inherent noise levels associated with a larger active area. This approach successfully addresses the challenge of balancing active area size and radiation resilience in SPAD-based radiation sensors. Moreover, both applications can benefit from a well-controlled cooling system, such as a Peltier cooling system, to further enhance performance and stability.

We have demonstrated the use of machine learning for efficient data analysis with SPADs, but this field offers many untapped opportunities for faster and more advanced data processing. In the coming years, we expect an increased application of machine learning, especially in FLIM and related scientific imaging, to further enhance performance [202]. Additionally, newer techniques like recurrent neural networks and spiking neural networks are being explored for real-time bio-science imaging [203], [204], promising significant improvements in SPAD-based sensor data analysis. Future research should focus on harnessing these methods to advance SPAD-based sensor capabilities.

Finally, we would like to emphasize the potential of implementing SPAD-based systems in space-based applications, particularly in planetary exploration. Image sensors are currently employed in various remote material studies, such as Laser-Induced Breakdown Spectroscopy and Raman spectroscopy, which require sensors with good sensitivity under low signal and high radiation environments. SPAD sensors also hold promise for space-based quantum communication applications, offering enhanced capabilities in secure communication over long distances and high count rate contributing to the development of secure data transmission in free space. Our future work will focus on promoting the adoption of SPAD-based sensors in these related applications to achieve better performance and stimulate further research and development in this exciting and rapidly evolving field.

A SPAD characterization methods

This chapter provides a comprehensive analysis of the characterization of the figures-of-merit of SPADs. It also discusses how different measurement methods can potentially affect the results and therefore need to be carefully considered.

A.1 Dark count

The dark count rate characterizes the global noise performance of a SPAD when no external signal is presented. Unlike a photodiode in which the noise is characterized as a continuous dark current, SPADs express noise as quantized counts due to the avalanche event and the quenching mechanism provided by either a resistor or a transistor. This allows us to digitize the voltage pulse with a discriminator such as an inverter or a comparator. The count can then be recorded by a counter.

To comprehend the potential variations in the results of a Dark Count Rate (DCR) measurement across different setups, it is necessary to first grasp the voltage pulse shape at the anode of a SPAD. A SPAD can be represented as a combination of components including a junction capacitance (C_J , typically a few pF), a junction resistance (R_J , typically in the range of hundreds of Ω), and a switch symbolizing photon incidence [205]. This is depicted in Fig.A.1a. Normally, the capacitor is charged by V_{OP} . Upon the arrival of a photon, the switch closes and the capacitor discharges with a time constant of $R_J C_J$, leading to a rise time of less than 1 ns. The resultant maximum voltage at the anode becomes $V_{OP} - V_B$. During the recharge phase, the switch opens, resulting in a voltage drop at the anode with a time constant that could extend up to a few hundred ns. This is due to the passive quenching resistance typically being higher than 100k Ω .

An example of the voltage output at the anode can be observed in Fig.A.1b. In general, the most efficient method for counting the number of pulses is to connect the anode to a counter. This counter discriminates the output using a threshold V_{T1} . However, in specific cases like this example, the counter might inaccurately miss counting the third pulse, which could

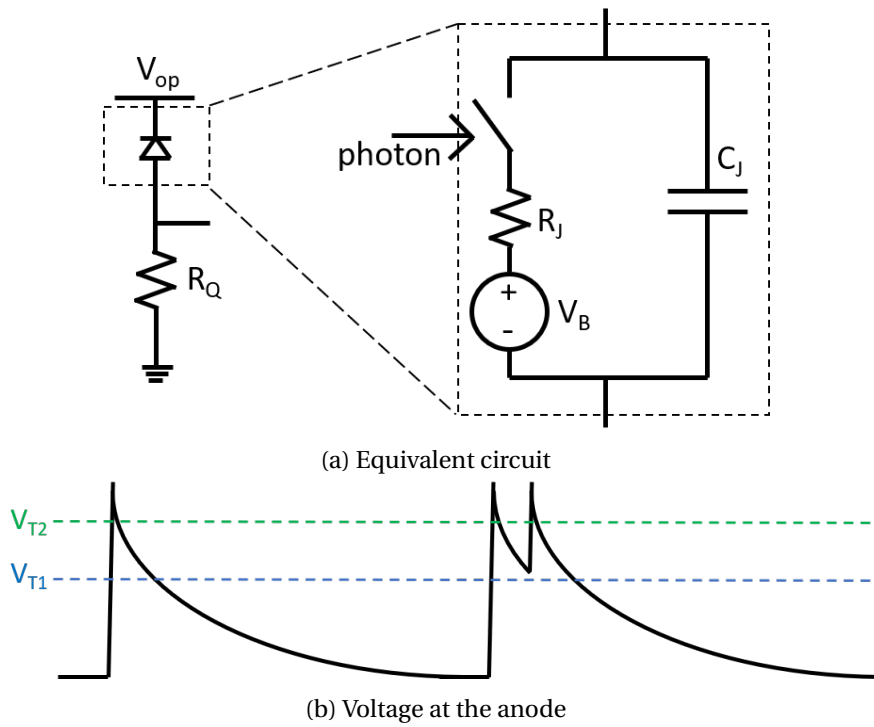


Figure A.1: (a) shows the equivalent circuit of a passive quenching SPAD includes a junction resistance R_J and a junction capacitance C_J . (a) indicates how the discriminator threshold can affect measurement result.

potentially be either an afterpulse or a dark count occurring during recharge. In such cases, a higher threshold V_{T2} is used to capture all the dark counts. Therefore, it is recommended to monitor the pulses with an oscilloscope before using a counter.

Because of this consideration, we characterize the DCR of irradiated SPADs using a comparator at the anode with a threshold set at 80% of V_{ex} . Typically, in a SPAD-based system, employing the high-precision SPAD as an example [68], an inverter serves as the discriminator. In this setup, the threshold is set at half of the logic voltage supply, which acts as a form of screening for afterpulsing.

To characterize the DCR with respect to temperature, the DUTs are placed in a temperature chamber. It should be noted that at lower temperatures, free carriers have a lower probability of colliding with the lattice. Consequently, they require a lower electric field to build up enough momentum to trigger an avalanche. Therefore, as the temperature decreases, the breakdown voltage also decreases. Consequently, it is necessary to lower the biasing voltage to maintain a reasonable V_{ex} at different temperatures to avoid damaging the front-end circuitry. The relationship between V_b and temperature is first characterized by measuring the output count of the DUT under different V_{op} and temperatures under moderate illumination. An example can be seen in Fig.A.2a, where the legend marks the operating temperatures. The breakdown voltage at different temperatures can then be extracted by finding the intercept on the voltage

axis. The relationship between breakdown voltage and operating temperature can then be determined by the slope of Fig.A.2b. This value is typically around 0.02 to 0.03 V per degree Celsius.

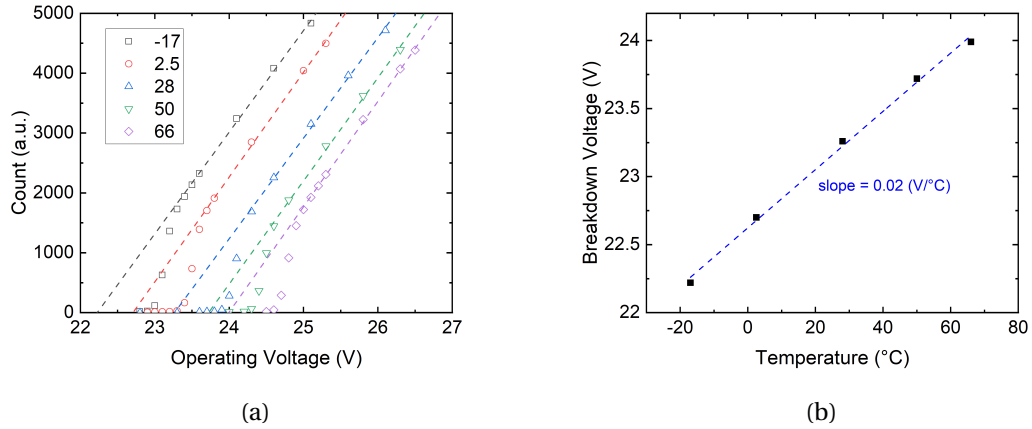


Figure A.2: (a) shows the output counts at different operating voltages and different temperatures. (b) shows the extracted temperature dependence of the breakdown voltage

A.2 Afterpulsing

In this section, we will discuss a popular method for measuring afterpulsing probability based on interarrival time measurements [81]. The method involves collecting timestamps of pulses generated by a free-running SPAD at a specific threshold level. This is typically accomplished using a fast oscilloscope with precise timing capabilities. The interarrival times between all consecutive pulses are then recorded in a histogram. It's important to note that the choice of threshold level can affect both the timing and the number of recorded counts, as illustrated in Fig.A.1b. Therefore, when dealing with noisy or highly afterpulsing SPADs, it is advisable to use a higher timestamping threshold to obtain reliable measurements.

This method takes advantage of the nature of Poisson statistics by distinguishing between the primary dark counts, which are fitted exponentially on the histogram, and the afterpulses, which appear above the exponential fit. Examples of measurements using this method are presented in Chapter 3, specifically in Fig.3.9 and Fig.3.19.

Achieving accurate results with this method requires the accumulation of pulses for improved statistical significance. Consequently, for a SPAD with a low DCR, longer acquisition times are often necessary to build up the histogram. In such cases, it is suggested that dim illumination can be applied to expedite the measurement process, as illumination also results in an exponential decay in the interarrival time histogram.

It has been discussed that applying dim illumination can influence the measured afterpulsing probability [81]. To demonstrate the impact of illumination on the extracted afterpulsing

probability using exponential fitting, we present a measurement result for a SPAD with a DCR of 100 cps, showing the effect of increasing illumination in Fig.A.3. Due to the low signal rate, each measurement required over 48 hours to ensure statistical accuracy. The results reveal a rapid decrease in the apparent afterpulsing probability as illumination is applied.

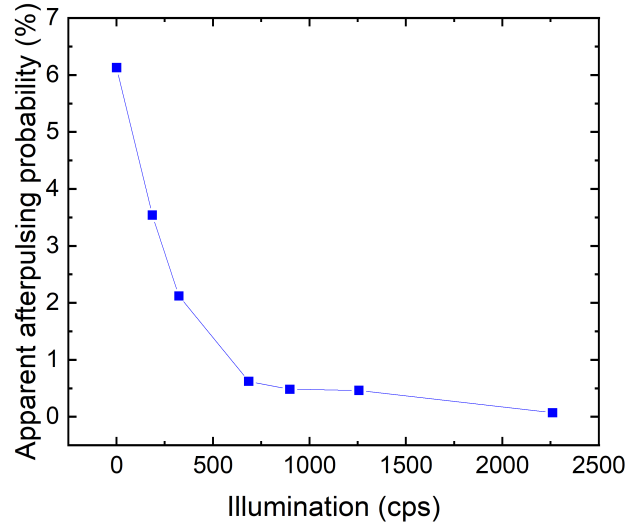


Figure A.3: The relationship between the apparent afterpulsing probability and the level of illumination.

Due to the dependence of this signal on the apparent afterpulsing probability, we conducted measurements of the afterpulsing probability after irradiation in complete darkness. This approach enables us to capture the worst-case scenario. Moreover, this behavior suggests that a SPAD implemented in a high count rate application may be less susceptible to the effects of afterpulses.

A.3 Photon detection probability

To measure the PDP (Photon Detection Probability) as presented in this work, we employed a method that is also applicable to other detectors, such as multi-pixel photon counters or silicon photomultipliers [206]. The experimental setup is depicted in Fig.A.4. We utilized a Xenon lamp as a continuous light source, emitting a broad spectrum of light ranging from 200 nm to 2000 nm. Subsequently, this white light passed through a computer-controlled monochromator capable of filtering out light with a narrow bandwidth, as low as 1 nm. An aperture situated at the monochromator allowed us to tune the intensity of the output single-wavelength light.

The light was then directed into a light-tight chamber housing an integrating sphere and the DUT. The integrating sphere efficiently diffused the input light across its entire inner surface

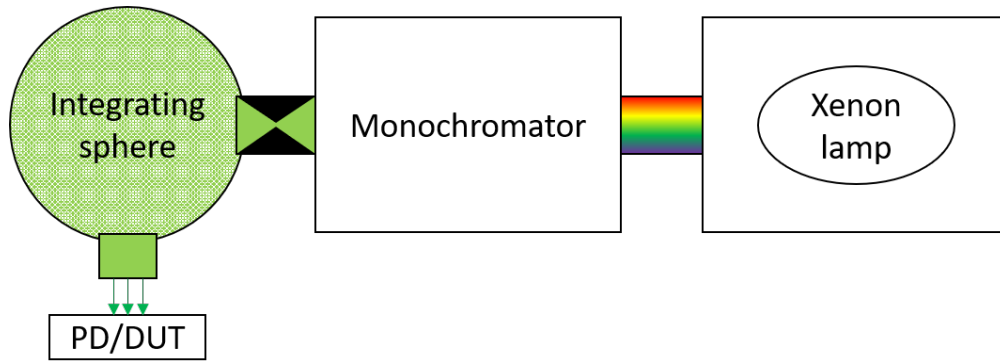


Figure A.4: PDP measurement setup

through multiple reflections. We typically position the commercial reference photodiode, denoted as PD, more than 10 cm away from the output of the integrating sphere. This is to ensure that only light perpendicular to the sensors is impinging. This photodiode enabled us to characterize the actual output light intensity at each wavelength by scanning through the wavelength range using the monochromator. Since we knew the photoresponse of the photodiode expressed in Amperes per Watt, we could utilize the output current from the photodiode to create a mapping of the photon flux density at each wavelength, $\Phi(\lambda)$, using the equation:

$$\frac{\Phi(\lambda)}{A_{PD}} = \frac{P(\lambda)}{h\nu \cdot A_{PD}} \quad (\text{A.1})$$

where A_{PD} is the area of the photodiode, P is the measured optical power, h is Planck's constant, and ν is the photon frequency.

Following this characterization, we replaced the photodiode with the DUT in the same position. This allowed us to measure the counts at different wavelengths and biasing voltages, thereby assessing the DUT's response.

One has to note that the dark count of the SPAD and the dark current of the photodiode have to be subtracted when characterizing the SPAD response and the optical power. The afterpulsing probability of the SPAD should also be corrected since afterpulses generate extra signals when photons impinge. Without the correction, one can overestimate the PDP.

A.4 Timing jitter

As the avalanche process generates a large current within a short period, the timing response of SPADs is expected to be in the tens of picoseconds to hundreds of picoseconds range. To precisely characterize the timing jitter on this timescale, it is required to have a reference with sub-picosecond timing resolution to ensure the precision of the measurement. As a light source reference, we used a femtosecond laser that emits optical pulses with a duration well

Chapter A: SPAD characterization methods

below 1 ps. The laser pulse is then split by a beam splitter, with one branch going to a fast photodiode with picosecond-level rise time, and the other branch reaches the SPAD under test after passing through a neutral density (ND) filter.

The setup is depicted in Fig.A.5. The two signals coming from the reference photodiode and the SPAD are then sampled by a fast oscilloscope (WaveMaster 813Zi). The time interval between the two pulses is measured and forms a histogram, as shown in the previous chapters.

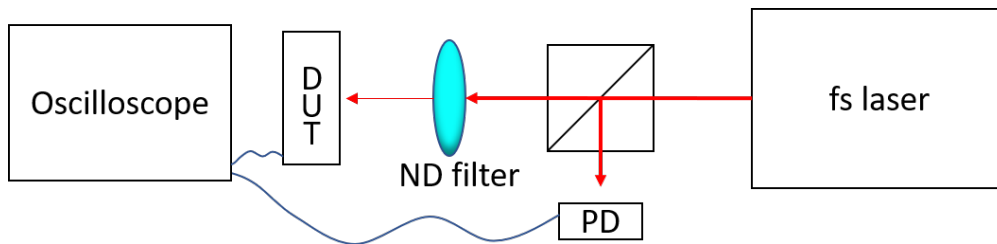


Figure A.5: Timing jitter measurement setup

The ND filter serves the crucial role of ensuring that only a single photon strikes the SPAD during each laser pulse, thus guaranteeing that the SPAD operates in the single-photon regime. Without this precaution, the intensity of the incoming signal could be so high that multiple photons simultaneously trigger the avalanche process. When this occurs, the avalanche initiated by the photon in the high-field region responds more rapidly than the one triggered in the diffusion region, where electron-hole pairs must first migrate to the high-field region to initiate an avalanche. Consequently, measuring timing jitter under strong light can result in an underestimation of timing precision, as the avalanche signal from the initial electron-triggered avalanche consistently masks subsequent avalanches.

As we approach 10 ps FWHM timing, often we observe multiple smaller peaks in the acquired histogram instead of one Gaussian center and an exponential tail as shown in Chapter 4 Fig.4.25a. This is attributed to the alignment of the setup. Notice that 1 ps corresponds to light traveling for 300 μm . Any reflection along the signal path or even reflection of the laser on the bonding wires can result in this artifact in the measurement. Therefore, alignment plays an important role in achieving such timing resolution.

B Gallery

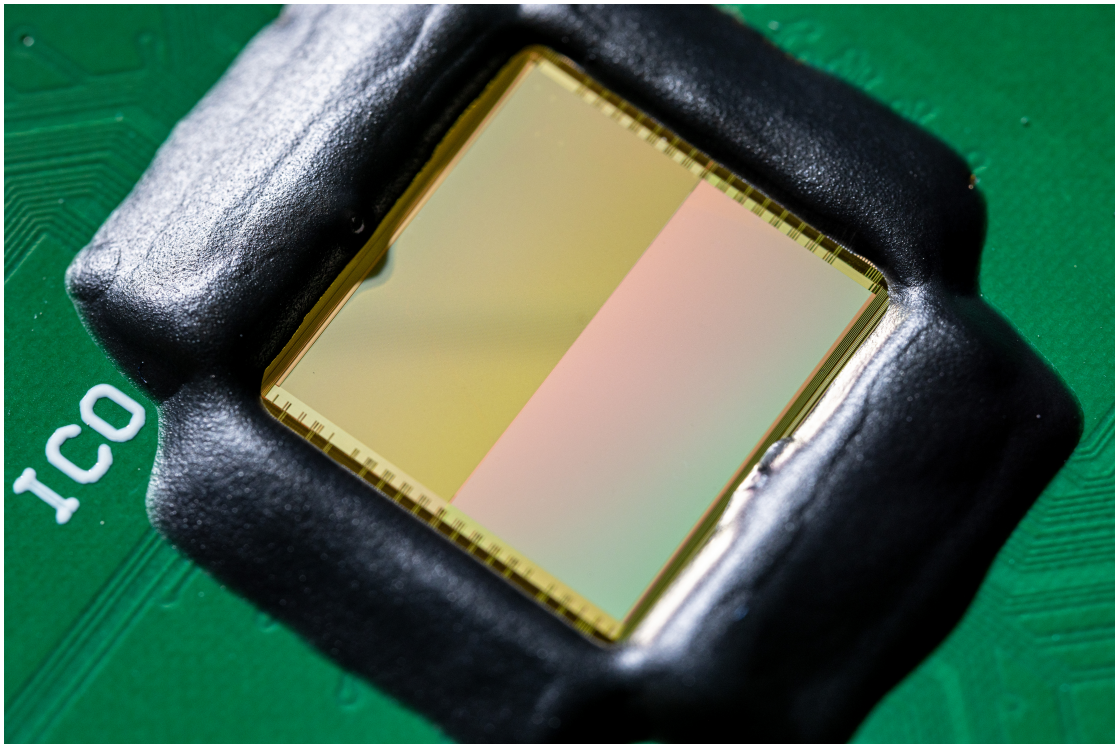


Figure B.1: Megapixel SPAD array [35]

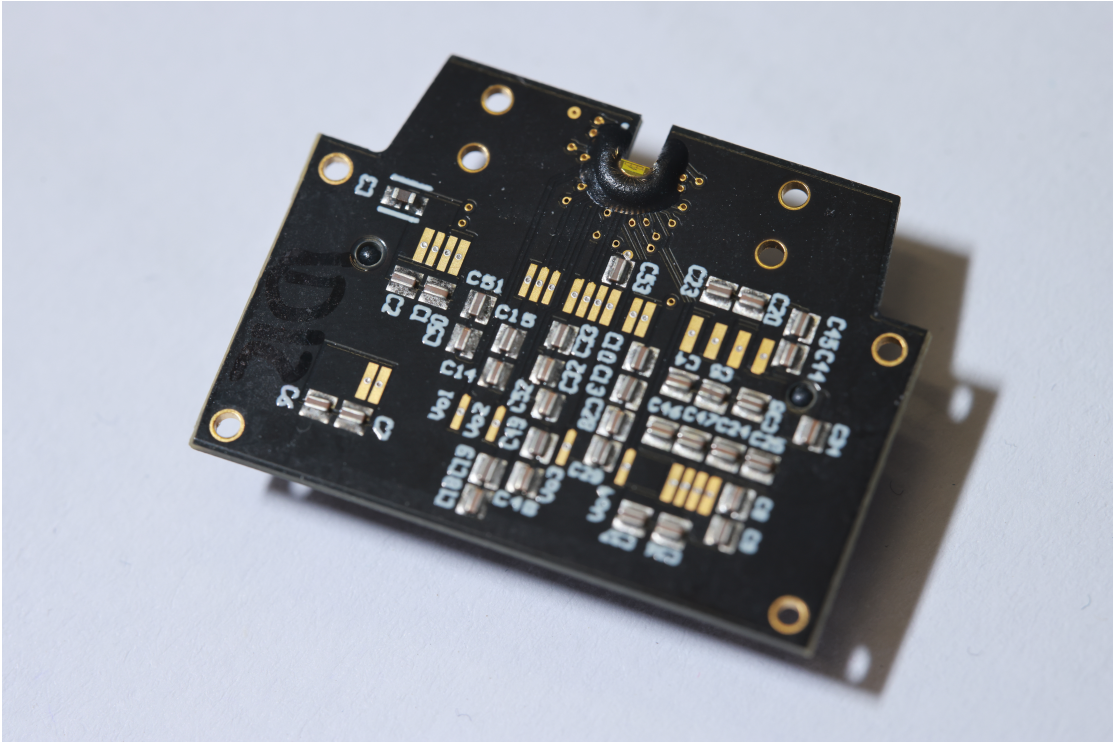


Figure B.2: High timing precision SPAD pixel [68]

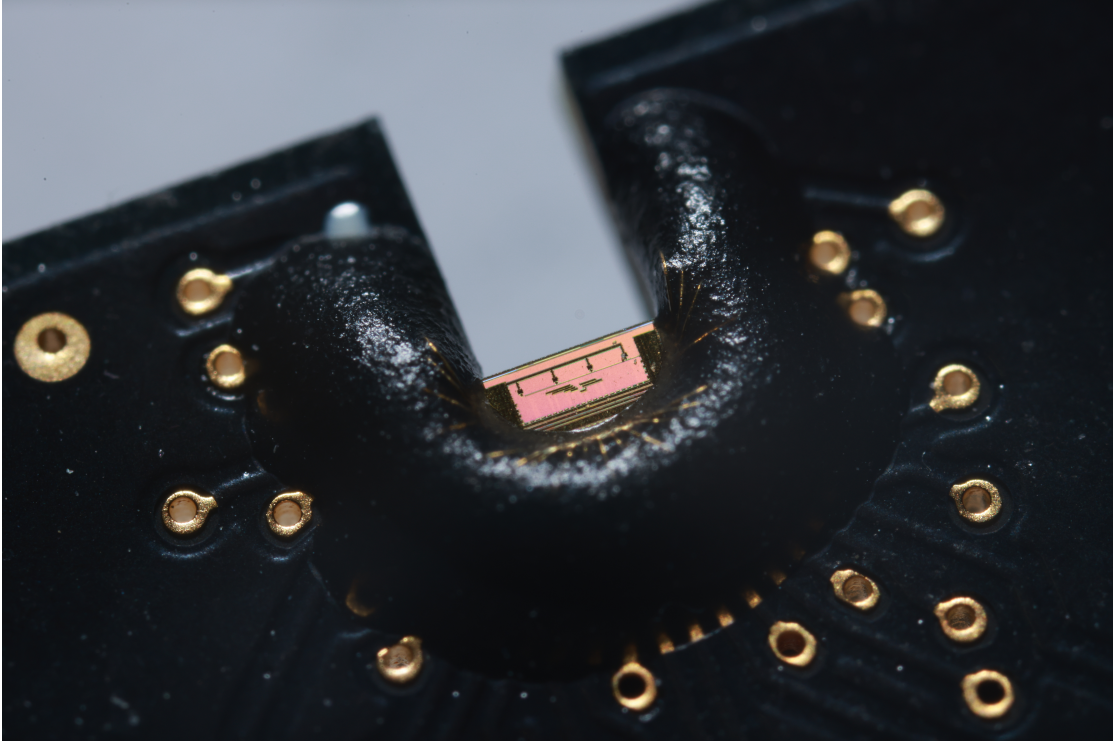


Figure B.3: High timing precision SPAD pixel [68]

Bibliography

- [1] C. Veerappan and E. Charbon, "A low dark count pin diode based SPAD in CMOS technology", *IEEE transactions on electron devices*, vol. 63, no. 1, pp. 65–71, 2015.
- [2] R. H. Haitz, "Mechanisms contributing to the noise pulse rate of avalanche diodes", *Journal of Applied Physics*, vol. 36, no. 10, pp. 3123–3131, 1965.
- [3] F. Sun, Y. Xu, Z. Wu, and J. Zhang, "A simple analytic modeling method for SPAD timing jitter prediction", *IEEE Journal of the Electron Devices Society*, vol. 7, pp. 261–267, 2019.
- [4] S. Lindner, S. Pellegrini, Y. Henrion, B. Rae, M. Wolf, and E. Charbon, "A high-PDE, backside-illuminated SPAD in 65/40-nm 3D IC CMOS pixel with cascaded passive quenching and active recharge", *IEEE Electron Device Letters*, vol. 38, no. 11, pp. 1547–1550, 2017.
- [5] K. K. Mehta, "Integrated optical quantum manipulation and measurement of trapped ions", Ph.D. dissertation, Massachusetts Institute of Technology, 2017.
- [6] A. Morelle, F. Gramuglia, P. Keshavarzian, *et al.*, "Deep cryogenic operation of 55 nm CMOS SPADs for quantum information and metrology applications", in *Quantum Information and Measurement*, Optica Publishing Group, 2021, M2B–7.
- [7] V. T. Bickel, B. Moseley, I. Lopez-Francos, and M. Shirley, "Peering into lunar permanently shadowed regions with deep learning", *Nature Communications*, vol. 12, no. 1, p. 5607, 2021.
- [8] A. S. Jursa *et al.*, *Handbook of geophysics and the space environment*. Air Force Geophysics Laboratory, Air Force Systems Command, United States . . . , 1985, vol. 1.
- [9] M. W. Fishburn, *Fundamentals of CMOS single-photon avalanche diodes*. fishburn, 2012.
- [10] M. Manghisoni, L. Ratti, V. Re, and V. Speziali, "Radiation hardness perspectives for the design of analog detector readout circuits in the 0.18-/spl mu/m CMOS generation", *IEEE Transactions on Nuclear Science*, vol. 49, no. 6, pp. 2902–2909, 2002.
- [11] F. Faccio and G. Cervelli, "Radiation-induced edge effects in deep submicron CMOS transistors", *IEEE Transactions on Nuclear Science*, vol. 52, no. 6, pp. 2413–2420, 2005.

-
- [12] S. Bonacini, P. Valerio, R. Avramidou, *et al.*, “Characterization of a commercial 65 nm CMOS technology for SLHC applications”, *Journal of Instrumentation*, vol. 7, no. 01, P01015, 2012.
- [13] M. Boscherini, O. Adriani, M. Bonghi, *et al.*, “Radiation damage of electronic components in space environment”, *Nuclear Instruments and Methods in Physics Research Section A: Accelerators, Spectrometers, Detectors and Associated Equipment*, vol. 514, no. 1-3, pp. 112–116, 2003.
- [14] H. Lischka, H. Henschel, W. Lennartz, and K. Schmidt, “Radiation sensitivity of light emitting diodes (LED), laser diodes (LD) and photodiodes (PD)”, *IEEE transactions on nuclear science*, vol. 39, no. 3, pp. 423–427, 1992.
- [15] O. Marcelot, V. Goiffon, M. Raine, *et al.*, “Radiation effects in CCD on CMOS devices: first analysis of TID and DDD effects”, *IEEE Transactions on Nuclear Science*, vol. 62, no. 6, pp. 2965–2970, 2015.
- [16] G. Brunetti, I. McKenzie, F. Dell’Olio, M. N. Armenise, and C. Ciminelli, “Measured radiation effects on InGaAsP/InP ring resonators for space applications”, *Optics express*, vol. 27, no. 17, pp. 24 434–24 444, 2019.
- [17] E. Garutti and Y. Musienko, “Radiation damage of SiPMs”, *Nuclear Instruments and Methods in Physics Research Section A: Accelerators, Spectrometers, Detectors and Associated Equipment*, vol. 926, pp. 69–84, 2019.
- [18] M. Hofbauer, B. Steindl, K. Schneider-Hornstein, B. Goll, K.-O. Voss, and H. Zimmermann, “Single-event transients in a PIN photodiode and a single-photon avalanche diode integrated in 0.35 μm CMOS”, in *2018 18th European Conference on Radiation and Its Effects on Components and Systems (RADECS)*, IEEE, 2018, pp. 1–5.
- [19] V. Brasch, Q.-F. Chen, S. Schiller, and T. J. Kippenberg, “Radiation hardness of high-Q silicon nitride microresonators for space compatible integrated optics”, *Optics express*, vol. 22, no. 25, pp. 30 786–30 794, 2014.
- [20] K. A. Gill, G. Cervelli, R. Grabit, F. B. Jensen, and F. Vasey, “Radiation damage and annealing in 1310-nm InGaAsP/InP lasers for the CMS tracker”, in *Photonics for Space Environments VII*, SPIE, vol. 4134, 2000, pp. 176–184.
- [21] J. A. Smith, V. H. Dhulla, S. S. Mukherjee, *et al.*, “Evaluation of an operational concept for improving radiation tolerance of single-photon avalanche diode (SPAD) arrays”, *IEEE Transactions on Nuclear Science*, vol. 67, no. 5, pp. 797–804, 2020.
- [22] J. Kodet, I. Prochazka, J. Blazej, X. Sun, and J. Cavanaugh, “Single photon avalanche diode radiation tests”, *Nuclear Instruments and Methods in Physics Research Section A: Accelerators, Spectrometers, Detectors and Associated Equipment*, vol. 695, pp. 309–312, 2012.

BIBLIOGRAPHY

- [23] V. Malherbe, S. De Paoli, B. Mamdy, G. Gasiot, and P. Roche, “Displacement damage characterization of CMOS single-photon avalanche diodes: alpha-particle and fast-neutron measurements”, *IEEE Transactions on Nuclear Science*, vol. 68, no. 5, pp. 777–784, 2021.
- [24] L. Ratti, P. Brogi, G. Collazuol, *et al.*, “Dark count rate degradation in CMOS SPADs exposed to X-rays and neutrons”, *IEEE Transactions on Nuclear Science*, vol. 66, no. 2, pp. 567–574, 2019.
- [25] Y. Li, C. Veerappan, M.-J. Lee, L. Wen, Q. Guo, and E. Charbon, “A radiation-tolerant, high performance SPAD for SiPMs implemented in CMOS technology”, in *2016 IEEE Nuclear Science Symposium, Medical Imaging Conference and Room-Temperature Semiconductor Detector Workshop (NSS/MIC/RTSD)*, IEEE, 2016, pp. 1–4.
- [26] M. Campajola, F. Di Capua, D. Fiore, C. Nappi, E. Sarnelli, and L. Gasparini, “Long-term degradation study of CMOS SPADs in space radiation environment”, in *2018 18th European Conference on Radiation and Its Effects on Components and Systems (RADECS)*, IEEE, 2018, pp. 1–5.
- [27] G. Anelli, M. Campbell, M. Delmastro, *et al.*, “Radiation tolerant VLSI circuits in standard deep submicron CMOS technologies for the LHC experiments: practical design aspects”, *IEEE Transactions on Nuclear Science*, vol. 46, no. 6, pp. 1690–1696, 1999.
- [28] E. Anisimova, B. L. Higgins, J.-P. Bourgoïn, *et al.*, “Mitigating radiation damage of single photon detectors for space applications”, *EPJ Quantum Technology*, vol. 4, pp. 1–14, 2017.
- [29] I. DSouza, J.-P. Bourgoïn, B. L. Higgins, *et al.*, “Repeated radiation damage and thermal annealing of avalanche photodiodes”, *EPJ Quantum Technology*, vol. 8, no. 1, p. 13, 2021.
- [30] J. G. Lim, E. Anisimova, B. L. Higgins, J.-P. Bourgoïn, T. Jennewein, and V. Makarov, “Laser annealing heals radiation damage in avalanche photodiodes”, *EPJ quantum technology*, vol. 4, pp. 1–16, 2017.
- [31] J. Krynski, N. Sultana, Y. S. Lee, V. Makarov, and T. Jennewein, “Protocols for healing radiation-damaged single-photon detectors suitable for space environment”, *arXiv preprint arXiv:2305.10959*, 2023.
- [32] R. C. Wiens, S. Maurice, B. Barraclough, *et al.*, “The ChemCam instrument suite on the Mars Science Laboratory (MSL) rover: Body unit and combined system tests”, *Space science reviews*, vol. 170, pp. 167–227, 2012.
- [33] B. Sallé, J.-L. Lacour, E. Vors, *et al.*, “Laser-induced breakdown spectroscopy for Mars surface analysis: capabilities at stand-off distances and detection of chlorine and sulfur elements”, *Spectrochimica Acta Part B: Atomic Spectroscopy*, vol. 59, no. 9, pp. 1413–1422, 2004.

- [34] C. S. Thiel, S. Tauber, C. Seebacher, *et al.*, “Real-time 3D high-resolution microscopy of human cells on the international space station”, *International journal of molecular sciences*, vol. 20, no. 8, p. 2033, 2019.
- [35] K. Morimoto, A. Ardelean, M.-L. Wu, *et al.*, “Megapixel time-gated SPAD image sensor for 2D and 3D imaging applications”, *Optica*, vol. 7, no. 4, pp. 346–354, 2020.
- [36] K. Morimoto, J. Iwata, M. Shinohara, *et al.*, “3.2 megapixel 3D-stacked charge focusing SPAD for low-light imaging and depth sensing”, in *2021 IEEE International Electron Devices Meeting (IEDM)*, IEEE, 2021, pp. 20–2.
- [37] R. K. Henderson, N. Johnston, S. W. Hutchings, *et al.*, “5.7 a 256 × 256 40nm/90nm CMOS 3d-stacked 120dB dynamic-range reconfigurable time-resolved SPAD imager”, in *2019 IEEE International Solid-State Circuits Conference-(ISSCC)*, IEEE, 2019, pp. 106–108.
- [38] Y. Ota, K. Morimoto, T. Sasago, *et al.*, “A 0.37 w 143dB-dynamic-range 1Mpixel backside-illuminated charge-focusing SPAD image sensor with pixel-wise exposure control and adaptive clocked recharging”, in *2022 IEEE International Solid-State Circuits Conference (ISSCC)*, IEEE, vol. 65, 2022, pp. 94–96.
- [39] J. Ogi, T. Takatsuka, K. Hizu, *et al.*, “A 250fps 124dB dynamic-range SPAD image sensor stacked with pixel-parallel photon counter employing sub-frame extrapolating architecture for motion artifact suppression”, in *2021 IEEE International Solid-State Circuits Conference (ISSCC)*, IEEE, vol. 64, 2021, pp. 113–115.
- [40] N. A. Dutton, L. Parmesan, A. J. Holmes, L. A. Grant, and R. K. Henderson, “320 × 240 oversampled digital single photon counting image sensor”, in *2014 Symposium on VLSI Circuits Digest of Technical Papers*, IEEE, 2014, pp. 1–2.
- [41] O. Kumagai, J. Ohmachi, M. Matsumura, *et al.*, “A 189 × 600 back-illuminated stacked SPAD direct time-of-flight depth sensor for automotive LiDAR systems”, in *2021 IEEE International Solid-State Circuits Conference (ISSCC)*, IEEE, vol. 64, 2021, pp. 110–112.
- [42] K. Yoshioka, H. Kubota, T. Fukushima, *et al.*, “A 20-ch TDC/ADC hybrid architecture LiDAR soc for 240 × 96 pixel 200-m range imaging with smart accumulation technique and residue quantizing SAR ADC”, *IEEE Journal of Solid-State Circuits*, vol. 53, no. 11, pp. 3026–3038, 2018.
- [43] X. Ren, P. W. Connolly, A. Halimi, *et al.*, “High-resolution depth profiling using a range-gated CMOS SPAD quanta image sensor”, *Optics express*, vol. 26, no. 5, pp. 5541–5557, 2018.
- [44] A. R. Ximenes, P. Padmanabhan, M.-J. Lee, Y. Yamashita, D.-N. Yaung, and E. Charbon, “A modular, direct time-of-flight depth sensor in 45/65-nm 3-D-stacked CMOS technology”, *IEEE Journal of Solid-State Circuits*, vol. 54, no. 11, pp. 3203–3214, 2019.
- [45] T. Talala, E. Parkkinen, and I. Nissinen, “CMOS SPAD line sensor with fine-tunable parallel connected time-to-digital converters for Raman spectroscopy”, *IEEE Journal of Solid-State Circuits*, 2022.

BIBLIOGRAPHY

- [46] Y. Maruyama, J. Blacksberg, and E. Charbon, “A 1024×8 , 700-ps time-gated SPAD line sensor for planetary surface exploration with laser Raman spectroscopy and LIBS”, *IEEE Journal of Solid-State Circuits*, vol. 49, no. 1, pp. 179–189, 2013.
- [47] J. Kostamovaara, J. Tenhunen, M. Kögler, I. Nissinen, J. Nissinen, and P. Keränen, “Fluorescence suppression in Raman spectroscopy using a time-gated CMOS SPAD”, *Optics express*, vol. 21, no. 25, pp. 31 632–31 645, 2013.
- [48] A. C. Ulku, C. Bruschini, I. M. Antolović, *et al.*, “A 512×512 SPAD image sensor with integrated gating for widefield FLIM”, *IEEE Journal of Selected Topics in Quantum Electronics*, vol. 25, no. 1, pp. 1–12, 2018.
- [49] V. Zickus, M.-L. Wu, K. Morimoto, *et al.*, “Fluorescence lifetime imaging with a megapixel SPAD camera and neural network lifetime estimation”, *Scientific Reports*, vol. 10, no. 1, p. 20 986, 2020.
- [50] L. Parmesan, N. Dutton, N. J. Calder, *et al.*, “A 256×256 SPAD array with in-pixel time to amplitude conversion for fluorescence lifetime imaging microscopy”, *Memory*, vol. 900, no. M4, p. M5, 2015.
- [51] H.-K. Lo, M. Curty, and K. Tamaki, “Secure quantum key distribution”, *Nature Photonics*, vol. 8, no. 8, pp. 595–604, 2014.
- [52] E. Diamanti, H.-K. Lo, B. Qi, and Z. Yuan, “Practical challenges in quantum key distribution”, *npj Quantum Information*, vol. 2, no. 1, pp. 1–12, 2016.
- [53] R. Bedington, J. M. Arrazola, and A. Ling, “Progress in satellite quantum key distribution”, *npj Quantum Information*, vol. 3, no. 1, p. 30, 2017.
- [54] S.-K. Liao, W.-Q. Cai, W.-Y. Liu, *et al.*, “Satellite-to-ground quantum key distribution”, *Nature*, vol. 549, no. 7670, pp. 43–47, 2017.
- [55] N. Massari, L. Gasparini, A. Tomasi, *et al.*, “16.3 a 16×16 pixels SPAD-based 128-mb/s quantum random number generator with- 74dB light rejection ratio and- 6.7 ppm/ $^{\circ}$ C bias sensitivity on temperature”, in *2016 IEEE International Solid-State Circuits Conference (ISSCC)*, IEEE, 2016, pp. 292–293.
- [56] P. Keshavarzian, K. Ramu, D. Tang, *et al.*, “A 3.3-Gb/s SPAD-Based Quantum Random Number Generator”, *IEEE Journal of Solid-State Circuits*, 2023.
- [57] R. Aaij, G. Ciezarek, P. Collins, *et al.*, “Expression of Interest for a Phase-II LHCb Upgrade: Opportunities in flavour physics, and beyond, in the HL-LHC era”, Tech. Rep., 2017.
- [58] A. Collaboration *et al.*, “Letter of intent for ALICE 3: A next-generation heavy-ion experiment at the LHC”, *arXiv e-prints*, arXiv-2211, 2022.
- [59] M. Marisaldi, A. Berra, F. Moscatelli, *et al.*, “Scintillating fibers readout by single photon avalanche diodes (spad) for space applications”, in *Space Telescopes and Instrumentation 2012: Ultraviolet to Gamma Ray*, SPIE, vol. 8443, 2012, pp. 157–165.

- [60] L. Pancheri, A. Ficorella, P. Brogi, *et al.*, “First demonstration of a two-tier pixelated avalanche sensor for charged particle detection”, *IEEE Journal of the Electron Devices Society*, vol. 5, no. 5, pp. 404–410, 2017.
- [61] L. Ratti, P. Brogi, G. Collazuol, *et al.*, “Layered CMOS SPADs for low noise detection of charged particles”, *Frontiers in Physics*, vol. 8, p. 625, 2021.
- [62] F. Gramuglia, E. Ripiccini, C. A. Fenoglio, *et al.*, “Sub-10 ps minimum ionizing particle detection with geiger-mode APDs”, *Front. in Phys.*, vol. 10, p. 849 237, 2022. DOI: 10.3389/fphy.2022.849237. arXiv: 2111.09998 [physics.ins-det].
- [63] K. Morimoto and E. Charbon, “A scaling law for SPAD pixel miniaturization”, *Sensors*, vol. 21, no. 10, p. 3447, 2021.
- [64] F. Yang, Y. M. Lu, L. Sbaiz, and M. Vetterli, “Bits from photons: oversampled image acquisition using binary poisson statistics”, *IEEE Transactions on image processing*, vol. 21, no. 4, pp. 1421–1436, 2011.
- [65] M.-L. Wu, E. Ripiccini, E. Kizilkan, *et al.*, “Radiation hardness study of single-photon avalanche diode for space and high energy physics applications”, *Sensors*, vol. 22, no. 8, p. 2919, 2022.
- [66] F. Gramuglia, P. Keshavarzian, E. Kizilkan, *et al.*, “Engineering breakdown probability profile for PDP and DCR optimization in a SPAD fabricated in a standard 55 nm BCD process”, *IEEE Journal of Selected Topics in Quantum Electronics*, vol. 28, no. 2: Optical Detectors, pp. 1–10, 2021.
- [67] P. Keshavarzian, F. Gramuglia, E. Kizilkan, *et al.*, “Low-noise high-dynamic-range single-photon avalanche diodes with integrated PQAR circuit in a standard 55nm BCD process”, in *Advanced Photon Counting Techniques XVI*, SPIE, vol. 12089, 2022, pp. 73–82.
- [68] F. Gramuglia, M.-L. Wu, C. Bruschini, M.-J. Lee, and E. Charbon, “A low-noise CMOS SPAD pixel with 12.1 ps SPTR and 3 ns dead time”, *IEEE Journal of Selected Topics in Quantum Electronics*, vol. 28, no. 2, pp. 1–9, 2021.
- [69] H. Xu, L. Pancheri, G.-F. Dalla Betta, and D. Stoppa, “Design and characterization of a p+/n-well SPAD array in 150nm CMOS process”, *Optics express*, vol. 25, no. 11, pp. 12 765–12 778, 2017.
- [70] X. Sun, D. Reusser, H. Dautet, and J. B. Abshire, “Measurement of proton radiation damage to Si avalanche photodiodes”, *IEEE transactions on Electron Devices*, vol. 44, no. 12, pp. 2160–2166, 1997.
- [71] F. Moscatelli, M. Marisaldi, P. Maccagnani, *et al.*, “Radiation tests of single photon avalanche diode for space applications”, *Nuclear Instruments and Methods in Physics Research Section A: Accelerators, Spectrometers, Detectors and Associated Equipment*, vol. 711, pp. 65–72, 2013.
- [72] C. H. Bennett, F. Bessette, G. Brassard, L. Salvail, and J. Smolin, “Experimental quantum cryptography”, *Journal of cryptology*, vol. 5, pp. 3–28, 1992.

BIBLIOGRAPHY

- [73] V. Dhulla, S. S. Mukherjee, A. O. Lee, N. Dissanayake, B. Ryu, and C. Myers, “256 x 256 dual-mode CMOS SPAD image sensor”, in *Advanced Photon Counting Techniques XIII*, SPIE, vol. 10978, 2019, pp. 109–116.
- [74] G. D. Watkins, “Intrinsic defects in silicon”, *Materials science in semiconductor processing*, vol. 3, no. 4, pp. 227–235, 2000.
- [75] R. Hull, *Properties of crystalline silicon*. IET, 1999.
- [76] E. A. Webster, R. L. Nicol, L. Grant, and D. Renshaw, “Per-pixel dark current spectroscopy measurement and analysis in CMOS image sensors”, *IEEE Transactions on electron devices*, vol. 57, no. 9, pp. 2176–2182, 2010.
- [77] E. A. Webster and R. K. Henderson, “A TCAD and spectroscopy study of dark count mechanisms in single-photon avalanche diodes”, *IEEE transactions on electron devices*, vol. 60, no. 12, pp. 4014–4019, 2013.
- [78] Y. Xu, P. Xiang, and X. Xie, “Comprehensive understanding of dark count mechanisms of single-photon avalanche diodes fabricated in deep sub-micron CMOS technologies”, *Solid-State Electronics*, vol. 129, pp. 168–174, 2017.
- [79] J. Frenkel, “On pre-breakdown phenomena in insulators and electronic semi-conductors”, *Physical Review*, vol. 54, no. 8, p. 647, 1938.
- [80] J. Srour and R. Hartmann, “Enhanced displacement damage effectiveness in irradiated silicon devices”, *IEEE Transactions on Nuclear Science*, vol. 36, no. 6, pp. 1825–1830, 1989.
- [81] G. Humer, M. Peev, C. Schaeff, S. Ramelow, M. Stipčević, and R. Ursin, “A simple and robust method for estimating afterpulsing in single photon detectors”, *Journal of Lightwave Technology*, vol. 33, no. 14, pp. 3098–3107, 2015.
- [82] E. Kerstel, A. Gardelein, M. Barthelemy, M. Fink, S. K. Joshi, and R. Ursin, “Nanobob: a CubeSat mission concept for quantum communication experiments in an uplink configuration”, *EPJ Quantum Technology*, vol. 5, no. 1, p. 6, 2018.
- [83] C. Papapanos, D. Zavitsanos, G. Giannoulis, A. Raptakis, C. Kouloumentas, and H. Avramopoulos, “Afterpulsing effect on the baseline system error rate and on the decoy-state quantum key distribution protocols”, *arXiv preprint arXiv:2010.03358*, 2020.
- [84] M. Herrero-Collantes and J. C. Garcia-Escartin, “Quantum random number generators”, *Reviews of Modern Physics*, vol. 89, no. 1, p. 015 004, 2017.
- [85] Z. Cheng, X. Zheng, D. Palubiak, M. J. Deen, and H. Peng, “A comprehensive and accurate analytical SPAD model for circuit simulation”, *IEEE Transactions on Electron Devices*, vol. 63, no. 5, pp. 1940–1948, 2016.
- [86] J. Srour and D. Lo, “Universal damage factor for radiation-induced dark current in silicon devices”, *IEEE Transactions on Nuclear Science*, vol. 47, no. 6, pp. 2451–2459, 2000.

- [87] M. A. Karami, A. Pil-Ali, and M. R. Safaee, "Multistable defect characterization in proton irradiated single-photon avalanche diodes", *Optical and Quantum Electronics*, vol. 47, no. 7, pp. 2155–2160, 2015.
- [88] M. Campajola, F. Di Capua, D. Fiore, E. Sarnelli, and A. Aloisio, "Proton induced dark count rate degradation in 150-nm CMOS single-photon avalanche diodes", *Nuclear Instruments and Methods in Physics Research Section A: Accelerators, Spectrometers, Detectors and Associated Equipment*, vol. 947, p. 162 722, 2019.
- [89] T. Nuns, G. Quadri, J.-P. David, and O. Gilard, "Annealing of proton-induced random telegraph signal in CCDs", *IEEE transactions on Nuclear Science*, vol. 54, no. 4, pp. 1120–1128, 2007.
- [90] E. A. Swanson, E. R. Arnau, and F. G. Walther, "Measurements of natural radiation effects in a low noise avalanche photodiode", *IEEE Transactions on Nuclear Science*, vol. 34, no. 6, pp. 1658–1661, 1987.
- [91] X. Sun and H. Dautet, "Proton radiation damage of Si APD single photon counters", in *2001 IEEE Radiation Effects Data Workshop. NSREC 2001. Workshop Record. Held in conjunction with IEEE Nuclear and Space Radiation Effects Conference (Cat. No. 01TH8588)*, IEEE, 2001, pp. 146–150.
- [92] D. Fleetwood, P. Winokur, and J. Schwank, "Using laboratory X-ray and cobalt-60 irradiations to predict CMOS device response in strategic and space environments", *IEEE Transactions on Nuclear Science*, vol. 35, no. 6, pp. 1497–1505, 1988.
- [93] J. R. Schwank, M. R. Shaneyfelt, D. M. Fleetwood, *et al.*, "Radiation effects in MOS oxides", *IEEE Transactions on Nuclear Science*, vol. 55, no. 4, pp. 1833–1853, 2008.
- [94] M. Fiorini, "The upgrade of the LHCb RICH detectors", *Nuclear Instruments and Methods in Physics Research Section A: Accelerators, Spectrometers, Detectors and Associated Equipment*, vol. 952, p. 161 688, 2020.
- [95] L. Snoj, G. Žerovnik, and A. Trkov, "Computational analysis of irradiation facilities at the JSI TRIGA reactor", *Applied Radiation and Isotopes*, vol. 70, no. 3, pp. 483–488, 2012.
- [96] G. Watkins, J. Corbett, and R. Walker, "Spin resonance in electron irradiated silicon", *Journal of Applied Physics*, vol. 30, no. 8, pp. 1198–1203, 1959.
- [97] G. Watkins and J. Corbett, "Defects in irradiated silicon. I. electron spin resonance of the Si-A center", *Physical Review*, vol. 121, no. 4, p. 1001, 1961.
- [98] G. Watkins and J. Corbett, "Defects in irradiated silicon: electron paramagnetic resonance and electron-nuclear double resonance of the si-e center", *Physical Review*, vol. 134, no. 5A, A1359, 1964.
- [99] J.-M. Belloir, V. Goiffon, C. Virmontois, *et al.*, "Dark current spectroscopy on alpha irradiated pinned photodiode CMOS image sensors", *IEEE Transactions on Nuclear Science*, vol. 63, no. 4, pp. 2183–2192, 2016.

BIBLIOGRAPHY

- [100] C.-T. Sah, R. N. Noyce, and W. Shockley, "Carrier generation and recombination in pn junctions and pn junction characteristics", *Proceedings of the IRE*, vol. 45, no. 9, pp. 1228–1243, 1957.
- [101] W. Shockley and W. Read Jr, "Statistics of the recombinations of holes and electrons", *Physical review*, vol. 87, no. 5, p. 835, 1952.
- [102] R. N. Hall, "Electron-hole recombination in germanium", *Physical review*, vol. 87, no. 2, p. 387, 1952.
- [103] K. T. Lim, H. Kim, J. Kim, and G. Cho, "Effect of electric field on primary dark pulses in SPADs for advanced radiation detection applications", *Nuclear Engineering and Technology*, vol. 53, no. 2, pp. 618–625, 2021.
- [104] W. Shockley, *Electrons and holes in semiconductors: with applications to transistor electronics*. van Nostrand, 1959, pp. 465–475.
- [105] Y. Yoshida and G. Langouche, *Defects and impurities in silicon materials*. Springer, 2015.
- [106] D. Lang, "Deep-level transient spectroscopy: a new method to characterize traps in semiconductors", *Journal of applied physics*, vol. 45, no. 7, pp. 3023–3032, 1974.
- [107] D. B. Jackson and C. Sah, "Thermally generated electron traps in boron-implanted, phosphorus-doped silicon", *Journal of applied physics*, vol. 58, no. 6, pp. 2225–2229, 1985.
- [108] G.-G. Qin, M.-F. Li, and C.-T. Sah, "Deep level profiles in boron implanted n-Si", *Journal of Applied Physics*, vol. 53, no. 7, pp. 4800–4811, 1982.
- [109] M.-f. Li and C.-T. Sah, "A new method for the determination of dopant and trap concentration profiles in semiconductors", *IEEE Transactions on Electron Devices*, vol. 29, no. 2, pp. 306–315, 1982.
- [110] S. Cova, A. Lacaita, and G. Ripamonti, "Trapping phenomena in avalanche photodiodes on nanosecond scale", *IEEE Electron device letters*, vol. 12, no. 12, pp. 685–687, 1991.
- [111] V. Markevich, I. Hawkins, A. Peaker, *et al.*, "Vacancy-group-V-impurity atom pairs in Ge crystals doped with P, As, Sb, and Bi", *Physical Review B*, vol. 70, no. 23, p. 235 213, 2004.
- [112] M. Liu, C. Hu, X. Bai, *et al.*, "High-performance InGaAs/InP single-photon avalanche photodiode", *IEEE Journal of selected topics in quantum electronics*, vol. 13, no. 4, pp. 887–894, 2007.
- [113] M. Ghioni, A. Gulinatti, P. Maccagnani, I. Rech, and S. Cova, "Planar silicon SPADs with 200- μm diameter and 35-ps photon timing resolution", in *Advanced Photon Counting Techniques*, SPIE, vol. 6372, 2006, pp. 203–211.
- [114] T. Katsube, K. Kakimoto, and T. Ikoma, "Temperature and energy dependences of capture cross sections at surface states in Si metal-oxide-semiconductor diodes measured by deep level transient spectroscopy", *Journal of Applied Physics*, vol. 52, no. 5, pp. 3504–3508, 1981.

- [115] L. Ratti, P. Brogi, G. Collazuol, *et al.*, “DCR performance in neutron-irradiated cmos spads from 150-to 180-nm technologies”, *IEEE Transactions on Nuclear Science*, vol. 67, no. 7, pp. 1293–1301, 2020.
- [116] M. A. Itzler, X. Jiang, and M. Entwistle, “Power law temporal dependence of InGaAs/InP SPAD afterpulsing”, *Journal of Modern Optics*, vol. 59, no. 17, pp. 1472–1480, 2012.
- [117] B. A. Wilson, A. Miloshevsky, D. A. Hooper, and N. A. Peters, “Radiation-induced dark counts for silicon single-photon detectors in space”, *Physical Review Applied*, vol. 16, no. 6, p. 064 049, 2021.
- [118] K. Morimoto, M.-L. Wu, A. Ardelean, and E. Charbon, “Superluminal motion-assisted four-dimensional light-in-flight imaging”, *Physical Review X*, vol. 11, no. 1, p. 011 005, 2021.
- [119] E. R. Fossum, J. Ma, S. Masoodian, L. Anzagira, and R. Zizza, “The quanta image sensor: every photon counts”, *Sensors*, vol. 16, no. 8, p. 1260, 2016.
- [120] E. R. Fossum, “Modeling the performance of single-bit and multi-bit quanta image sensors”, *IEEE Journal of the Electron Devices Society*, vol. 1, no. 9, pp. 166–174, 2013.
- [121] I. M. Antolovic, C. Bruschini, and E. Charbon, “Dynamic range extension for photon counting arrays”, *Optics Express*, vol. 26, no. 17, pp. 22 234–22 248, 2018.
- [122] J. R. Lakowicz and J. R. Lakowicz, “Time-domain lifetime measurements”, *Principles of fluorescence spectroscopy*, pp. 95–140, 1999.
- [123] W. Becker, “Fluorescence lifetime imaging—techniques and applications”, *Journal of microscopy*, vol. 247, no. 2, pp. 119–136, 2012.
- [124] A. H. P. Ho, D. Kim, and M. G. Somekh, *Handbook of photonics for biomedical engineering*. Springer Netherlands, 2017.
- [125] E. B. van Munster and T. W. Gadella, “Fluorescence lifetime imaging microscopy (FLIM)”, *Microscopy Techniques: -/-*, pp. 143–175, 2005.
- [126] H.-J. Lin, P. Herman, and J. R. Lakowicz, “Fluorescence lifetime-resolved pH imaging of living cells”, *Cytometry part A: the journal of the international society for analytical cytology*, vol. 52, no. 2, pp. 77–89, 2003.
- [127] M. Y. Berezin and S. Achilefu, “Fluorescence lifetime measurements and biological imaging”, *Chemical reviews*, vol. 110, no. 5, pp. 2641–2684, 2010.
- [128] J. W. Borst and A. J. Visser, “Fluorescence lifetime imaging microscopy in life sciences”, *Measurement Science and Technology*, vol. 21, no. 10, p. 102 002, 2010.
- [129] D.-H. Lee, X. Li, N. Ma, M. A. Digman, and A. P. Lee, “Rapid and label-free identification of single leukemia cells from blood in a high-density microfluidic trapping array by fluorescence lifetime imaging microscopy”, *Lab on a Chip*, vol. 18, no. 9, pp. 1349–1358, 2018.

BIBLIOGRAPHY

- [130] J. A. Jo, S. Cheng, R. Cuenca-Martinez, *et al.*, “Endogenous fluorescence lifetime imaging (FLIM) endoscopy for early detection of oral cancer and dysplasia”, in *2018 40th Annual International Conference of the IEEE Engineering in Medicine and Biology Society (EMBC)*, IEEE, 2018, pp. 3009–3012.
- [131] S. Gershanov, S. Michowiz, H. Toledano, *et al.*, “Fluorescence lifetime imaging microscopy, a novel diagnostic tool for metastatic cell detection in the cerebrospinal fluid of children with medulloblastoma”, *Scientific reports*, vol. 7, no. 1, p. 3648, 2017.
- [132] M. Wang, F. Tang, X. Pan, *et al.*, “Rapid diagnosis and intraoperative margin assessment of human lung cancer with fluorescence lifetime imaging microscopy”, *BBA clinical*, vol. 8, pp. 7–13, 2017.
- [133] T. Etrych, H. Lucas, O. Janoušková, P. Chytil, T. Mueller, and K. Mäder, “Fluorescence optical imaging in anticancer drug delivery”, *Journal of Controlled Release*, vol. 226, pp. 168–181, 2016.
- [134] M. Carlson, A. L. Watson, L. Anderson, D. A. Largaespada, and P. P. Provenzano, “Multi-photon fluorescence lifetime imaging of chemotherapy distribution in solid tumors”, *Journal of biomedical optics*, vol. 22, no. 11, pp. 116 010–116 010, 2017.
- [135] Y. Ardeshirpour, V. Chernomordik, M. Hassan, R. Zielinski, J. Capala, and A. Gandjbakhche, “In vivo fluorescence lifetime imaging for monitoring the efficacy of the cancer treatment”, *Clinical Cancer Research*, vol. 20, no. 13, pp. 3531–3539, 2014.
- [136] S. Kawanabe, Y. Araki, T. Uchimura, and T. Imasaka, “Applying fluorescence lifetime imaging microscopy to evaluate the efficacy of anticancer drugs”, *Methods and Applications in Fluorescence*, vol. 3, no. 2, p. 025 006, 2015.
- [137] O. I. Kolenc and K. P. Quinn, “Evaluating cell metabolism through autofluorescence imaging of NAD (P) H and FAD”, *Antioxidants & redox signaling*, vol. 30, no. 6, pp. 875–889, 2019.
- [138] Z. Wang, Y. Zheng, D. Zhao, *et al.*, “Applications of fluorescence lifetime imaging in clinical medicine”, *Journal of Innovative Optical Health Sciences*, vol. 11, no. 01, p. 1 830 001, 2018.
- [139] O. Peng and W. J. Akers, “Fluorescence lifetime imaging of cancer in vivo”, *In Vivo Fluorescence Imaging: Methods and Protocols*, pp. 55–66, 2016.
- [140] J. R. Lakowicz, *Principles of fluorescence spectroscopy*. Springer, 2006.
- [141] W. Becker, “The bh tcspc handbook. 8th”, *Becker & Hickl GmbH*, 2019.
- [142] R. A. Colyer, O. H. Siegmund, A. S. Tremsin, J. V. Vallerga, S. Weiss, and X. Michalet, “Phasor imaging with a widefield photon-counting detector”, *Journal of biomedical optics*, vol. 17, no. 1, pp. 016 008–016 008, 2012.
- [143] M. A. Digman, V. R. Caiolfa, M. Zamai, and E. Gratton, “The phasor approach to fluorescence lifetime imaging analysis”, *Biophysical journal*, vol. 94, no. 2, pp. L14–L16, 2008.

- [144] A. Ulku, A. Ardelean, M. Antolovic, *et al.*, “Wide-field time-gated SPAD imager for phasor-based FLIM applications”, *Methods and applications in fluorescence*, vol. 8, no. 2, p. 024 002, 2020.
- [145] B. Tang, Z. Pan, K. Yin, and A. Khateeb, “Recent advances of deep learning in bioinformatics and computational biology”, *Frontiers in genetics*, vol. 10, p. 214, 2019.
- [146] R. Yao, M. Ochoa, P. Yan, and X. Intes, “Net-FLICS: fast quantitative wide-field fluorescence lifetime imaging with compressed sensing—a deep learning approach”, *Light: Science & Applications*, vol. 8, no. 1, p. 26, 2019.
- [147] J. T. Smith, R. Yao, N. Sinsuebphon, *et al.*, “Fast fit-free analysis of fluorescence lifetime imaging via deep learning”, *Proceedings of the National Academy of Sciences*, vol. 116, no. 48, pp. 24 019–24 030, 2019.
- [148] S. C. Warren, A. Margineanu, D. Alibhai, *et al.*, “Rapid global fitting of large fluorescence lifetime imaging microscopy datasets”, *PLoS One*, vol. 8, no. 8, e70687, 2013.
- [149] A. J. Bowman, B. B. Klopfer, T. Juffmann, and M. A. Kasevich, “Electro-optic imaging enables efficient wide-field fluorescence lifetime microscopy”, *Nature communications*, vol. 10, no. 1, p. 4561, 2019.
- [150] M. Eibl, S. Karpf, D. Weng, *et al.*, “Single pulse two photon fluorescence lifetime imaging (sp-flim) with mhz pixel rate”, *Biomedical optics express*, vol. 8, no. 7, pp. 3132–3142, 2017.
- [151] A. Tsikouras, R. Berman, D. W. Andrews, and Q. Fang, “High-speed multifocal array scanning using refractive window tilting”, *Biomedical optics express*, vol. 6, no. 10, pp. 3737–3747, 2015.
- [152] N. Krstajić, S. Poland, J. Levitt, *et al.*, “0.5 billion events per second time correlated single photon counting using CMOS SPAD arrays”, *Optics letters*, vol. 40, no. 18, pp. 4305–4308, 2015.
- [153] K. J. Martin, E. J. McGhee, J. P. Schwarz, *et al.*, “Accepting from the best donor; analysis of long-lifetime donor fluorescent protein pairings to optimise dynamic FLIM-based FRET experiments”, *Plos one*, vol. 13, no. 1, e0183585, 2018.
- [154] N. C. Shaner, G. G. Lambert, A. Chamma, *et al.*, “A bright monomeric green fluorescent protein derived from branchiostoma lanceolatum”, *Nature methods*, vol. 10, no. 5, pp. 407–409, 2013.
- [155] S. Burri, H. Homulle, C. Bruschini, and E. Charbon, “LinoSPAD: a time-resolved 256x1 CMOS SPAD line sensor system featuring 64 FPGA-based TDC channels running at up to 8.5 giga-events per second”, in *Optical Sensing and Detection IV*, SPIE, vol. 9899, 2016, pp. 57–66.
- [156] C. Bruschini, S. Burri, E. Bernasconi, *et al.*, “LinoSPAD2: A 512x1 linear SPAD camera with system-level 135-ps SPTR and a reconfigurable computational engine for time-resolved single-photon imaging”, in *Quantum Sensing and Nano Electronics and Photonics XIX*, SPIE, vol. 12430, 2023, pp. 126–135.

BIBLIOGRAPHY

- [157] F. Madonini and F. Villa, “Single photon avalanche diode arrays for time-resolved raman spectroscopy”, *Sensors*, vol. 21, no. 13, p. 4287, 2021.
- [158] C. Bruschini, H. Homulle, and E. Charbon, “Ten years of biophotonics single-photon SPAD imager applications: retrospective and outlook”, in *Multiphoton Microscopy in the Biomedical Sciences XVII*, SPIE, vol. 10069, 2017, pp. 213–233.
- [159] C. Niclass, M. Sergio, and E. Charbon, “A single photon avalanche diode array fabricated in 0.35- μm CMOS and based on an event-driven readout for TCSPC experiments”, in *Advanced Photon Counting Techniques*, SPIE, vol. 6372, 2006, pp. 212–223.
- [160] K. A. Christensen and M. D. Morris, “Hyperspectral raman microscopic imaging using powell lens line illumination”, *Applied spectroscopy*, vol. 52, no. 9, pp. 1145–1147, 1998.
- [161] H. Qu, Z. Ling, X. Qi, Y. Xin, C. Liu, and H. Cao, “A remote raman system and its applications for planetary material studies”, *Sensors*, vol. 21, no. 21, p. 6973, 2021.
- [162] D. Faccio and A. Velten, “A trillion frames per second: the techniques and applications of light-in-flight photography”, *Reports on Progress in Physics*, vol. 81, no. 10, p. 105 901, 2018.
- [163] N. Abramson, “Light-in-flight recording by holography”, *Optics letters*, vol. 3, no. 4, pp. 121–123, 1978.
- [164] N. Abramson, “Light-in-flight recording: high-speed holographic motion pictures of ultrafast phenomena”, *Applied optics*, vol. 22, no. 2, pp. 215–232, 1983.
- [165] N. H. Abramson and K. G. Spears, “Single pulse light-in-flight recording by holography”, *Applied optics*, vol. 28, no. 10, pp. 1834–1841, 1989.
- [166] A. Velten, E. Lawson, A. Bardagjy, M. Bawendi, and R. Raskar, “Slow art with a trillion frames per second camera”, in *ACM SIGGRAPH 2011 Talks*, 2011, pp. 1–1.
- [167] A. Velten, D. Wu, A. Jarabo, *et al.*, “Femto-photography: capturing and visualizing the propagation of light”, *ACM Transactions on Graphics (ToG)*, vol. 32, no. 4, pp. 1–8, 2013.
- [168] G. Gariepy, N. Krstajić, R. Henderson, *et al.*, “Single-photon sensitive light-in-flight imaging”, *Nature communications*, vol. 6, no. 1, p. 6021, 2015.
- [169] M. Laurenzis, J. Klein, E. Bacher, and N. Metzger, “Multiple-return single-photon counting of light in flight and sensing of non-line-of-sight objects at shortwave infrared wavelengths”, *Optics letters*, vol. 40, no. 20, pp. 4815–4818, 2015.
- [170] R. Warburton, C. Aniculaesei, M. Clerici, *et al.*, “Observation of laser pulse propagation in optical fibers with a SPAD camera”, *Scientific reports*, vol. 7, no. 1, p. 43 302, 2017.
- [171] M. O’Toole, F. Heide, D. B. Lindell, K. Zang, S. Diamond, and G. Wetzstein, “Reconstructing transient images from single-photon sensors”, in *Proceedings of the IEEE conference on computer vision and pattern recognition*, 2017, pp. 1539–1547.
- [172] K. Wilson, B. Little, G. Gariepy, R. Henderson, J. Howell, and D. Faccio, “Slow light in flight imaging”, *Physical Review A*, vol. 95, no. 2, p. 023 830, 2017.

- [173] Q. Sun, X. Dun, Y. Peng, and W. Heidrich, “Depth and transient imaging with compressive spad array cameras”, in *Proceedings of the IEEE Conference on Computer Vision and Pattern Recognition*, 2018, pp. 273–282.
- [174] M. Laurenzis, J. Klein, and E. Bacher, “Relativistic effects in imaging of light in flight with arbitrary paths”, *Optics letters*, vol. 41, no. 9, pp. 2001–2004, 2016.
- [175] Y. Zheng, M.-J. Sun, Z.-G. Wang, and D. Faccio, “Computational 4D imaging of light-in-flight with relativistic effects”, *Photonics Research*, vol. 8, no. 7, pp. 1072–1078, 2020.
- [176] T. G. Etoh, T. Okinaka, Y. Takano, *et al.*, “Light-in-flight imaging by a silicon image sensor: Toward the theoretical highest frame rate”, *Sensors*, vol. 19, no. 10, p. 2247, 2019.
- [177] D. Turecek, L. Pinsky, J. Jakubek, Z. Vykydal, N. Stoffle, and S. Pospisil, “Small dosimeter based on Timepix device for International Space Station”, *Journal of Instrumentation*, vol. 6, no. 12, p. C12037, 2011.
- [178] L. Paolozzi, M. Munker, R. Cardella, *et al.*, “Picosecond avalanche detector—working principle and gain measurement with a proof-of-concept prototype”, *Journal of Instrumentation*, vol. 17, no. 10, P10032, 2022.
- [179] M. M. Vignetti *et al.*, “3D Silicon Coincidence Avalanche Detector (3D-SiCAD) for charged particle detection”, *Nucl. Instrum. Meth. A*, vol. 881, pp. 53–59, 2018. DOI: 10.1016/j.nima.2017.10.089.
- [180] M. Benoit, J. B. De Mendizabal, F. Di Bello, *et al.*, “The FE-I4 telescope for particle tracking in testbeam experiments”, *Journal of Instrumentation*, vol. 11, no. 07, P07003, 2016.
- [181] G. Iacobucci, S. Zambito, M. Milanese, *et al.*, “Testbeam results of the picosecond avalanche detector proof-of-concept prototype”, *Journal of Instrumentation*, vol. 17, no. 10, P10040, 2022.
- [182] A. Lacaita, S. Cova, M. Ghioni, and F. Zappa, “Single-photon avalanche diode with ultrafast pulse response free from slow tails”, *IEEE electron device letters*, vol. 14, no. 7, pp. 360–362, 1993.
- [183] A. Gulinatti, I. Rech, M. Assanelli, M. Ghioni, and S. Cova, “A physically based model for evaluating the photon detection efficiency and the temporal response of SPAD detectors”, *Journal of Modern Optics*, vol. 58, no. 3-4, pp. 210–224, 2011.
- [184] G. Ripamonti and S. Cova, “Carrier diffusion effects in the time-response of a fast photodiode”, *Solid-state electronics*, vol. 28, no. 9, pp. 925–931, 1985.
- [185] W. Becker, F. Gramuglia, M.-L. Wu, E. Charbon, and C. Bruschini, *8.7 ps FWHM IRF width from ultrafast SPAD*, 2023. [Online]. Available: <https://www.becker-hickl.com/literature/application-notes/8-7-ps-fwhm-irf-width-from-ultrafast-spad/>.

BIBLIOGRAPHY

- [186] N. Cartiglia, A. Staiano, V. Sola, *et al.*, “Beam test results of a 16 ps timing system based on ultra-fast silicon detectors”, *Nuclear Instruments and Methods in Physics Research Section A: Accelerators, Spectrometers, Detectors and Associated Equipment*, vol. 850, pp. 83–88, 2017.
- [187] A. Lampis, F. Borgato, D. Brundu, *et al.*, “10 ps timing with highly irradiated 3D trench silicon pixel sensors”, *Journal of Instrumentation*, vol. 18, no. 01, p. C01051, 2023.
- [188] W. Riegler and P. Windischhofer, “Time resolution and efficiency of SPADs and SiPMs for photons and charged particles”, *Nuclear Instruments and Methods in Physics Research Section A: Accelerators, Spectrometers, Detectors and Associated Equipment*, vol. 1003, p. 165 265, 2021.
- [189] A. Kirmani, T. Hutchison, J. Davis, and R. Raskar, “Looking around the corner using ultrafast transient imaging”, *International journal of computer vision*, vol. 95, pp. 13–28, 2011.
- [190] A. Velten, T. Willwacher, O. Gupta, A. Veeraraghavan, M. G. Bawendi, and R. Raskar, “Recovering three-dimensional shape around a corner using ultrafast time-of-flight imaging”, *Nature communications*, vol. 3, no. 1, p. 745, 2012.
- [191] O. Katz, E. Small, and Y. Silberberg, “Looking around corners and through thin turbid layers in real time with scattered incoherent light”, *Nature photonics*, vol. 6, no. 8, pp. 549–553, 2012.
- [192] M. O’Toole, D. B. Lindell, and G. Wetzstein, “Confocal non-line-of-sight imaging based on the light-cone transform”, *Nature*, vol. 555, no. 7696, pp. 338–341, 2018.
- [193] X. Liu, I. Guillén, M. La Manna, *et al.*, “Non-line-of-sight imaging using phasor-field virtual wave optics”, *Nature*, vol. 572, no. 7771, pp. 620–623, 2019.
- [194] J. Zhao, F. Gramuglia, P. Keshavarzian, *et al.*, “A Gradient-Gated SPAD Array for Non-Line-of-Sight Imaging”, *IEEE Journal of Selected Topics in Quantum Electronics*, 2023.
- [195] D. Faccio, A. Velten, and G. Wetzstein, “Non-line-of-sight imaging”, *Nature Reviews Physics*, vol. 2, no. 6, pp. 318–327, 2020.
- [196] P. Coates, “The origins of afterpulses in photomultipliers”, *Journal of Physics D: Applied Physics*, vol. 6, no. 10, p. 1159, 1973.
- [197] G. Morton, H. Smith, and R. Wasserman, “Afterpulses in photomultipliers”, *IEEE Transactions on Nuclear Science*, vol. 14, no. 1, pp. 443–448, 1967.
- [198] I. Cusini, D. Berretta, E. Conca, *et al.*, “Historical Perspectives, State of art and Research Trends of Single Photon Avalanche Diodes and Their Applications (Part I: Single Pixels)”, *Frontiers in Physics*, p. 607, 2022.
- [199] I. Cusini, D. Berretta, E. Conca, *et al.*, “Historical Perspectives, State of Art and Research Trends of SPAD Arrays and Their Applications (Part II: SPAD Arrays)”, *Frontiers in Physics*, vol. 10, p. 906 671, 2022.

- [200] A. E. Lita, D. V. Reddy, V. B. Verma, R. P. Mirin, and S. W. Nam, “Development of superconducting single-photon and photon-number resolving detectors for quantum applications”, *Journal of Lightwave Technology*, vol. 40, no. 23, pp. 7578–7597, 2022.
- [201] C. Durnez, C. Virmontois, P. Panuel, *et al.*, “Evaluation of Microlenses, Color Filters, and Polarizing Filters in CIS for Space Applications”, *Sensors*, vol. 23, no. 13, p. 5884, 2023.
- [202] M. Adhikari, R. Houhou, J. Hniopek, and T. Bocklitz, “Review of Fluorescence Lifetime Imaging Microscopy (FLIM) Data Analysis Using Machine Learning”, *Journal of Experimental and Theoretical Analyses*, vol. 1, no. 1, pp. 44–63, 2023.
- [203] Y. Lin, P. Mos, A. Ardelean, C. Bruschini, and E. Charbon, “Coupling a Recurrent Neural Network to SPAD TCSPC Systems for Real-time Fluorescence Lifetime Imaging”, *arXiv preprint arXiv:2306.15599*, 2023.
- [204] Y. Lin and E. Charbon, “Spiking Neural Networks for Active Time-Resolved SPAD Imaging”, in *WACV*, 2024.
- [205] S. Cova, M. Ghioni, A. Lacaita, C. Samori, and F. Zappa, “Avalanche photodiodes and quenching circuits for single-photon detection”, *Applied optics*, vol. 35, no. 12, pp. 1956–1976, 1996.
- [206] G. Zappalà, F. Acerbi, A. Ferri, *et al.*, “Set-up and methods for SiPM Photo-Detection Efficiency measurements”, *Journal of Instrumentation*, vol. 11, no. 08, P08014, 2016.

List of Publications

Journal articles

K. Morimoto, A. Ardelean, M.-L. Wu, A. C. Ulku, I. M. Antolovic, C. Bruschini, and E. Charbon, "**Megapixel time-gated SPAD image sensor for 2D and 3D imaging applications**", *Optica*, 7(4), 346-354. (2020)

V. Zickus*, M.-L. Wu*, K. Morimoto, V. Kapitany, A. Fatima, A. Turpin, R. Insall, J. Whitelaw, L. Machesky, C. Bruschini, D. Faccio, and E. Charbon, "**Fluorescence lifetime imaging with a megapixel SPAD camera and neural network lifetime estimation**", *Scientific Reports*, 10(1), 1-10. (2020)

F. Gramuglia, M.-L. Wu, C. Bruschini, M.-J. Lee, and E. Charbon, "**A Low-noise CMOS SPAD Pixel with 12.1 ps SPTR and 3 ns Dead Time**", *IEEE Journal of Selected Topics in Quantum Electronics*, 28(2), 1-9. (2021)

K. Morimoto*, M.-L. Wu*, A. Ardelean*, and E. Charbon, "**Superluminal motion-assisted four-dimensional light-in-flight imaging**", *Physical Review X*, 11(1), 011005. (2021)

F. Gramuglia, E. Ripiccini, C. A. Fenoglio, M.-L. Wu, L. Paolozzi, C. Bruschini, and E. Charbon, "**Sub-10 ps Minimum Ionizing Particle Detection With Geiger-Mode APDs**", *Frontiers in Physics*, 370. (2022)

M.-L. Wu, E. Ripiccini, E. Kizilkan, F. Gramuglia, P. Keshavarzian, C. A. Fenoglio, K. Morimoto, and E. Charbon, "**Radiation Hardness Study of Single-Photon Avalanche Diode for Space and High Energy Physics Applications**", *Sensors*, 22(8), 2919. (2022)

Conference and workshop presentations

K. Morimoto, A. Ardelean, M.-L. Wu, A. C. Ulku, I. M. Antolovic, V. Zickus, V. Kapitany, A. Fatima, A. Turpin, R. Insall, J. Whitelaw, L. Machesky, C. Bruschini, D. Faccio, and E. Charbon, "**Megapixel time-gated SPAD image sensor for scientific imaging applications**", *In SPIE High-Speed Biomedical Imaging and Spectroscopy VI*. (2021)

*Shared first authorship

F. Gramuglia, M.-L. Wu, M.-J. Lee, C. Bruschini, and E. Charbon, "**SPAD Microcells with 12.1 ps SPTR for SiPMs in TOF-PET Applications**", In *IEEE Nuclear Science Symposium and Medical Imaging Conference (NSS/MIC)* (2021)

M.-L. Wu, E. Ripiccini, E. Kizilkan, F. Gramuglia, P. Keshavarzian, C. A. Fenoglio, K. Morimoto, C. Bruschini, and E. Charbon, "**Radiation Hardness Study of SPAD for Space and High Energy Physics Applications**", In *International SPAD Sensor Workshop (ISSW)* (2022)

M.-L. Wu, E. Ripiccini, C. A. Fenoglio, F. Gramuglia, P. Keshavarzian, E. Kizilkan, and E. Charbon, "**Characterization of Single-Photon Avalanche Diodes Under High Proton Radiation**", In *IEEE Nuclear and Space Radiation Effects Conference (NSREC)* (2022)

M.-L. Wu, E. Ripiccini, E. Kizilkan, F. Gramuglia, P. Keshavarzian, C. A. Fenoglio, K. Morimoto, C. Bruschini and E. Charbon, "**CMOS SPADs for High Radiation Environments**", In *IEEE Nuclear Science Symposium and Medical Imaging and Room Temperature Semiconductor Detector Conference (NSS/MIC/RTSD)* (2022)

E. Ripiccini*, M.-L. Wu*, F. Gramuglia, E. Kizilkan, J. Benserhir, C. Bruschini, and E. Charbon, "**Photon and minimum ionizing particle detection with ultra fast Geiger mode APDs**", In *Ultrafast Imaging and Tracking Instrumentation, Methods and Applications Conference (ULITIMA)* (2023)

M.-L. Wu, E. Ripiccini, J. Benserhir, F. Gramuglia, E. Kizilkan, C. Bruschini, and E. Charbon, "**Single-Photon Avalanche Diode for Scalable Particle Detection**", In *IEEE International conference on smart technologies (EUROCON)* (2023)

R. Dolenc*, M.-L. Wu*, C. Bruschini*, E. Charbon, D. Consuegra Rodríguez, F. Gramuglia, P. Križan, S. Korpar, R. Pestotnik, and A. Seljak, "**Neutron radiation hardness of single-photon avalanche diodes for future RICH detectors**", In *IEEE Nuclear Science Symposium and Medical Imaging and Room Temperature Semiconductor Detector Conference (NSS/MIC/RTSD)* (2023)

M.-L. Wu and E. Charbon, "**SPADs for space**", In *Photonics 4 Space by Swissphotonics* (2023)

Preprints

K. Morimoto, A. Ardelean, M.-L. Wu, A. C. Ulku, I. M. Antolovic, C. Bruschini, and E. Charbon, "**A megapixel time-gated SPAD image sensor for 2D and 3D imaging applications**", *arXiv:1912.12910* (2019)

V. Zickus*, M.-L. Wu*, K. Morimoto, V. Kapitany, A. Fatima, A. Turpin, R. Insall, J. Whitelaw, L. Machesky, C. Bruschini, D. Faccio, and E. Charbon, "**Wide-field Fluorescence Lifetime Imaging Microscopy with a High-Speed Mega-pixel SPAD Camera**", *bioRxiv: 2020.06.07.138685* (2020)

Curriculum Vitae

Ming-Lo Wu

Nationality: Taiwan, R.O.C.

Education

École polytechnique fédérale de Lausanne (EPFL), Switzerland

Advanced Quantum Architecture Laboratory (AQUA)

Doctoral Program in Microsystems and Microelectronics

September 2019 – Present

Katholieke Universiteit Leuven (KUL), Belgium

Master of Nanoscience, Nanotechnology and Nanoengineering

September 2016 – June 2018

National Chiao Tung University (NCTU), Taiwan (now NYCU)

Undergraduate Honors Program of Nano Science and Engineering

September 2013 – June 2016

Experience

TSMC

R&D intern: High Voltage Electrostatic Discharge (ESD) Protection Engineer

2017

IMEC

Master thesis: Design, fabrication and characterization of magnetic domain wall injector

June 2017 – July 2018